Electron Microscopy-based Study of Nanostructured ZnO:Morphological, Structural and Electrical Characterization

POLITECNICO DI TORINO

DOCTORAL SCHOOL

PhD Thesis in Physics

Electron Microscopy-Based Study of Nanostructured ZnO:

Morphological, Structural and Electrical Characterization

Author:
Marco Fontana

Supervisor:
Prof. C.F.Pirri
Co-supervisor:
Dr. A.Chiodoni

Contents

Introduction

Zinc oxide is considered a very interesting and promising material due to its functional properties: it is a piezoelectric wide band gap semiconductor which can be synthesized in a wide variety of nanostructures, such as nanowires, nanobelts, nanopods, nanoparticles, nanostructured thin films. It is therefore an ideal candidate for the development of innovative miniaturized devices ranging over the field of nanotechnology. The simultaneous presence of semiconducting behavior, piezoelectricity and surface effects dictated by the nanostructuration could be exploited for sensing applications, such as pressure sensors embedded in artificial skin, gas sensors, biosensors. Furthermore, ZnO nanostructures have attracted great interest in view of energy harvesting applications: nanostructured ZnO is currently employed as a photoanode material in dye-sensitized solar cells (DSSC) and examples of nanogenerators based on ZnO nanowire arrays are already present in the literature. However, in order to reach a better understanding of physical properties at the nanoscale and for the performance optimization of devices, a lot of work still needs to be done. It is important to establish relationships between morphological, structural and electrical properties, in order to assess which structure gives the best performance for a particular application. In the framework of the scientific plan $2009-2013$, ZnO nanostructures have been studied at Center for Space Human Robotics (CSHR) Istituto Italiano di Tecnologia as candidates for tactile sensors and energy harvesting applications, such as dye-sensitized solar cells and mechanical harvesting. Part of my thesis work has been devoted to the morphological and structural characterization of all the ZnO nanostructures that have been synthesized at the CSHR. This activity required the use of electron microscopy; in particular, for the research activity reported in this thesis a dual-beam FIB-SEM workstation has been used for the morphological characterization of the samples and preparation of TEM samples, while TEM has been used for the morphological and structural analysis. Among the different ZnO nanostructures, ZnO nanowires are of particular interest for applications, since they have well-defined geometry at the nanoscale and they have controllable crystalline orientation. Part of my research activity has been devoted to the development of procedures for the in-situ electrical characterization of single ZnO nanowires, based on the electron beam and ion-beam induced deposition of contacts and subsequent two-probe electrical characterization performed in the dual-beam FIB-FESEM chamber by micromanipulators.

The thesis is organized as follows:

- **Chapter 1**: this chapter is a brief introduction to ZnO and its interesting properties. Bulk properties, deposition techniques of thin films, synthesis of nanostructures and their applications are introduced in this chapter
- **Chapter 2**: in this chapter the characterization techniques adopted in this thesis work are described. Particular attention is devoted to electron microscopy
- **Chapter 3**: here all the ZnO thin films and nanostructures synthesized at the CSHR are presented, alongside analysis of their structure and morphology. The first part of the chapter is dedicated to thin films with different morphologies, while the second part is devoted to micro and nanowires
- **Chapter 4**: this chapter is focused on the electrical characterization of single ZnO microwires and nanowires. Both the deposition of the contacts and the actual electrical characterization are performed in the FIB-SEM chamber. The chapter starts with some preliminary studies and proceeds with the presentation of the experimental results.
- **Chapter 5**: this chapter reports on the possibility of performing impedance spectroscopy on a single microwire
- **Chapter 6**: a brief summary and a critical review of the experimental results achieved in this thesis are given, followed by possible future works primarily based on impedance spectroscopy

Chapter 1

ZnO nanostructures: synthesis and applications

In recent years, ZnO has been the subject of an intense and widespread research activity due to a variety of interesting properties which make it a promising material for a multitude of applications. It is a wide bandgap piezoelectric semiconductor with a large exciton binding energy; moreover, ZnO can be synthesized in a wide variety of nanostructures, such as nanostructured thin films, nanorods, nanowires, nanobelts [1]. The simultaneous presence of semiconducting behavior, piezoelectricity and surface effects dictated by the nanostructuration could be exploited for many different applications: from sensing (pressure sensors, gas sensors, biosensors) to energy harcesting devices (Dye-Sensitized-Solar-Cells, piezoelectric generators). In this chapter we will introduce bulk ZnO and its important physical properties; we will then introduce thin films deposition techniques and we will conclude the chapter presenting synthesis approaches for the production of ZnO nanostructures and their potential applications in nanotechnology.

1.1 Properties of bulk ZnO

In the first half of the 20^{th} century, ZnO was employed in different applications, such as paints, adhesives, medical and pharmaceutical technology [2]. It was not until the 1950s that ZnO started attracting interest as compound semiconductor and many of its interesting properties were discovered and further investigated in the 1950s and 1960s [3]. In the 1970s, it was found that as-grown ZnO shows unintentional n-type conductivity and studies on doping and implantation of impurities were carried out. Research on ZnO has had a fluctuating evolution over decades since the 1970s, reaching its peak in recent years due to the growing interest in wide bandgap semiconductors and nanostructured materials. Detailed description of bulk ZnO properties will be presented in the following subsections.

1.1.1 Crystalline structure

ZnO crystallizes in three different structures:

- *wurtzite*: stable phase at ambient pressure and temperature
- *zincblende*: it is stable only by growth on cubic structures
- *rocksalt*: high pressure metastable phase forming at $P \sim 10\ GPa$

The wurtzite phase is therefore the most common under conventional conditions. It has hexagonal unit cell with space group $P6_3mc$ (Hermann-Mauguin notation); it is characterized by two inter-connecting sublattices of Zn^{2+} and O^{2-}, such that each Zn ion is surrounded by a tetrahedron of O ions and vice-versa, as shown in figure (1.1). The crystal structure can in fact be obtained by

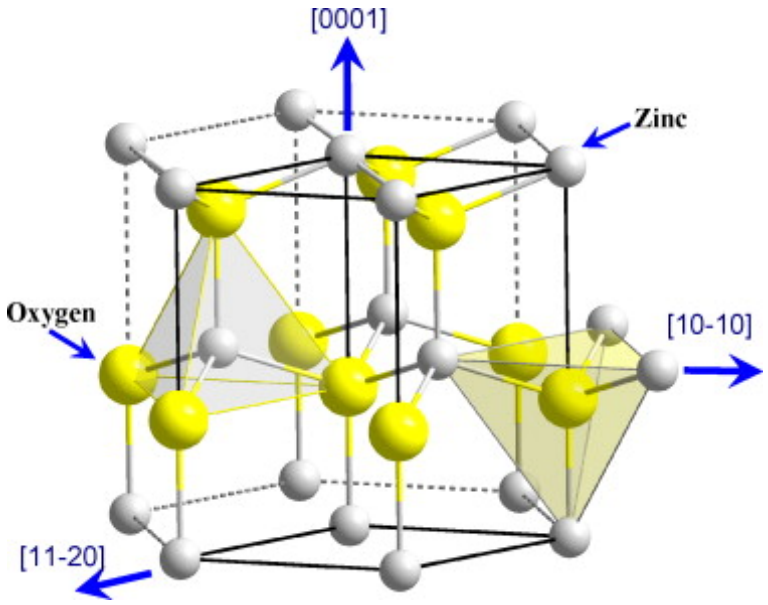

Figure 1.1: wurtzite crystalline structure of ZnO

stacking planes composed by either Zn^{2+} or O^{2-} ions. The charged ions produce polar surfaces, such as the positively-charged Zn-terminated (0001) and the negatively-charged O-terminated $(000\bar{1})$ surfaces which give rise to spontaneous polarization along the c-axis. These surfaces are atomically flat and do not experience surface reconstruction [4], despite having non-zero dipole moment perpendicular to the surface. The crystallographic vectors of the wurtzite structure are

$$\vec{a} = a(1/2, \sqrt{3}/2, 0)$$
$$\vec{b} = a(1/2, -\sqrt{3}/2, 0)$$
$$\vec{c} = (0, 0, c)$$

The lattice parameters of the hexagonal unit cell are $a = 3.25\mathring{A}$ and $c = 5.21\mathring{A}$ [5] (we have neglected digits affected by fluctuations of results between different research groups).

1.1.2 Piezoelectricity and Mechanical properties

The lack of a centre of symmetry in the wurtzite crystalline structure leads to piezoelectricity in ZnO. Piezoelectricity can be described as a linear coupling between the electrical and the mechanical behaviour of a solid system. The mechanical response of a solid under deformation is encoded in the Hooke's law, which linearly relates the stress tensor components and the strain tensor components:

$$\sigma_{ij} = C_{ijkl}\epsilon_{kl} \tag{1.1}$$

with C_{ijkl} the elastic stiffness tensor. This relationship is invertible and the strain can be expressed as a linear function of the stress through the elastic compliance tensor

$$\epsilon_{ij} = S_{ijkl}\sigma_{kl} \tag{1.2}$$

Both the strain and the stress tensors are symmetric; this symmetry implies conditions on the compliance and stiffness tensors which reduce their independent components. A more compact notation (the *Voigt notation*) which expresses (n)-order symmetric tensors as $(n-1)$-order tensors is therefore introduced:

$$\epsilon_{ij} \rightarrow \epsilon_k$$

$$\sigma_{ij} \rightarrow \sigma_k$$

$$C_{ijmn} \rightarrow C_{kl}$$

$$S_{ijmn} \rightarrow S_{kl}$$

ij	11	22	33	23	13	12
k	1	2	3	4	5	6

As previously mentioned, piezoelectricity is a linear coupling between mechanical and electrical properties; more precisely:

- *direct piezoelectric effect*: electric charge is generated at the surface of the solid as a result of mechanical strain

  $$P_i = e_{ijk}\epsilon_{jk} \rightarrow P_i = e_{im}\epsilon_m \tag{1.3}$$

  where P_i is the polarization vector

- *converse piezoelectric effect*: mechanical deformation arises due to applied electric field

  $$\epsilon_{ij} = d_{ijk}E_k \rightarrow \epsilon_m = d_{mk}E_k \tag{1.4}$$

  where E_k is the applied electric field

By thermodynamic approach, the equivalence of the direct and converse piezoelectric effect can be proved [6]. Using the properties of the strain tensor and symmetry arguments, it can be shown that for the hexagonal wurtzite phase there are only three independent components of the piezoelectric tensors, as it is shown in the Voigt notation expressions for the piezoelectric tensors:

$$e_{kl} = \begin{pmatrix} 0 & 0 & 0 & 0 & e_{15} & 0 \\ 0 & 0 & 0 & e_{15} & 0 & 0 \\ e_{31} & e_{31} & e_{33} & 0 & 0 & 0 \end{pmatrix} \tag{1.5}$$

$$d_{kl} = \begin{pmatrix} 0 & 0 & 0 & 0 & d_{15} & 0 \\ 0 & 0 & 0 & d_{15} & 0 & 0 \\ d_{31} & d_{31} & d_{33} & 0 & 0 & 0 \end{pmatrix} \tag{1.6}$$

As a final remark we stress that the two piezoelectric tensors can be related through:

$$e_{ij} = d_{ik} C_{kj} \tag{1.7}$$

with C_{kj} the elastic stiffness tensor in the Voigt notation. A work by Kobiakov [7] published in 1980 presents measurements of all tensor components of the elastic compliance, stiffness and the piezoelectric tensors of a set of ZnO single crystals; particularly, the highest piezoelectric coefficient (e_{33}) was evaluated as $e_{33} = 0.96\ C/m^2 \pm 2.1\%$ (or alternatively $d_{33} = 12.3 \cdot 10^{-12}\ C/N$), which is in good agreement with theoretical studies such as the one proposed by Dal Corso et al. [8] published in 1994, which yields a $e_{33} = 0.92$ theretical value from *ab initio* calculations. By comparing ZnO with other piezoelectric materials, taking d_{33} into account as a measure of the strength of the piezoelectric response, we can say that ZnO has a rather strong piezoelectric response. Although inferior by at least one order of magnitude to ferroelectric ceramics such as $BaTiO_3$ and lead zirconate titanate (PZT) [9], ZnO has the highest electromechanical coupling among tetrahedrally bonded semiconductors such as GaN and AlN [5]. Concerning mechanical properties, Kucheyev et al. [10] have investigated the deformation behaviour of c-axis oriented single crystal ZnO by nanoindentation with a diamond spherical tip; they have evaluated $H = 5.0 \pm 0.1\ GPa$ and $E = 111.2 \pm 4.7\ GPa$ as hardness value and Young's modulus, respectively. For comparison, ZnO is significantly softer than GaN, whose single crystal mechanical properties have been evaluated by the same group with the same instrumentation [11], yielding $15.5 \pm 0.9\ GPa$ as hardness and $210 \pm 23\ GPa$ as Young's modulus.

1.1.3 Pyroelectricity and Thermal properties

As was previously stated, the presence of alternating polar planes along the c-axis leads to spontaneous polarization in ZnO. This spontaneous polarization is temperature-dependent, meaning that changes in temperature give rise to voltage across the crystal: the coupling between the thermal and the electrical

behavior of a crystal is called pyroelectricity. The pyroelectric response of a material can be expressed through the pyroelectric coefficient

$$p_i = \frac{\partial P_i}{\partial T} \tag{1.8}$$

where P_i is the polarization and T the temperature. The experimental value for ZnO pyroelectric coefficient is $-9.4 \cdot 10^{-6}\ Cm^{-2}K^{-1}$ [12], which is 2 order of magnitudes lower than common poled ferroelectric ceramics such as $BaTiO_3$ and PZT. It is well-known that solids tend to change their volume as a response to changes in temperature, while keeping their shape unaltered; the relationship between changes in size and changes in temperature is expressed by the thermal expansion coefficients. In the case of crystalline materials, one can define the thermal expansion coefficients as the fractional change in the magnitude of the lattice parameters per degree change in temperature; for a given lattice parameter a the related thermal expansion coefficient α_a at a temperature T_0 is

$$\alpha_a = \frac{1}{a} \cdot \left(\frac{da}{dT} \right) |_{T=T_0}$$

Iwanaga et al. [13] measured the temperature dependence of the ZnO lattice parameters a and c, obtaining second-order polynomial dependence as shown in the following relations:

$$a(T) = 3.2468 + 0.623 \cdot 10^{-5} T + 12.94 \cdot 10^{-9} T^2 \tag{1.9}$$

$$c(T) = 5.2042 + 0.522 \cdot 10^{-5} T + 12.13 \cdot 10^{-9} T^2 \tag{1.10}$$

with room temperature expansion coefficients $\alpha_a = 4.31 \cdot 10^{-6} K^{-1}$ and $\alpha_c = 2.49 \cdot 10^{-6} K^{-1}$.

1.1.4 Band structure and Electrical properties

ZnO is a direct band-gap semiconductor: the valence band maximum and the conduction band minimum are characterized by the same crystal momentum ($\vec{k} = \vec{0}$).The experimental value for the bandgap at room temperature is $E_g = 3.37eV$ [14] with temperature dependence up to $300K$ given by the empirical relationship [15]

$$E_g(T) = E_{g,T=0} + \frac{5.05 \cdot 10^{-4} T^2}{T - 900} \tag{1.11}$$

Being a wide-band gap semiconductor, ZnO is therefore in principle a good candidate for optoelectronics applications in the blue-UV regions of the electromagnetic spectrum. The free-exciton binding energy is $60meV$, which is much higher than the thermal energy at room temperature ($k_b T \cong 25meV$); efficient excitonic emission can therefore persist at room temperature or even higher. Concerning the low-electric field transport properties, Hall mobility and carrier concentration measurements at different temperatures on nominally undoped ZnO bulk samples have been reported in the literature. In this regard,

we have to recall that wurtzite ZnO becomes naturally a n-type semiconductor due to the presence of unavoidable defects or impurities; up to now, the causes of the un-intentional n-type doping are still debated, although theoretical work suggests interstitial hydrogen could be responsible for the background n-type conductivity [16]. To the best of our knowledge, the highest measured room-temperature mobility of undoped bulk single crystal ZnO has been measured by Look and coworkers [17]: the reported value for the mobility is $\mu_H = 205$ $cm^2V^{-1}s^{-1}$ with a carrier concentration of $6.0 \cdot 10^{16}$ cm^{-3}.

1.2 Deposition of ZnO thin films

The production of thin films of ZnO dates back to the 1970s and research has been carried out until now in order to improve the deposition processes and the subsequent quality of the films mainly for piezoelectric application (especially Surface Acoustic Wave filters). In the present section we will present the main synthesis approaches commonly used to obtain ZnO thin films.

1.2.1 Deposition and growth

The most common techniques used for the deposition of ZnO films are:

- *Pulsed Laser Deposition*: The PLD technique consists of three different stages:

  1. the laser beam strikes a solid target and produces a plume of gas phase material
  2. interaction of the plume with the background ambient
  3. the ablated material condenses onto a suitable substrate where the thin film grows

  The experimental parameters which influence the outcome of the deposition (morphology, structure and chemical composition of the film) are: laser wavelength, target composition, background pressure (Ultra-High-Vacuum or oxygen as background gas for the oxidation of the films), the choice of substrate and its temperature. ZnO thin films have been obtained from a variety of target materials: ceramic discs prepared from pressed powders, single crystal ZnO, pure metallic Zn with oxygen as a reactive gas. Many different substrates have been used for the PLD of ZnO thin films, depending on the particular application of the samples: amorphous glass substrates [18], single crystal substrates (Si, GaAs) [19], sapphire (Al_2O_3) [20].

- *Chemical Vapor Deposition*: CVD is a a thin film growth process which involves the chemically-induced deposition of volatile precursors on a suitable substrate; typical CVD systems allow control on several parameters, such as total pressure, flux of carrier gases, substrate temperature. If

the gas precursors are organometallic, the process is called metalorganic chemical vapor deposition (MOCVD). ZnO growth by MOCVD has been reported in the literature: zinc acetylacetonate was used as organometallic precursor gas for the deposition on sapphire substrates [21].

- *Molecular Beam Epitaxy*: One of the main advantages of MBE with respect to the other deposition techniques is the fact that the crystalline structure of the surface of the thin film can be analysed in-situ by Reflection High-Energy Electron Diffraction (RHHED): the deposition process can therefore be monitored real-time. The MBE process takes place in UHV without the use of carrier gases: ideally only gases containing the constituent elements are present in the chamber. The constituent elements reach the heated substrate in the form of molecular or atomic beams, usually obtained by sublimation of one or more source materials. Typical growth rates are low ($1\mu ms^{-1}$) and extremely high-purity samples can be obtained. For ZnO thin film deposition, high-purity Zn metal is evaporated from an effusion cell, while reactive oxygen species obtained with a RF plasma source are directed to the substrate in order to obtain the oxidation of the metal. The most commonly employed substrate is sapphire [22], [23].

- *Sputter deposition*: Sputtering is a popular and relatively low-cost deposition technique by which it is possible to obtain large-size well-oriented and uniform thin films, with high deposition rates at relatively low temperatures. Sputtering is a process whereby atoms are ejected from a solid material (the target) as a consequence of the interaction with energetic particles (usually ions generated in a plasma). The ejected atoms can be deposited onto a substrate, forming thin films. Plasma is obtained by eletrical background of a gas phase; gas generation can be obtained by direct current (DC), low-frequency alternating current (AC) and radio-frequency (RF) sources, depending on the target material. ZnO films can be obtained by both DC and RF sources [24]. The choice for the sputter gas is usually Argon for deposition processes involving ZnO as target material, while a mixture of Ar and O_2 is used in the case of metallic Zn target material. Numerous materials are used as substrates, such as Si, sapphire, Au, glass, depending on the particular application of the thin films [25].

1.2.2 Applications

There are three main possible fields of application for ZnO thin films:

- piezoelectric devices
- optical applications
- dilute magnetic semiconductors

ZnO piezoelectric thin films are usually employed in Surface-Acoustic-Wave (SAW) devices as transducers: one interdigital transducer converts an electric signal into a mechanical wave while the receiving transducer converts the mechanical wave into an electric signal. Piezoelectric thin films can be deposited by MBE or MOCVD but they always exhibit unintentional n-type semiconducting behavior. This is a problem for piezoelectric applications because free carriers screen the piezoelectric potential. Sputtering is preferred as deposition technique of piezoelectric thin films because it allows easier compensation doping (with elements such as Li, Ni, Cu) and it has higher growing rates. ZnO is also considered a promising material for optical applications such as LED and possibly LD (laser diodes) in the near UV-region. This is due to the fact that ZnO has a wide band gap (3.37 eV at room temperature) and large exciton binding energy (60 meV). Therefore, room temperature radiative exciton recombination is allowed. However, one major obstacle which has to be overcome in order to obtain efficient light emitting devices is reliable p-type doping, which up to now is still an open issue. It is also believed that ZnO can be made ferromagnetic by the introduction of suitable transition metal ions, such as Mn and Cr. Semiconducting materials which exhibit ferromagnetic behavior are called Dilute Magnetic Semiconductor (DMS) and they are the essential building blocks for new-generation electronics exploiting spin-dependent transport phenomena.

1.3 ZnO Nanostructures

One major cause of the great appeal ZnO has had in the research community in the last few years is the fact that it can be synthesized in a variety of different nanostructures: nanobelts, nanowires, nanocages, nanocombs, nanosprings, nanorings, nanohelixdes ([1], [26], [27]). Nanostructured materials are interesting for both fundamental and applied research:

- they could be ideal experimental systems for the study of physical laws or phenomena which naturally emerge at the nanoscale, such as quantum confinement, ballistic transport, quantization of conductivity
- they could be used for the development of new-generation devices with an extremely wide field of application

Synthesis methods for the production of the most interesting ZnO nanostructures will be presented in the following subsections, as well as their possible future applications. Particular attention will be devoted to the ZnO NWs, which are among the most studied nanostructures alongside Carbon nanotubes [28] and Silicon nanowires [29].

1.3.1 Synthesis

A wide variety of nanostructures of ZnO can be obtained with different synthesis approaches; from the literature, this methods can basically be gathered in two

main groups: growth from gas phase or synthesis in solution. Growth from gas phases usually lead to higher crystalline quality and are in general carried out at higher temperatures; the most common growth methods are:

- vapor-transport method
- physical vapor deposition (PVD)
- CVD, MOCVD

Solution-based synthesis processes can be considered low-cost and are carried out at considerably lower temperatures; the most common synthesis approaches are:

- hydrothermal method
- electro-deposition
- template-assisted methods

In the following subsections, an overview of the different ZnO nanostructures will be presented alongside the different synthesis and growth methods which are reported in the literature.

Nanorods and Nanowires

By definition, nanowires are elongated nanoscale objects whose "'diameter"' lies in the range $(1-100)\ nm$, although the definition has been loosely used for wire-like objects with diameter up to hundreds of nm. Nanorods are basically wire-like nanoscale objects with lower aspect-ratio with respect to the wires: both their diameter and length are $< 100\ nm$. Nanowires and nanorods can be obtained from either gas-phase methods or solution-phase synthesis; a brief introduction to this methods will be presented in the following paragraphs.

In the vapor-transport method, or Vapor-Liquid-Solid method (VLS), a mixture of Zn vapor and O_2 gas is transported to the substrate, where ZnO is deposited. The process is usually carried out in Al_2O_3 horizontal furnace and Ar is employed as the carrier gas responsible for the vapor transport. There are 3 main choices as source material:

- ZnO powders, with melting point 1975 ℃
- ZnO:graphite mixture: mixture with graphite lowers significantly the decomposition temperature $(800-1100$ ℃)
- Zn metal: after evaporation of the source (Zn melting point is 420 ℃), Zn vapor is transported in the reaction region near the substrate, where it reacts with O_2 gas, in order to form ZnO

The vapor-transport method can be coupled with the action of a catalyst (usually Au), which enables more control over localization, density and aspect-ratio of the nanostructures, despite lowering the chemical purity. The catalyst can also be used as source of dopant: vapor-transport growth of n-type ZnO nanorods have been reported using In as catalyst [30].

One major advantage of wet chemical methods with respect to the VLS method is that, using ZnO seeds in the form of thin films or nanoparticles, ZnO nanowires can be grown on arbitrary substrates. The so-called seed layer is usually obtained by sputtering of a suitable source or by spin-coating suitable colloidal solutions. The most commonly used chemical agents for the synthesis of ZnO nanowires in aqueous solution are zinc nitrate $Zn(NO_3)_2$ and Hexamethylenetetramine HMT [31]. The precursor concentration determines the NWs density while temperature (usually kept under 100 ℃) and growth time influence the morphology of the NWs. Aligned nanowire arrays can be obtained on conductive substrates without the use of seed layers by the electrodeposition process. The electrodeposition process can also be coupled with the template-assisted approach in order to gain deeper control on the NW morphology; in the literature, the most widely used template is Anodic Aluminum Oxide (AAO) [32].

Nanobelts, Nanorings, Nanotubes

As the name suggests, nanobelts are nanostructures in the shape of belts: they have uniform width along their entire length , typically in the range $(50 - 300\ nm)$. The thickness of the belt is usually in the range $(10 - 30\ nm)$ and the cross-section is rectangular. Nanobelts can be prepared by a number of methods, including evaporation and condensation processes [33] and their growing crystalline direction can be controlled by doping with elements such as Li and Ni [1]. The two faces of the belts are in general polar surfaces; polar nanobelts tend to roll over in order to reduce the electrostatic energy. As a consequence, different structures can be obtained such as nanoring, nanohelixes and nanosprings, lead by the principle of minimization of the total energy. Other interesting ZnO nanostrucutres are nanotubes: they are basically hollow nanowires with diameter up to hundreds of nanometers. Succesful synthesis and growth of ZnO nanotubes have been reported in the literature with a variety of different approaches, such as MOCVD [34], hydrothermal method [35] and chemical etching of electrochemically deposited nanorods [36].

1.3.2 Applications

ZnO nanostructures are interesting because they merge the numerous properties of bulk ZnO with effects dictated by nanostructuration, paving the way for:

- possible integration in microdevices due to their small size
- exploitation of surface effects caused by the increased surface-to-volume ratio with respect to the bulk

- emergence of quantum behaviour

Microdevices based on ZnO nanostructures have already been demonstrated. Field-Effect-Transistors based on ZnO nanowires [37] and nanobelts [38] have been reported in the literature, showing that ZnO nanostructures can in fact be considered as possible building blocks for electronic applications. However, a lot of technological research still needs to be done in order to produce reliable Ohmic and Schottky contacts to ZnO nanostructures. Concerning the exploitation of piezoelectricity, examples of nanogenerators based on a single ZnO nanowire are already present in the literature [39]. This devices convert mechanical stimulation into an electric potential difference, while at the same time being miniaturized and possibly integrated in Micro-Electro-Mechanical systems. Since in nanostructures the surface-to-volume ratio is extremely high, most of nanostructured ZnO applications are based on surface-mediated interaction with the surroundings. For example, nanostructured ZnO is currently employed as a photoanode material in Dye-Sensitized-Solar-Cells (DSSC) where the surface area is of critical importance in order to increase the efficiency of the cells [40]. Moreoever, the electrical properties of nanostructures are sensitive to adsorbed species: this effect has already been exploited for the preparation of single nanowire gas sensors [41]. Since the conductivity of ZnO nanostructures is also influenced by adsorbed bio-molecules, efforts have been made in the last few years in order to develop ZnO biosensors [42].

Chapter 2

Characterization Techniques

In this chapter we will present the techniques adopted in this thesis work for the characterization of nanostructured ZnO. Particular attention will be devoted to electron microscopy, the most important tool for the analysis of morphology and crystalline structure at the nanoscale. In the second part of the chapter, a brief description of X-Ray Diffraction will be given. Finally, an overview of the electrical characterization techniques will be presented.

2.1 Electron Microscopy

Since the advent of nanotechnology, electron microscopy has become the most important technique for the analysis of the morphology and crystalline structure of materials down to the nanometer scale. Electron microscopes use accelerated electrons as source radiation for the production of images (IMAGING) and for the analysis of crystalline structure, chemical composition and many other characteristics of the sample. There are two major types of electron microscopes: the Scanning Electron Microscope (SEM) and Transmission Electron Microscope (TEM), differing in their mode of operation. There are many reasons for the widespread use of electron microscopes in the fields of materials science and nanotechnology. First of all, electron microscopy has an intrinsic advantage with respect to optical microscopy: better resolution. In fact, the maximum achievable resolution in optical microscopy is $\approx 200\ nm$; this limitation arises from the Rayleigh criterion, which essentially states that the smallest distance that can be resolved is comparable with the minimum wavelength of the radiation. For comparison, the *de Broglie* wavelength of electrons accelerated to $E = 100keV$ is $\approx 4pm$, meaning that *in principle* electron microscopes can resolve details at the sub-atomic level. Another advantage of the electron radiation is that it produces a wide range of secondary signals, which can be used for imaging and analytical purposes. Furthermore, since the wavelength of the electrons can

resolve inter-atomic distances, the crystalline structure of the sample can be investigated with transmission electron microscopes through electron diffraction. In this section, we will introduce the basic concepts of electron beam interaction with matter and we will briefly present Scanning Electron Microscopy and Transmission Electron Microscopy.

2.1.1 Electron-beam interaction with matter

Understanding the interaction of an electron beam with matter is of pivotal importance in order to correctly interpret SEM and TEM images. As low-mass negatively-charged particles, electron are extremely sensitive to the Coulombic field generated by the electrons and the nuclei that constitute the atoms. The interaction of the electrons with the atoms can deflect the electron trajectories and it can cause changes in their kinetic energy of the electrons, through scattering processes. Scattering processes are grouped in two categories:

- *elastic scattering*: electron trajectories are deflected but the kinetic energy is conserved.
- *inelastic scattering*: alongside deflection of their motion, electrons experience energy loss

For any scattering event, the probability of that event happening can be encoded in a quantity called *cross section* (usually denoted by σ), which has units of area. When the electron beam impinges on the surface of the sample, electrons start to experience a sequence of elastic and inelastic scattering events; the initial electron distribution at the surface of the sample changes as electrons are scattered over a $3D$ volume inside the sample (the *interaction volume*). The propagation of the electrons in the sample can end in two different ways:

- some electrons are scattered outside the sample (*back-scattered electrons*)
- the other electrons loose all their energy through inelastic scattering events, creating an excess of electric charge in the sample. In electron microscopes, an electrical connection is established between the sample and the ground; therefore, if the specimen is conductive, there is no accumulation of charge. However, this connection cannot be established if the sample is non-conductive and electric charge accumulates in the sample.

In the following subsections, details on the elastic and inelastic scattering will be discussed and further insight on the interaction volume will be presented.

Elastic scattering

Elastic scattering is by definition a process in which the kinetic energy of a particle is conserved; therefore, it can only cause deflections in the electron trajectories. Elastic scattering events can be divided into two groups:

- scattering from single atoms (*Rutherford scattering*)

- collective scattering from many atoms (*electron diffraction*)

Rutherford scattering is caused by the interaction of a single electron with a nucleus and its cross section can be written as

$$\sigma_{nucleus} = 1.62 \cdot 10^{-24} \frac{Z^2}{E_0^2} cot^2(\theta/2) \quad [m^2] \tag{2.1}$$

for deflection angles $> \theta$. Expression 2.1 is therefore dependent on the energy of the electrons E_0, the atomic number of the atom Z and the scattering angle θ. By taking a look at figure 2.1, it is clear that the Rutherford cross section decreases by several orders of magnitude as the scattering angle increases, meaning that Rutherford scattering is most likely to happen in the forward direction. As

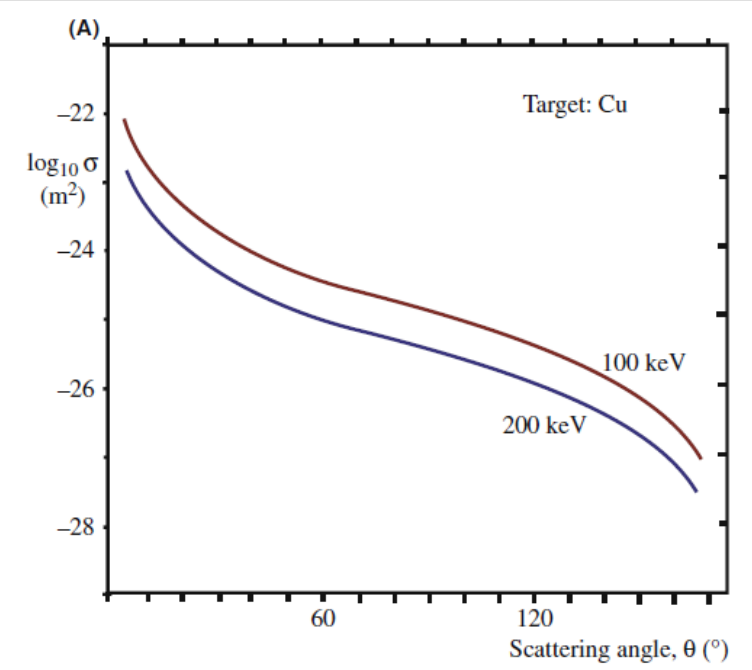

Figure 2.1: dependence of the Rutherford cross section on the scattering angle for two different electron energies [43]

every elementary particle, electrons exhibit wave-particle duality: therefore, we can consider the electron beam as composed by a succession of particles or by a number of waves. While Rutherford scattering can be explained by the particle picture, we have to take the wave-like nature of the electrons into account in order to explain electron diffraction. When the electron beam strikes on a crystalline sample diffracted beams of equal energy are generated; the direction and intensity of the diffracted beams depend on the particular crystalline structure of the specimen. This form of elastic scattering is of major importance in

Transmission Electron Microscopy, because the wavelength and the typical interatomic distances are of the same order of magnitude.. The relation between the energy of the electrons, the interplanar distance of a particular family of crystalline planes, and the scattering angle is encoded in Bragg's law:

$$n\lambda = 2dsin\theta_B \tag{2.2}$$

with λ the de Broglie wavelength of the electrons, d interplanar spacing, θ_B the Bragg angle and n the order of the reflection.

Inelastic scattering

Inelastic scattering processes can be divided into four groups:

- processes that generate X-rays (characteristic x-rays and bremsstrahlung radiation
- emission of Auger electrons
- processes that generate secondary electrons
- collective interactions with many atoms or electrons (plasmon or phonon excitation)

The Coulombic field of the atoms in the sample can induce deceleration of the beam electrons, decreasing their initial energy by an amount ΔE. This energy loss causes the emission of a photon with corresponding energy $\Delta E = h\nu$, with h Planck's constant and ν frequency of the electromagnetic radiation. The energy loss ΔE can take any value up to the total initial energy of the electron E_0. Therefore, when the electron beam interacts with the sample, electromagnetic radiation with energies continuously varying in the range $(0 - E_0)$ is produced. The intensity of this continuum electromagnetic radiation (called *Bremsstrahlung radiation*) can be calculated with the following equation

$$I_{cm} = i_p \bar{Z} \frac{E_0 - E_\nu}{E_\nu} \tag{2.3}$$

where i_p is the electron current impinging on the specimen, $\bar{Z}$ is the average atomic number and E_ν is the emitted photon energy. A beam electron can also interact with inner-shell electrons of the atoms, causing the ejection of an electron from the shell and leaving the atom in an excited state. The atom then relaxes to its ground state through a set of allowed electronic transitions; the energy corresponding to the electronic transition is emitted as a photon. The energy balance of the entire phenomenon is

$$E_\nu = E_I - E_{II} \tag{2.4}$$

with E_ν photon energy, E_I the energy of the electron ejected from the core shell, E_{II} the energy of the electron from the outer shell involved in the electronic

transition. The energy difference between shell I and II can also be transferred to another outer shell electron, ejecting it from the atom with a specific kinetic energy. The kinetic energy of this electron (the *Auger electron*) is

$$E_{kin} = E_I - E_{II} - E_{III} \tag{2.5}$$

The energies involved in the Auger emission and characteristic X-ray production are specific for a given chemical element; therefore measurements on the Auger electrons and characteristic X-ray energies are used to identify the chemical composition of the sample. The two phenomena are in competition and it results that the probability of having an Auger electrons is higher for low Z elements while X-ray production is favored in heavy atoms.

The interaction of the electron beam with matter can cause the emission of electrons from the valence band or conduction band. These electrons are called *secondary electrons* and they usually have energies $< \ 50\ eV$; unlike Auger electrons, they do not carry specific elemental information.

Plasmon and phonon excitations caused by the electron beam can be seen as collective phenomena because they involve many electrons and many atoms, respectively. Plasmons can occur in any material with loosely bound electrons and they can be interpreted as oscillations of the free-electron density; plasmon excitations are quantized and they occur in the eV energy scale. Phonon excitation are related to beam-induced vibrations and subsequent heating of the sample; phonon transition energies are typically $< \ 0.1\ eV$.

Interaction volume

As it was previously stated, when the beam electrons are scattered through the specimen, they either escape the sample (back-scattered electrons) or they loose all their energy by inelastic scattering. The $3D$ distribution of the electrons in the sample is called the interaction volume. A rough estimate of the depth of the interaction volume can be obtained by integrating the Bethe expression for the energy loss over a suitable energy range

$$\frac{dE}{ds} = -7.85 \cdot 10^4 \frac{Z\rho}{AE} \ln\left(\frac{1.166E}{J}\right) \qquad [keV/cm] \tag{2.6}$$

with N_0 Avogadro's constant, Z atomic number, ρ density (g/cm^3), A atomic weight (g/mol), E electron energy, $J = (9.76Z + 58.5Z^{-0.19}) \cdot 10^{-3}\ keV$ the average loss in energy per event. When the specimen is thinner than the interaction volume, some electrons can escape the back-surface of the sample (*trasmitted electrons*); these electrons are extremely important in Transmission Electron Microscopy. Monte Carlo simulations can be performed in order to understand the energy and atomic number dependence of the electron interaction volume (examples are presented in figure 2.2). As a basic rule, the higher the beam energy, the larger the size of the interaction volume and the deeper electrons penetrate in the material. Moreover, higher average atomic numbers lead to smaller interaction volumes with almost hemispherical shape. The inelastic

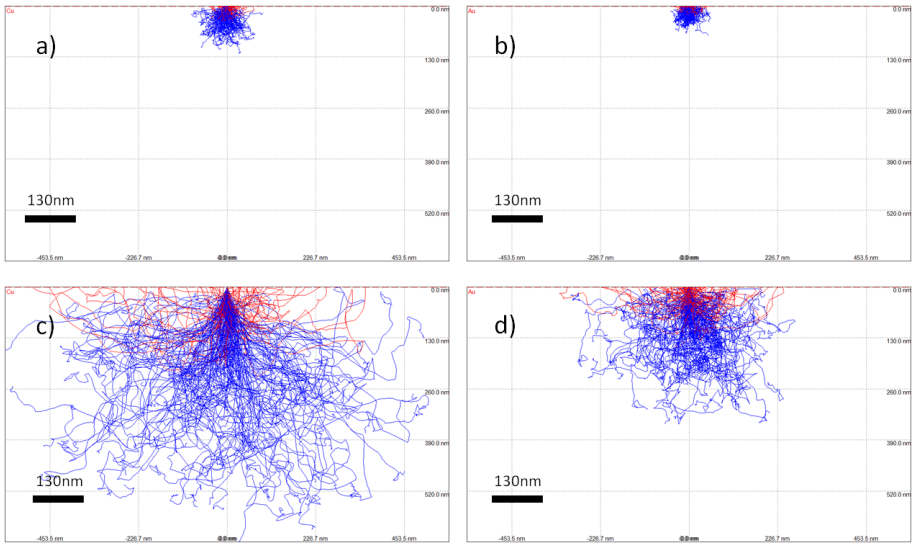

Figure 2.2: Electron interaction volume dependence on beam energy and atomic number. Left column shows the interaction volume in Cu (Z = 29) for beam energy 5 keV a) and 15 keV b). The right column shows the interaction volume with Au (Z = 79) with the same beam energies. The interaction volumes were calculated with the software *Casino* [44]; backscattered electrons trajectories are shown in red

scattering processes that were introduced in the previous section do not occur at the same rate at a fixed depth in the sample; in fact, some depth regions of the interaction volume are usually dominated by one main inelastic scattering process, as it is shown in figure 2.3. Basically, different signals carry information which show to some extent depth-localization. Moreover, it is worth noticing that by reducing the beam energy we can reduce the interaction volume and therefore have better localization of the information. Taking the whole picture into account, the elastic and the inelastic interactions of the electron beam with the sample generate different signals which can be used for different applications. The most important signals in Electron Microscopy are:

- secondary electrons, back-scattered electrons, transmitted electrons: they are commonly used for the construction of images
- characteristic X-rays: essential for a quick elemental analysis of the sample

2.1.2 Scanning Electron Microscopy

The scanning electron microscope (SEM) is the ideal instrument for the observation and characterization of materials down to the micro-nanometer scale. The recorded signals, namely the secondary electrons, backscattered electrons and photons, can be used to produce an image of the specimen or to investigate its chemical composition [45]. Images are obtained by raster scanning a

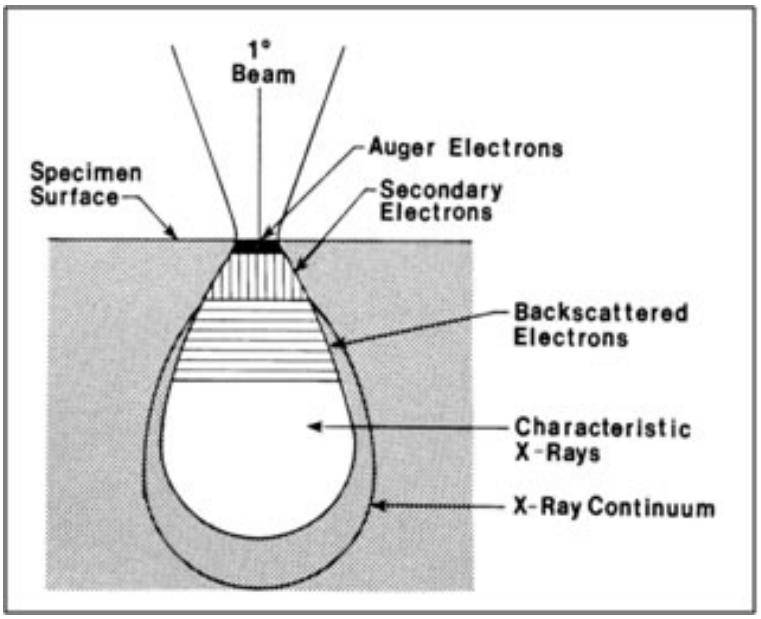

Figure 2.3: electron interaction volume

finely focused electron beam onto the surface of the specimen and recording secondary electrons or backscattered electrons signals. Chemical information can be gained by the analysis of the X-rays produced by the interaction of the electron beam with the specimen, by Energy Dispersive X-ray Spectroscopy (EDX) or Wavelength Dispersive X-ray Spectroscopy (WDX).

Working principles

The SEM can be divided into three main parts:

- the electron column, where the electron beam is produced and focused, under High-Vacuum (HV) conditions (pressure $< 10^{-8} Torr$)
- the chamber, where the samples and the detectors are kept under vacuum conditions
- the controls and the computer interface

The basic components of a SEM are the electron gun, the electromagnetic lenses and the detectors; their function and their principle of operation will be explained in the following sections. The electron gun is the part of the microscope which is responsible for the production of a stable beam of electrons with selectable energy: the gun generates the electrons and accelerates them to a suitable energy, usually in the range (0.1 - 30) keV, in UHV conditions. The

electron gun is in general composed of a electron emitter serving as the cathode, a Wehnelt cap as control electrode and a anode electrode; an example is presented in figure 2.4. There are four types of electron emitters which are com-

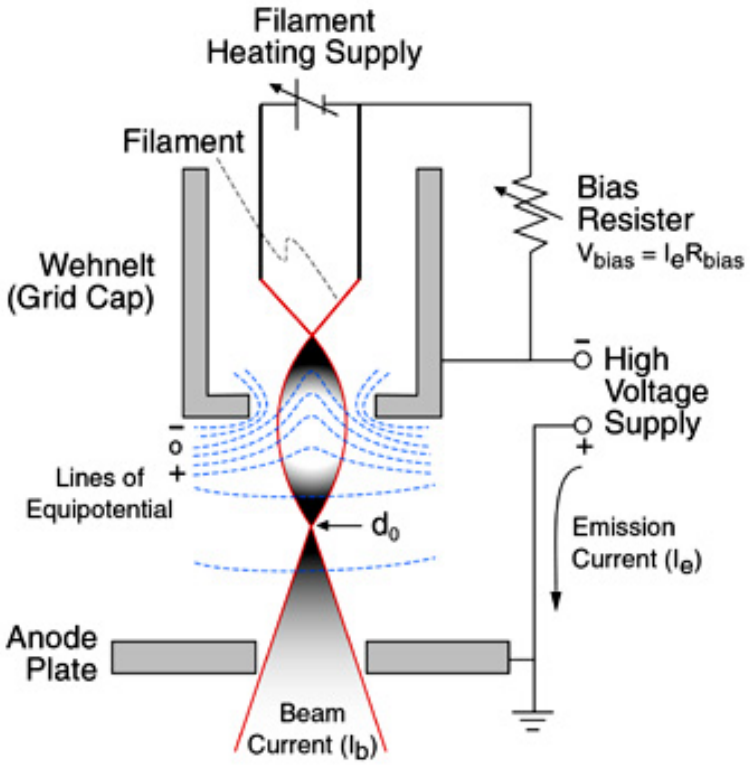

Figure 2.4: conventional tungsten hairpin electron gun [45]

monly used in electron microscopes, differing in materials and in the physical phenomena exploited for the emission of electrons [46]:

- *Tungsten hairpin*: a tungsten wire of about 100 μm in diameter is bent into a V-shaped hairpin; the filament is heated through Joule effect and thermoionic electrons are emitted from the tip
- *Lanthanum hexaboride*: a single crsytal of LaB_6 is used as the emitter; since the work function of LaB_6 is lower than W, more electrons are emitted
- *Cold tungsten field emission*: the field emitter is a sharp tip ($< 100\ nm$) of W which is kept at room temperature; electrons are extracted by field emission
- *ZrO/W Schottky emitter*: ZrO is used to lower the work function of the emitter; field emission is boosted by heating the emitter

A SEM equipped with a field emitter is called Field-Emission Scanning Electron Microscope (FESEM). The most important parameters in comparing electron guns and evaluating their performances are the following: brightness, optical radius and energy spread. The brightness β is defined as the beam current per unit area per solid angle and it is usually expressed in $A\ cm^{-2}sr^{-1}$ units:

$$\beta = \frac{4i_p}{\pi^2 d_p^2 \alpha_p^2} \tag{2.7}$$

with i_p the electron probe current, d_p the electron probe size and α_p the beam convergence angle. An important property of brightness is that ideally it is conserved at any point in the column of the electron microscope: as a consequence, measurements performed on the electron beam at the specimen level can be used to estimate the electron gun brightness. The optical radius is the radius of the electron beam when it exits the electron gun and the energy spread is in most cases defined as the energy interval containing 50% of the electrons emitted. Brightness is the most important estimator of a gun performance: the higher the brightness, the higher the resolution one can achieve with perceptible signal-to-noise ratio. It can be seen from equation 2.7 that higher i_p (proportional to signal-to-noise ratio and generation of contrast in the image) leads to higher values of d_p, which is inversely proportional to the maximum achievable resolution; therefore instruments with higher brightness can in principle achieve better performances. It must be also stressed that brightness increases linearly with the accelerating voltage: this is the reason why brightness values for different instruments must be compared at the same accelerating voltage. Table 2.1

Table 2.1: Comparison of Electron sources at 20kV [46]

Source	Brightness	Optical radius	Energy spread
tungsten hairpin	$10^5\ A\ cm^{-2}sr^{-1}$	$(30 - 100\ \mu m)$	$1 - 3$ eV
LaB_6	$10^6\ A\ cm^{-2}sr^{-1}$	$(5 - 50\ \mu m)$	$1 - 2$ eV
Cold tungsten	$10^8\ A\ cm^{-2}sr^{-1}$	$< 5\ nm$	0.3 eV
Schottky ZrO-W	$10^8\ A\ cm^{-2}sr^{-1}$	$15 - 30\ nm$	$0.3 - 1.0$ eV

shows that Schottky emitters are currently the best emitters for high-resolution imaging especially at low voltages due to their superior brightness.

Once the electron beam is generated by the electron gun, electromagnetic lenses are used to control the path of the electron beam along the column of the SEM, which is kept in HV conditions in order to avoid scattering with air molecules which could randomize the electron trajectories. Since electrons are charged particles, their motion can be easily controlled by electromagnetic fields, which in turn can be tuned by varying the current flowing in coils placed in a ferromagnetic material. This is the basic working principle of all electromagnetic lenses employed in SEMs. The remarkable thing is that the motion of the electrons of the beam in the presence of electromagnetic lenses can be treated by geometrical arguments and the electron beam can be modeled as a set of

rays with different directions. The focal length of an electromagnetic lens can be calculated from the usual equations for thin lenses in geometrical optics:

$$\frac{1}{f} = \frac{1}{p} + \frac{1}{q} \tag{2.8}$$

with p and q the distance from the object and from the image to the center of the lens, respectively. The focal length of the electromagnetic lenses can be changed by changing the current which is flowing in the coils, so that fine-tuning of focus independent of the sample position is possible. However, one disadvantage of electromagnetic lenses is that aberrations cannot be canceled by combination of lenses but can only be minimized. The most important aberrations in electromagnetic lenses are:

- *spherical aberration*: electrons whose trajectories are further away from the optic axis are bent more strongly toward the optical axis, meaning that electrons at different distances from the optic axis will be focused to different planes. Thus, object points become disks in the image plane and the image is blurred. The diameter of the disk, described as disk of least confusion, can be written as

  $$d_s = \frac{1}{2} C_s \alpha^3 \tag{2.9}$$

  with C_s the spherical aberration coefficient and α is the angle of convergence (or divergence) through the lens.

- *chromatic aberration*: electrons with different energies are focused at different locations in the image plane and a point object is imaged as a disk. The diameter of this disk is expressed as

  $$d_c = C_c \alpha \frac{\Delta E}{E_0} \tag{2.10}$$

  where E_0 is the nominal energy of the electron beam and ΔE is the energy spread of the electron gun.

- *astigmatism*: the lack of perfect cylindrical symmetry along the optical axis leads to this aberration, which manifests itself by the presence of two line of focus at different heights. Practically, image points are stretched into lines on one side of focus and into perpendicular lines on the other side of focus; at exact focus the image is not stretched but it is blurred. Astigmatism can be corrected using stigmators, which supply small magnetic fields that restore cylindrical symmetry in the lens.

- *aperture diffraction*: as a consequence of the wave-like nature of electrons, very small apertures can give rise to a circular diffraction pattern instead of a point in the image plane. The diameter of the Airy disk, which is the first, more intense diffraction ring, is given by:

  $$d_d = \frac{0.61\lambda}{\alpha} \tag{2.11}$$

The most important lens in the SEM is the final lens (the objective lens), which controls the size of the electron probe while focusing the electron beam on the specimen. Two sets of electromagnetic coils are placed inside the bore of the objective lens: these coils are responsible for the scanning action of the beam over the surface of the sample, which is necessary for the formation of the image. A digital image is basically a array (x, y, S) stored in computer memory, where (x, y) are the position coordinates and S is the signal intensity. In SEM, (x, y) are actual positions on the specimen and the signal S is the digitally-converted intensity of any signal generated by the interaction of the electron beam with the specimen. The correspondence between the (x, y) values in the computer memory and the actual positions on the specimen is ensured with a digital-to-analog converter which converts each scan position into a voltage that drives the scan circuit: there is a one-to-one relation between pixels in the image and positions on the specimen. The magnification M is defined as the square root of the ratio between the area of the screen and the scanned area on the sample:

$$M = \sqrt{\frac{A_{screen}}{A_{sample}}} \tag{2.12}$$

It must be stressed that changing magnification in a SEM image is obtained by changing the scanned area on the specimen, while keeping the number of pixels constant. In fact, higher magnification images are created by raster-scanning the beam on smaller areas of the sample.

The digitalized signal S values are usually displayed as gray levels and therefore the majority of SEM images are black-and-white images. Usually, there are two main signals used for the construction of SEM images: secondary electrons (SEs), back-scattered electrons (BSEs) or a combination of both. Three factors influence the construction of the image:

- the specific signal used for the image
- the position of the sample relative to the beam
- the position of the detector relative to the sample

The energy distribution of the electron signal produced by beam electrons with energy E_0 is shown in figure 2.5. It must be stressed that the distinction between SEs and BSEs is set to $50eV$ *by convention*. In fact, this conventional definition is not completely in accordance with the definition of backscattered electrons that was given in section 2.1.1: for example, although Auger electrons have typical energies $> 50\ eV$, they are not actually backscattered electrons. Moreover, there can in principle be backscattered electrons with energy $< 50\ eV$. However, the afore-mentioned conventional definition based on the energy distribution is extremely useful for the majority of applications, since actually most of the electrons with energy $< 50\ eV$ are in fact secondary electrons. The total electron yield can be expressed as

$$\sigma \equiv \frac{I_{emitted}}{I_{probe}} = \frac{I_{SE}}{I_{probe}} + \frac{I_{BSE}}{I_{probe}} \equiv \delta + \eta \tag{2.13}$$

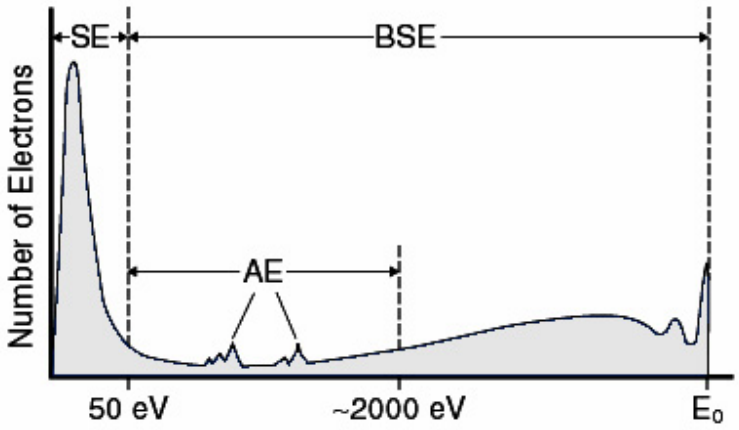

Figure 2.5: Energy distribution of the electron signal produced by the interaction of an electron beam with initial energy E_0 with the sample

with δ the secondary electron coefficient and η the backscattered electron coefficient. SEs are loosely bound electrons which receive sufficient kinetic energy during inelastic scattering to escape the surface of the sample. In general, the kinetic energy of the SE electrons is $< 50eV$; as a consequence, only those electrons near the surface have sufficient energy to reach the surface and overcome the work function of the sample. In fact, as it is shown in figure 2.3, the *detectable* SEs are mainly produced near the surface of the sample and therefore they are collected for the construction of images carrying information about the surface morphology. The SE coefficient dependence on the tilt angle θ of the sample is:

$$\delta(\theta) = \delta_0 sec(\theta) \tag{2.14}$$

Although the coefficient δ increases with increasing tilt, their angular distribution remains the same, since the generation of SEs is isotropic; as a consequence, SE-generated images are not ideal for topographic information of the surface. Backscattered electrons (BSEs) usually experience many elastic scattering events and therefore BSE production is highly dependent on the atomic number (equation 2.1); the BSE signal is used for the acquisition of Z-contrast images. The coefficient η increases with increasing sample tilt angle θ:

$$\eta(\theta) = \frac{1}{(1 + cos(\theta))^{9/\sqrt{Z}}} \tag{2.15}$$

with Z the atomic number. Moreover, the angular distribution is peaked in the direction normal to the surface:

$$\eta(\phi) = \eta_n cos(\phi) \tag{2.16}$$

with η_n the value measured along the normal to the surface and ϕ the angle with respect to the normal. Therefore, contrary to the case of SEs, great information

about the topography of the surface can be acquired by BSEs images. Specific detectors are used to collect the different electron signals; the most important detectors are the Everhart Thornley detector, the through-the-lens detector and the back-scattered electron detector.

- Everhart-Thornley (ET) detector: it is the most commonly used detector in SEMs. The ET detector consists of a scintillator which converts the electron signal into photons, amplifies the signal with a photomultiplier tube and converts it back to an electron signal. The detector is placed inside the chamber of the microscope on one side. A Faraday cage around the detector enables positive or negative biasing (typically in the range $(-50 \div 250)\ V$). In the negative bias mode, only backscattered electrons are detected, while in the positive bias mode both BEs and secondary electrons are detected.

- through-the-lens detector: this detector is placed inside the objective lens and collects SEs producing high-resolution images with exceptionally high signal-to-noise ratio

- Backscattered-electron detector: dedicated solid-state back-scattered electrons are placed over the specimen, in order to have better collection efficiency with respect to the negatively-biased ET detector

Resolution in images can be defined as the minimum spatial spacing at which two different features of the sample can be recognized as distinct. The lower limit to this distance is of course set by the beam size, which is one major factor of influence of the resolution. However, the beam interacts with the sample over a 3D volume which is much larger than the beam size and which is dependent on beam energy and sample composition. Moreover, the visibility of features in the image is determined by contrast and contrast is influenced by the brightness (monotonic function of the accelerating voltage) of the gun, by the particular choice of detector and by its position relative to the sample. The best resolution can therefore be ideally achieved by the smallest beam size possible, with the highest brightness possible, with the smallest interaction volume possible. These conditions can actually be approached with thin samples (thickness $<$ 150 nm) in Scanning Transmission Electron Microscopes (STEM, see section 2.1.3). FESEMs can reach $1nm$ resolution in optimal conditions with bulk samples. Most SEMs are equipped with a X-ray detector,in order to gain chemical information by the analysis of the characteristic x-rays production, with a technique called Energy Dispersive X-ray Spectroscopy (EDX). Moreover, by combining the scanning capability of the SEM with X-ray detector, elemental maps can be obtained.

2.1.3 Transmission Electron Microscopy

Transmission electron microscopy is a powerful technique which permits the investigation of the crystalline structure of materials at the nanometer scale

and imaging of materials at atomic resolution. As the name suggests, TEM operation modes rely on the collection of transmitted electrons; therefore, TEM samples must be very thin (usually with thickness $< 150nm$) in order to have a significant amount of transmitted electrons. This is a major limitation of transmission electron microscopy and a lot of efforts have been and are currently made in order to develop efficient procedures for TEM sample preparation.

Working principles

The main components of a TEM are:

- the electron gun: currently ZrO/W Schottky emitter or Cold Field emitters are used for the production of the electron beam in high-resolution microscopes, due to their high brightness (table 2.1). However, TEMs with tungsten hairpin and Lanthanum hexaboride emitters are still commercially available
- the electromagnetic lenses: as in SEMs, the electron beam is controlled by the action of electromagnetic lenses; however, in TEM there are lenses even *below* the sample. Some TEMs are equipped with scanning coils and Scanning Transmission Electron Microscopy (STEM) is possible
- the sample holder: there are different holders, giving rise to the possibility of moving the sample in different ways. Some holders allow for in-situ thermal or mechanical stimulation of the specimen
- the fluorescent screen and the detectors: the image or the diffraction pattern of the sample can be viewed on a fluorescent screen or they can be recorded by using a CCD camera. Different specific detectors can be mounted inside the TEM column for imaging and analytical purposes, such as annular dark field detector for STEM imaging or EDX detector for elemental analysis
- the controls and the computer interface
- the vacuum system: the TEM is kept permanently under vacuum; the electron gun and the electron column are kept in UHV conditions

The optical system of the TEM can be divided into three parts, depending on their function:

1. the illumination system: it comprises the gun and the condenser lenses; it determines the beam conditions above the specimen (convergence angle, current)
2. the objective lens: it is the most important lens in the TEM because it forms the images and the diffraction patterns
3. the projection system: it magnifies and projects images or diffraction patterns onto the fluorescent screen

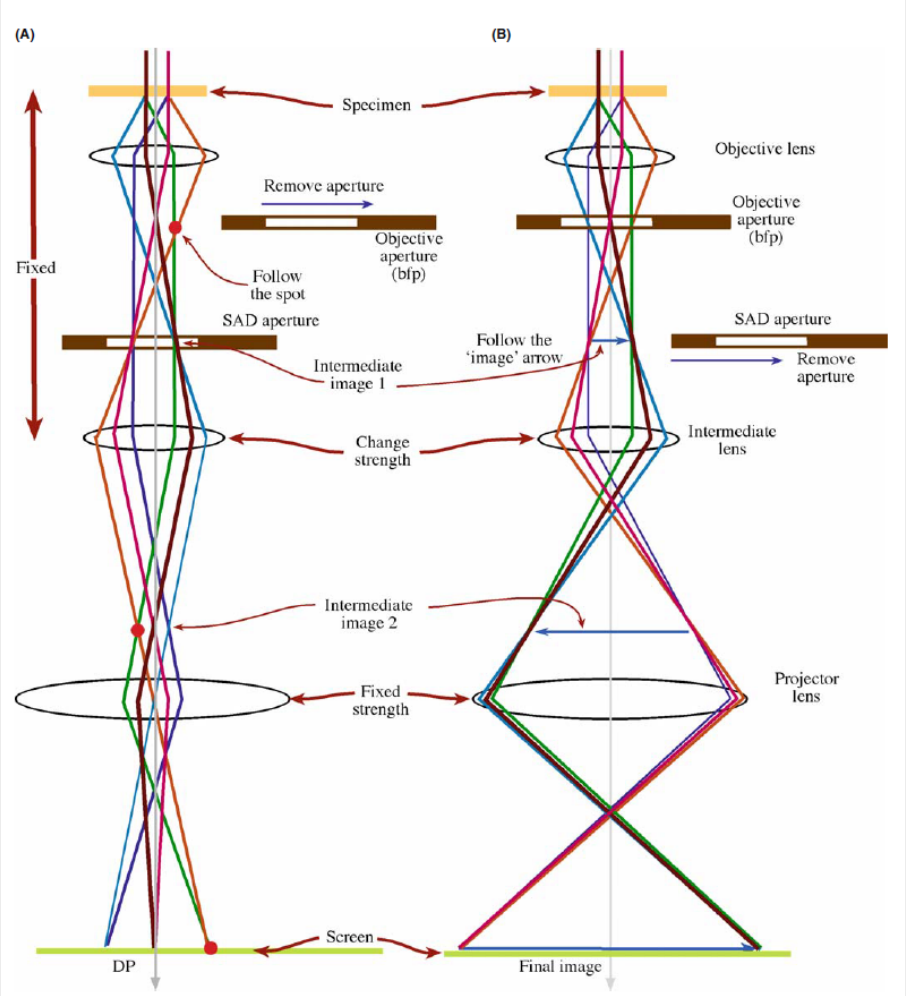

Figure 2.6: a) schematically shows the TEM diffraction mode, while b) shows the conventional TEM Bright-Field mode for imaging [43]

The different modes of operation in TEM are obtained by the interaction of the three parts of the optical system; the most important modes will be briefly presented in the following paragraphs.

Diffraction mode

As was already mentioned in section 2.1.1, the beam electrons undergo elastic scattering events in the specimen which are influenced by the crystalline structure of the sample. As a consequence of the wave-like nature of the electrons, diffraction of the electron beam takes place. Basically, the initial electron beam is diffracted into different transmitted electron beams, whose direction of propagation is related to the crystalline structure of the material under analysis. In analogy with X-Ray Diffraction, the electron beam is diffracted into directions selected by Bragg's law (equation 2.10). However, since the sample is so thin (usually $< 100nm$), the diffraction conditions imposed by Bragg's law are slightly relaxed and diffraction is possible even though the Bragg's law is not exactly satisfied. In order to get the sharpest diffraction patterns possible, parallel beam illumination is essential. Although it is not possible to achieve perfectly parallel beam condition, the illumination system is set in order to reduce the convergence of the beam impinging on the specimen. The diffracted beams emerging from the specimen are converged in the back focal plane of the objective lens: beams coming from different points in the back-surface of the sample with the *same* direction are focused into the same point in the back focal plane. In fact, the electron diffraction pattern is formed in the back focal plane by the objective lens. In order to see the diffraction pattern, the projecting system is set to DIFFRACTION MODE and it projects the pattern onto the fluorescent screen or to a CCD camera. The projecting system allows for different magnifications of the diffraction pattern which are labeled as camera lengths, in analogy with X-ray diffraction. The diffraction beam contains structural information of the whole illuminated area; in order to localize the information, one must reduce the illuminated area. The illuminated area can be reduced by increasing the convergence of the beam, in a technique called Convergent-Beam Electron Diffraction [43]. However, converging the beam destroys parallelism and the diffraction pattern consists of disks instead of sharp spots. The only way to preserve parallelism while reducing the area is to place an aperture in the image plane of the objective lens. This operation produces a virtual aperture in the object plane of the objective lens (which coincides with the sample); therefore, an area on the specimen is selected by the so-called Selected Area Aperture (SAA). The use of the SAA is the most common technique for the acquisition of electron diffraction patterns in TEM.

BF and DF imaging

As it was previously stated, the sample lies in the object plane of the objective lens and therefore it is imaged in the image plane of the objective lens. In the IMAGING mode, the projector system is adjusted so that the image plane of

the objective lens is magnified and projected onto the fluorescent screen or the CCD camera. All the information in the image is carried by the transmitted beam and the diffracted beams emerging from the back-surface of the sample. All these beams are focused in different spots at the back focal plane of the objective lens, depending on their direction. By placing an aperture in the back focal plane, we can select beams with specific directions and construct the image just with those beams. The contrast will obviously be influenced by the choice of the spots in the back focal plane. There are many possibilities for the selection of the beams:

- only the transmitted beam: this the pure Bright Field (BF) mode. Pure BF images are dominated by mass-thickness contrast, since the intensity of the transmitted beams is highly influenced by Rutherford scattering, which is dependent on the atomic number (equation 2.1). Moreover, in the regions where the specimen is thicker, there will be more elastic scattering processes (equation 2.1).
- transmitted beam + some diffracted beams: the contrast in the image is by influenced thickness, atomic number and by the diffracted beams, carrying structural information
- only one ore more diffracted beams: this is the Dark Field (DF) mode. Regions which contribute to the diffraction of the selected beam will exhibit brighter contrast. These imaging mode is extremely helpful in the analysis of polycrystalline materials.

STEM and analytical analysis

Some TEMs are equipped with scanning coils and the beam can be raster-scanned on the surface of the sample. The transmitted electrons signal is revealed by suitable detectors and images can be constructed by creating (x, y, S) arrays, where (x, y) is the position on the sample and S is the intensity of the detected signal. The magnification is dictated by the dimension of the scanned area. In the STEM mode, the objective lens and the projection system do not influence the image; the quality of the image is a consequence of the quality of the probe. The electron probe must have high current confined in small size, in order to achieve good resolution with reasonable signal-to-noise ratio. The position of detectors determines the contrast in STEM images; the most popular detector is the high-angle annular dark field detector, which is used for Z-contrast imaging [47]. As in SEMs, the scanning capability of STEMs can be used for the construction of analytical maps, such as EDX maps or Electron Energy Loss Spectroscopy (EELS) maps.

2.2 Focused Ion Beam

The Focused Ion Beam (FIB) is from an operational point of view very similar to the SEM, the main difference being that the focused beam consists of ions

instead of electrons. In commercially available instruments, Gallium (Ga) is the most employed element as source of ions; however, Helium (He) sources are recently being employed for focused ion beam imaging applications ([48], [49]). The FIB has three main functions: imaging, etching, deposition. Particularly useful for applications is the combination of a SEM column and a FIB column in a single system, which is generally referred to as a dual-beam FIB-SEM system.

2.2.1 Ion interaction with matter

Since ions have a mass which is several orders of magnitude greater than electrons, the interaction of the ions with matter is much more destructive; in fact, most of FIB applications are based on this concept. As was the case for beam electrons, the impinging ions can be backscattered or they can loose all their energy by inelastic scattering and be implanted in the sample. Inelastic scattering events can result in the production of phonons, plasmons, photons and in the emission of secondary electrons, secondary ions and sputtering of atoms from the sample. When an ion beam impinges on the surface of a sample, the ions

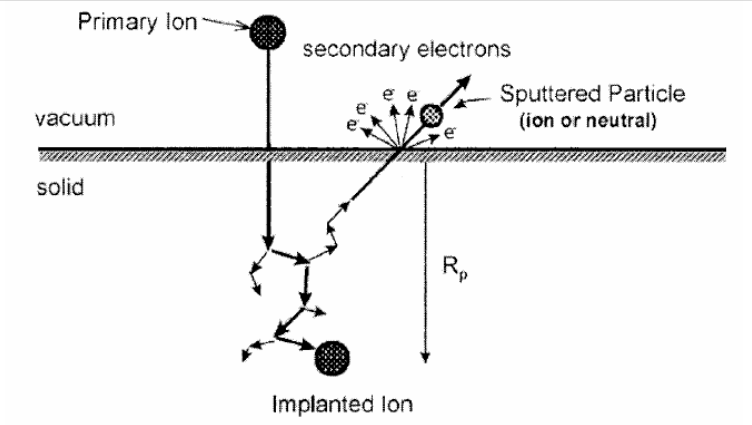

Figure 2.7: Schematic representation of the interaction of the ion beam with matter [50]

loose their energy through two different classes of inelastic scattering events:

- scattering with nuclei
- scattering with electrons

The rate of energy loss per unit path length dE/dx has therefore both nuclear and electronic contributions; however, nuclear energy losses dominate in typical FIB processes [50]. As was previously said, the most important aspect of the ion-matter interaction is that atoms can be sputtered away from the material. This phenomenon is represented through a *collision cascade model*: target atoms are knocked from their position under ion bombardment and sputtering occurs

if sufficient momentum is transferred from the collision cascade to the surface atoms. The number of ejected particles per incident ion (the sputtering yield Y) depends on:

- the ion beam energy: higher energies usually lead to higher sputtering yields
- the target material: the coefficient Y shows a periodic trend with respect to the atomic number Z of the target material
- incidence angle: the higher the incidence angle, the higher the sputtering yield
- crystalline structure of the target material: ions may penetrate greater distances along specific crystalline directions (ion channeling). Since sputtering is a surface phenomenon, ion channeling decreases the sputtering yield.

2.2.2 Liquid Metal Ion Source

The liquid metal ion source (LMIS) is the source of ions in the FIB; it has the ability to provide a source of ions of ~ 5 nm in diameter [50]. A typical LMIS usually contains a field emitter (a tungsten needle) having a tip radius of $\sim 2-5\ \mu m$, attached to a reservoir that holds the metal source material (which is currently Ga in commercially available FIB systems). The field emitter is heated up to the melting point of the metal source of ions and an electric field (10^8 V/cm) is applied to the tip by the extraction electrode. The liquid Ga is drawn into a conical shape (the *Taylor cone*) as a result of the balance between surface tension and electrostatic forces [51]; the apex of the Taylor cone has $\sim$ 1 - 2 nm radius of curvature [46]). Field evaporation and field ionization take place at the tip as a result of the high electric field applied by the extraction electrode; Ga^+ ions emission occurs and a flow of liquid Ga to the tip continuously replaces the evaporated ions. As in SEM system, the FIB has scanning capability provided through scanning coils. The main difference with respect to the SEM is that the ion beam is focused onto the specimen by an electrostatic lens. The ion current impinging on the surface of the specimen can be controlled through a set of apertures of various diameters.

2.2.3 Applications

Since ions are more massive than electrons, the interaction of the ion beam with the specimen is destructive and most of the applications of FIB are based on this concept. When energetic ions ($30keV$ on most FIBs) reach the specimen, sputtering, ion implantation and amorphization take place. Moreover, ion beam optics are capable of producing nanometer-sized ion probe, making the FIB the ideal (and in some cases the only) instrument for micro and nano-scale machining. Generally, FIB-SEM systems are equipped with gas delivery systems inside

the chamber in order to achieve in-situ deposition of conducting or insulating materials. Typically, a gas precursor is introduced in the chamber through the Gas Injection System (GIS) and site-specific deposition of desired materials is achieved by the interaction of the ion beam (or even the electron beam) with the gas precursor. Basically, a FIB system has three applications:

- IMAGING: the capability of scanning the ion beam and the generation of secondary electrons and secondary ions make it possible to acquire images. Since the ion-induced production of secondary electrons is sensitive to the crystalline structure and orientation of the sample, FIB imaging is particularly useful for the analysis of polycrystalline samples. However, the main drawback with this technique is the continuous change in surface morphology as a consequence of milling induced by the ion beam while raster-scanning.
- SPUTTERING: controlled removal of material at the micro and nanoscale can be achieved. This is especially useful for the preparation of localized cross-sections of the sample or for the preparation of devices at the nanoscale
- DEPOSITION: micro and nano-scale deposition of conducting or insulating material is often used for the preparation of miniaturized proof-of-concept devices or for the preparation of TEM samples

2.2.4 TEM lamella preparation

One of the most important applications of dual-beam instruments is the preparation of TEM samples. The main advantage of this kind of preparation is that it is relatively non-destructive and it allows for the localization of regions of interest at the micrometer scale. Currently the standard TEM sample preparation technique is the *lift-out method*, which essentially consists in the preparation of an electron-transparent lamella that is lifted out of the sample by a manipulator and subsequently attached to a suitable TEM sample holder. The entire procedure is carried out through different steps:

1. at first, a region of interest is identified. If the region near the surface is important for the TEM characterization, a protective layer of Platinum is deposited in-situ. The typical longitudinal size of the layer is $\approx 22\mu m \times 2\mu m$
2. the lamella is created by ion-beam induced sputtering at relatively large ion currents $(4 - 16\ nA, 30keV)$ and it is thinned until it reaches $1.5\mu m$ in thickness
3. frame cuts are performed with lower ion currents $(2nA, 30keV)$
4. the manipulator approaches the edge of the lamella

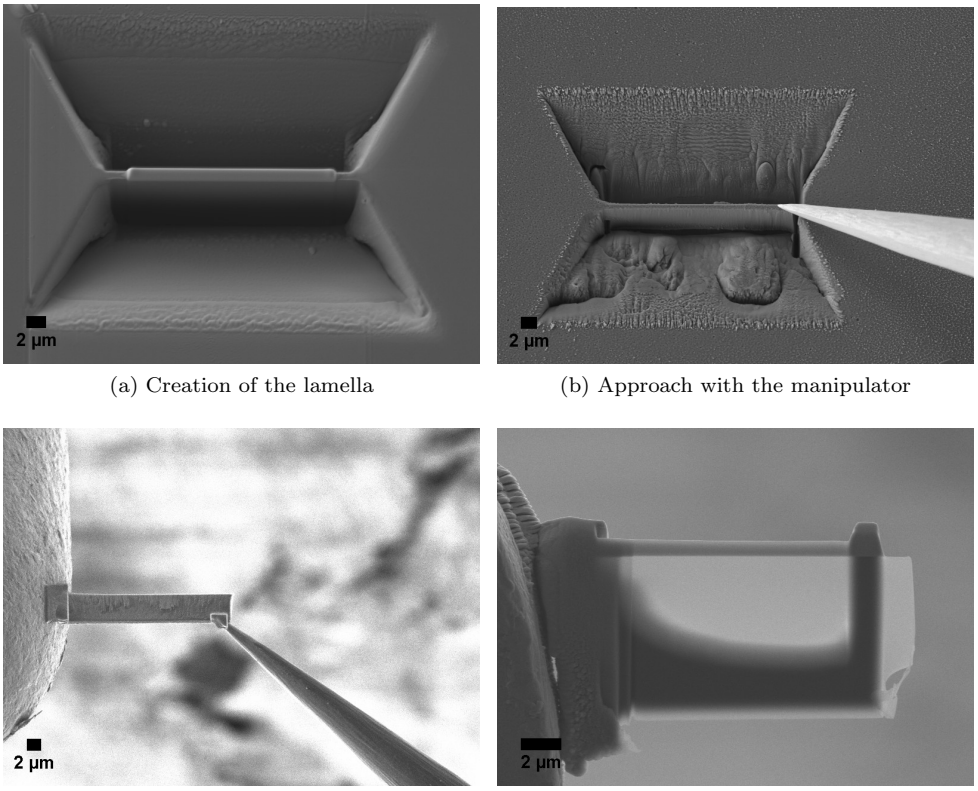

(a) Creation of the lamella

(b) Approach with the manipulator

(c) Attachment to the grid

(d) Electron-transparent lamella

Figure 2.8: Standard lift-out procedure

5. the manipulator is attached to the lamella by in-situ deposition of Pt and the final cut is performed
6. the lamella is attached to the TEM grid by Pt-deposition; the manipulator is detached from the lamella by FIB sputtering
7. the lamella is thinned until it is electron transparent (thickness $< 150\,nm$) with low FIB currents ($50pA, 30KeV$)
8. final cleaning of the lamella is performed at ($2pA, 2kV$); this step is essential for the removal of the amorphous layer induced by the previous steps

2.3 Instrumentation

During this thesis work, the following instruments have been used:

- *FESEM Zeiss Supra 40* at Politecnico di Torino: the microscope is equipped with three detectors: in-lens, Everhart-Thornley and solid-state backscattered electrons detector. Some SEMs morphological characterizations were performed on this microscope.
- *FESEM Zeiss Auriga FIB-FESEM* at Center for Space Human Robotics: this dual-beam instrument is equipped with a ion column at 54° with respect to the electron column. Three detectors are present: in-lens, secondary-electrons-secondary-ions (SESI) detector and a backscattered electrons detector which is placed in the column. In-situ deposition is possible through a 5-channel Gas-Injection-System. Three manipulators can be mounted in the microscope chamber: one is used for the lift-out of lamellae while the other two are employed for electrical characterizations. This microscope was used for the majority of morphological characterizations, for the preparation of TEM lamellae and for the electrical characterization of single nanostructures.

The structural characterization was carried out on a FEI Tecnai G^2 F20 S-TWIN microscope which, alongside the Auriga FIB-FESEM, constitutes the electron microscopy facility of the CSHR. The microscope is equipped with an EDX detector for elemental analysis, EELS spectrometer, Bright-Field (BF), Dark Field (DF) and High-Angle Annular Dark-Field (HAADF) detectors for STEM imaging.

2.4 X-ray Diffraction

X-Ray Diffraction (XRD) is a non-destructive technique which is used for the identification of crystalline phases, orientation and for the determination of structural properties such as lattice parameters, strain, grain size. X-rays are electromagnetic waves whose wavelengths range from about 10^{-11} to 10^{-8} m; they therefore give rise to diffraction patterns whenever they encounter crystalline structures, due to the fact that interatomic distances in crystalline matter are comparable with typical x-rays wavelengths. From a geometrical point of view, X-ray diffraction in matter is encoded in Bragg's law:

$$n\lambda = 2d_{hkl}sin\theta_B \tag{2.17}$$

where λ is the wavelength of the incident wave, n is an integer, d_{hkl} is the spacing between a family of parallel atomic planes in the lattice and θ is the angle between the incident ray and the scattering planes (see Fig. 2.10). Diffraction can occur whenever Bragg's law is satisfied. A typical X-ray spectrum is constructed by plotting the intensity of the X-rays versus the angle of incidence of the X-rays. X-ray spectra exhibit peaks that carry information about the sample; in fact:

- peak position: the position of the peaks is related to the crystalline structure through Bragg's law. Shifts of the position of the peaks with respect to the ideal position carry information about uniform strain in the material

(a) FESEM SUPRA

(b) FIB-FESEM AURIGA

(c) TEM Tecnai

Figure 2.9: Electron microscopes used for the thesis work

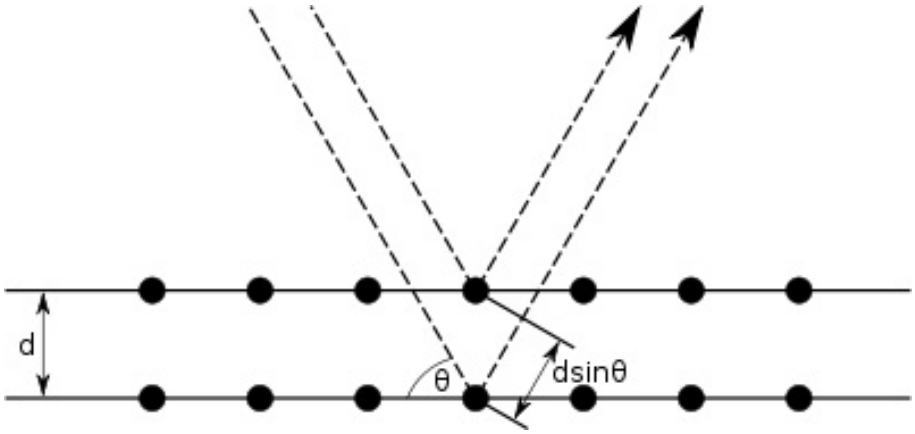

Figure 2.10: Bragg's law

- peak width: it is related to the size of the crystalline grains and to non-uniform strain
- peak intensity: the intensity of the peak is determined by many factors such as geometry, position of the atoms in the cell, sample adsorbance

All the XRD analysis presented in this thesis have been acquired with a Panalytical X'Pert X-ray diffractometer in the Bragg-Brentano configuration, equipped with a $Cu\ K_\alpha$ X-ray source ($\lambda = 1.54059\ \mathring{A}$).

2.5 In-Situ Electrical Characterization

All the electrical characterizations of single nanostructures presented in this thesis (chapter 4), are performed in the dual-beam FIB-SEM chamber; therefore, the data are acquired in high-vacuum conditions ($\approx 8 \cdot 10^{-6}\ Torr$). The contacts to the nanostructures are deposited in-situ by following specific procedures, depending on the particular nanostructure. Detailed description of these procedures will be given in the chapter dedicated to the electrical characterizations (chapter 4). Two micromanipulators (Kleindiek Nanotechnik) equipped with tungsten tips are exploited to establish voltage bias to the previously deposited conductive contacts; therefore, all the nanostructures are characterized by two-terminal measurements. The manipulators can be attached to any Source Measure Unit through BNC connectors.

The electrical behaviour of the nanostructures is studied with two different techniques:

- DC biasing: I-V curves are acquired in order to gain knowledge of the nature of contacts and for the calculation of the linear resistance of the nanostructures. The curves are acquired with a Agilent B2912A precision source measure unit.

- Impedance Spectroscopy: the electrical behavior of the nanostructures is studied under small signal AC polarization at different frequencies. In this way, it is possible to gain knowledge of the capacitive behavior of the nanostructures and it is possible to evaluate contact resistances. The data are acquired by connecting a potentiostat and a frequency-response analyzer to the micromanipulators.

Chapter 3

Characterization of morphology and structure

ZnO in the form of nanostructured thin films or nanowires has been studied at Center for Space Human Robotics (CSHR) in view of tactile sensors and energy harvesting applications. In particular, there are three main technological fields that have been studied:

- *tactile sensors for artificial skin*: tactile sensors can be developed by exploiting piezoelectricty of materials [52]. Since ZnO is both piezoelectric and semiconductor, it can in principle be used for the production of piezoelectric sensors integrated with silicon technology.
- *Dye-Sensitized Solar Cells*: DSSCs are studied as a low-cost alternative to conventional silicon-based photovoltaic devices [53]. As a wide bandgap semicondutor with energy band structure similar to TiO_2, ZnO is an ideal candidate as photoanode material [40]. Moreover, nanostructures fulfill naturally the requirement of high surface area which is essential for dye impregnation.
- *Photoelectrochemical water splitting devices*: ZnO can be used as photoanode material in photoelectrochemical water splitting cells due to its appropriate energy band structure [54]. In addition, as in DSSCs, high surface areas are required for water-splitting applications and therefore ZnO nanostructures are promising candidates

In this chapter we will present the morphological and structural characterization of the different ZnO thin films and nanostructures that have been synthesized at the CSHR, in view of their possible employment in functional devices. The first part of the chapter will be devoted to the characterization of thin films deposited by sputtering with two different morphologies: columnar dense films and porous sponge-like films. The second part of the chapter will be dedicated to microwires

and nanowires synthesized by chemical route and to nanowires grown by Low-Pressure-Chemical-Vapor-Deposition (LPCVD). FESEM characterization was performed on a Zeiss Auriga FIB-FESEM dual beam system and on a Zeiss SUPRA FESEM microscope. TEM characterization was performed with a FEI TECNAI G^2 F20 S-TWIN microscope. XRD spectra were acquired with a Panalytical X'Pert X-ray diffractometer in the Bragg-Brentano configuration, equipped with a $Cu\ K_\alpha$ monochromatic radiation X-ray source ($\lambda = 1.54059\ \mathring{A}$). The JCPDS-ICDD card n. 89-1397 was used for the indexation of ZnO X-ray peaks.

3.1 Columnar thin films

Columnar thin films have been deposited at the CSHR for two main applications:

- piezoelectric thin films
- seed layers for the synthesis of arrays of vertically aligned ZnO NWs

It is important for both applications to investigate the morphology and the structure of the films. In fact, ideal piezoelectric thin films should be constituted of crystalline grains with the [002] crystalline direction perpendicular to the substrate: in this way, piezoelectric response to forces applied perpendicular to the substrate is maximized, due to the fact that the highest piezoelectric coefficient in ZnO is e_{33}, as was explained in section 1.1.2. The above-mentioned preferential orientation along the [002] crystalline direction is also required for their application as seed-layer, as it will be explained in section 3.4.

All the samples have been prepared by deposition with a Radio-Frequency (RF) magnetron sputtering on silicon substrates. Two different approaches were chosen:

- ceramic ZnO target, 40 $sccm\ Ar$ flux with 5 $mTorr$ pressure
- ceramic ZnO target, 39 $sccm\ Ar$ flux and 2 $sccm\ O_2$ flux with 5 $mTorr$ pressure

For both deposition approaches, three different sputter power values were tested: 30 W, 50 W, 100 W.

At first, the crystalline structure and orientation of the ZnO thin films were investigated by X-ray diffraction. Typical XRD spectra are shown in figure 3.1. All the XRD spectra show that the samples have hexagonal wurtzite crystalline structure: this is evidenced by the presence of the (002) wurtzite ZnO peak at $2\theta \approx 34.4°$ in each sample (the reference value is $2\theta = 34.37°$, reported by JCPDS-ICDD card n. 89-1397). The presence of the single (002) wurtzite ZnO peak suggests oriented growth of the films along the [002] crystalline direction. The morphology of the films was evaluated by means of FESEM, performed both in top-view and cross-section, for all the samples mentioned in table 3.1. Concerning FESEM sample preparation, cross-sections of the samples were produced by cleaving the samples with a diamond tip. All the samples exhibit

Table 3.1: Sputtered ZnO thin films

sample	power (W)	Ar (sccm)	O_2 (sccm)	T (℃)	time (min)
$SP702$	30	40	0	RT	60
$SP701$	50	40	0	RT	60
$SP695$	100	40	0	RT	60
$SP709$	30	39	2	RT	600
$SP708$	50	39	2	RT	240
$SP707$	100	39	2	RT	60
$SP728$	100	39	2	50	120
$SP738$	100	39	2	50	240

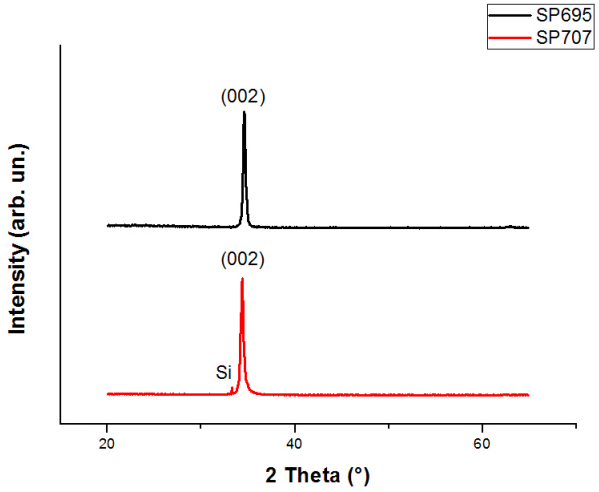

Figure 3.1: XRD spectra of samples SP707 and SP695; only the (002) wurtzite ZnO peak is visible, indicating preferentially oriented thin films

Table 3.2: Evaluation of thickness and average grain size

sample	thickness (nm)	grain size (nm)
$SP702$	75 ± 3	17 ± 5
$SP701$	210 ± 9	25 ± 10
$SP695$	800 ± 23 [fig. 3.4]	142 ± 42 [fig. 3.2b]
$SP709$	286 ± 3	23 ± 9
$SP708$	310 ± 6	26 ± 14
$SP707$	345 ± 4 [fig. 3.3]	26 ± 13 [fig. 3.2a]
$SP728$	750 ± 18	86 ± 23
$SP738$	1400 ± 30	180 ± 46 and 45 ± 11 [fig. 3.2c]

homogeneity and compactness (absence of cracks) along the whole surface. It is evident from top-view, 45°-tilt images and cross-section images that all the sample are constituted of columnar grains, whose average size is dependent on the deposition parameters and on the deposition time. The thickness and the average longitudinal grain size were evaluated from FESEM images and they are listed in table 3.2. It turns out that there is a correlation between the average grain size and the deposition time (or the thickness): the longer the deposition time, the larger the grain size. Two average values for the grain size are reported for sample $SP738$, since two different populations of grains are present, as shown in figure 3.2c. Moreover, the standard deviation of the thickness of the films gets higher as the the films get thicker, indicating higher root-mean-squared surface roughness as the deposition time is increased. The O_2 flux and the sputter power do not seem to play a significant role in the presented measurements. Samples with thickness $<$ 400 nm show well-defined columnar grains (figure 3.3); the diameter can be considered constant along the length of the grains and the morphology of the grains as seen in top-view is round-shaped (figure 3.2a). As the deposition time is increased and the samples get thicker, the grains become thicker at the expense of their morphology, which is less well-defined, as it can clearly be seen in figure 3.2b and figure 3.4. Further investigation of the crystalline structure of the films was conducted by Transmission Electron Microscopy on sample SP707, since this is the thickest sample with well-defined columnar structure (table 3.2). A thin lamella of the cross-section of the sample was prepared by following the procedure described in section 2.2.4. Since the ZnO film is only 300 nm in thickness, two protective Platinum layers were deposited in-situ: the first was deposited with the electron beam, while the second was obtained by FIB-induced deposition. A low-magnification TEM image of the lamella is shown in figure 3.5a. The analysis of selected-area diffraction patterns confirms the polycrystalline nature of the film; a typical example of diffraction pattern is presented in figure 3.5c. It must be stressed that the diffraction patterns are rotated 90° with respect to the images. The presence of a limited (002) arc in the diffraction patterns confirms that there is a preferential orientation of the grains along the [002] direction; moreover, it is possible to estimate the orientation spread by calculating the

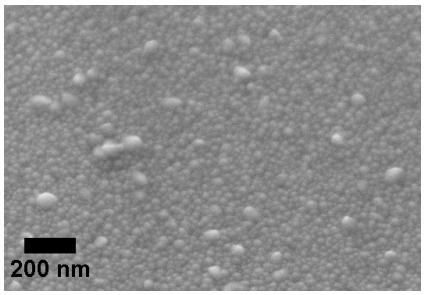

(a) 45° tilt top-view image of sample SP707; the grains are round-shaped

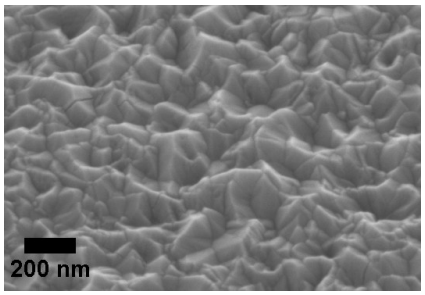

(b) 45° tilt top-viewimage of sample SP695; the shape of the grains is not well-defined

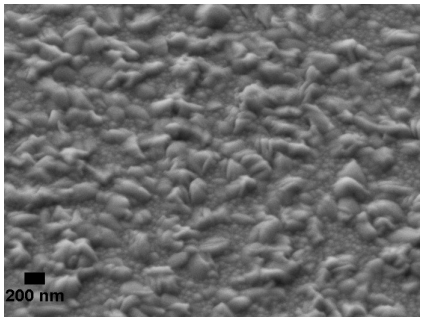

(c) 45° tilt top-view image of sample SP738; two different populations of grains are present

Figure 3.2: FESEM characterization of the morphology of the films

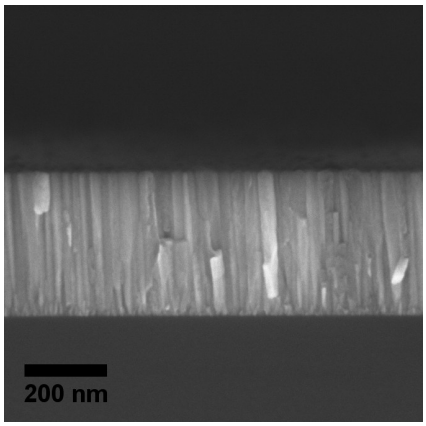

Figure 3.3: Cross-section image of sample SP707; thickness 345 ± 4 nm

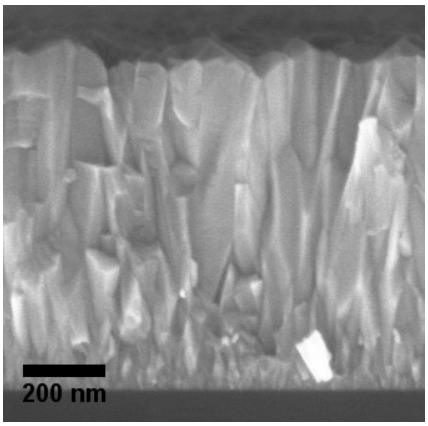

Figure 3.4: Cross-section image of sample SP695; thickness 800 ± 23 nm

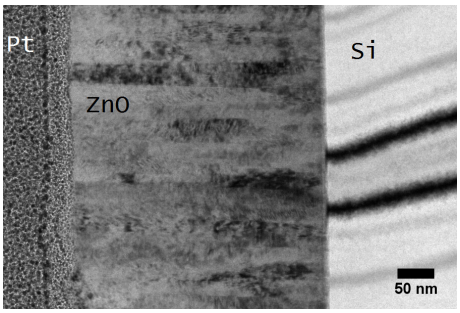

(a) Low-magnification image showing the lamella

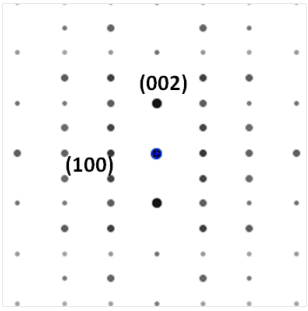

(b) Simulation of a selected-area diffraction pattern of a ZnO single crystal along the [010] zone axis

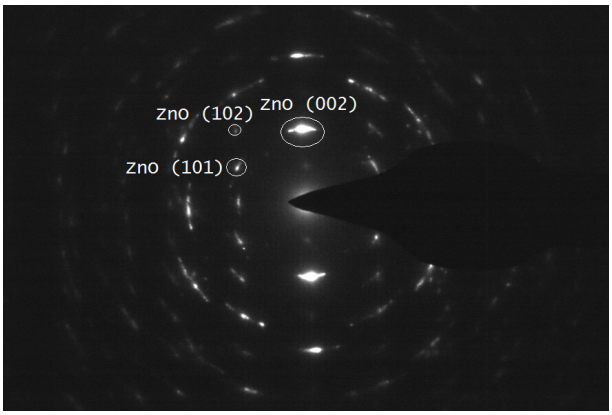

(c) SA diffraction pattern; the pattern is rotated 90° with respect to the images. The zone axis is [010]

Figure 3.5: Electron diffraction analysis of sample SP707

angle subtended by the circular (002) arc in the diffraction pattern. It can be seen that the majority of the crystals have orientation lying in a 20° range. The interplanar distance $d_{002} = 2.63 \pm 0.02 \AA$ was calculated from both selected area diffraction patterns and Fast-Fourier-Transforms (FFT) of high-resolution images. The reference value for d_{002} in ZnO crystals is $2.60 \AA$ (ICSD card n. 086254); the increase in d_{002} of at least $0.01 \AA$ in the analyzed sample is probably due to strain caused by lattice mis-match with respect to the substrate.
The analysis of the crystalline structure of single columns was possible through high-resolution imaging and subsequent FFT. Since the thickness of the lamella is higher than the average longitudinal grain size, most of the images exhibit Moiré fringes due to superimposition of slightly misoriented crystals. However, it was possible to follow the crystalline structure of two columns (figure 3.6) from the top to the bottom of the film. It can be reasonably asserted that the analyzed columns are single crystals. The crystalline structure of the film near

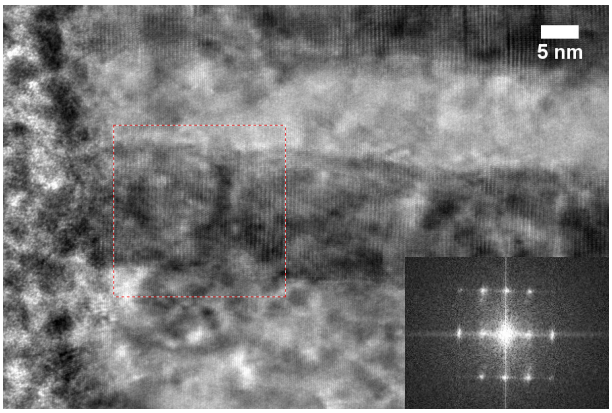

(a) HRTEM image of columnar grains. INSET: FFT of ROI

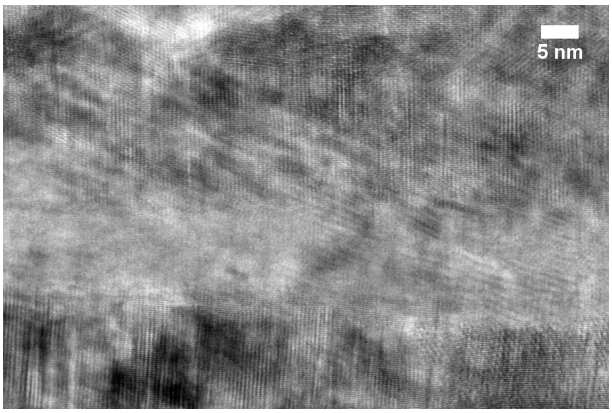

(b) HRTEM image of the columnar grains in the middle of the lamella

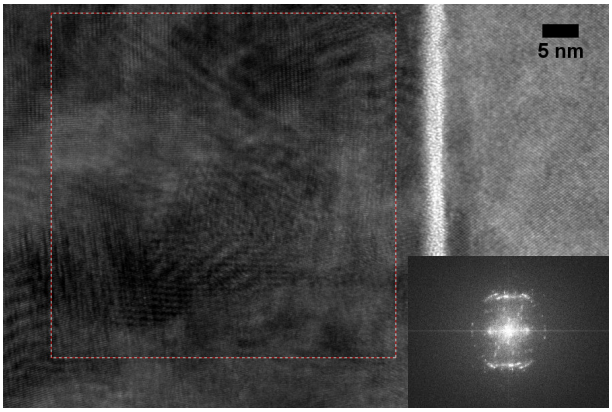

(c) HRTEM image of the columns near the interface with the substrate; inset: FFT of ROI

Figure 3.6: HRTEM analysis of SP707 lamella

the interface with silicon is less homogeneously oriented, as can be seen in figure 3.6c. This is coherent with the competitive growth model introduced by Van der Drift [55]: after the initial growth with random crystal orientation, crystals with the fastest growing crystalline plane parallel to the substrate survive at the cost of the others. In the case of ZnO, [002] is the fastest growing crystalline direction, due to the principle of minimization of surface energy [1].

3.2 Porous thin films

Porous thin films are produced at the CSHR as they are promising for applications which demand high surface areas; for example, porous ZnO films can be employed as:

- photoanode in Dye-Sensitized-Solar-Cells (DSSCs)
- photoanode material in Water-Splitting cells

Porous ZnO films have been obtained from the oxidation of porous Zn films. The Zn films have been deposited by RF magnetron sputtering at room temperature on Silicon substrates and glass substrates coated with FTO (Fluorine-doped Tin Oxide). A pure 99.99% Zn target is sputtered by Argon plasma at a sputter power of 30 W. The typical morphology of a porous Zn film is shown in figures 3.7a and 3.7b. The film is composed of nanostructured branches (typical cross-

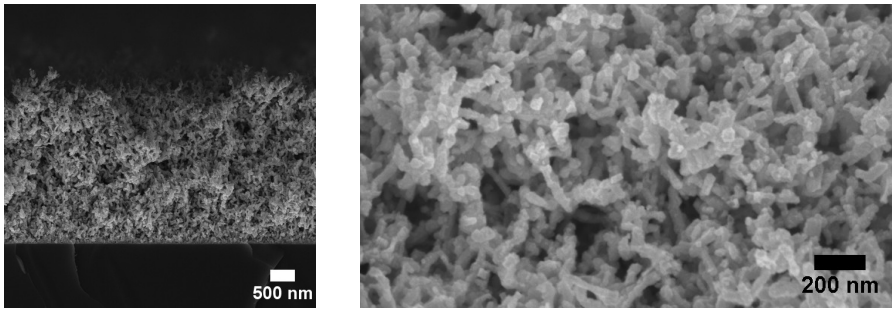

(a) Cross-section image of a porous metallic Zn film with thickness 3.3 μm

(b) High-magnification image of the porous nanostructured morphology of a metallic Zn film

Figure 3.7: FESEM images of porous metallic Zn

section size $\approx$ 30 nm) of randomly oriented crystalline grains, as can be seen from the XRD data in figure 3.8. As a result of the porosity of the films, the specific surface area of 14.1 m^2/g is quite high, as measured from N_2 sorption isotherms (BET) [56]. It is worth stressing that the morphology is not dependent on the choice between the two substrates (Si or FTO). FTO substrates are used as transparent conductive substrates for DSSC and water-splitting applications because they do not scatter visible light. Samples on Si substrates are usually

employed for SEM characterizations since they do not have charging issues. Currently, two different methods are employed for the oxidation of the metallic films:

- *thermal oxidation*: the porous metallic films are placed on a hot plate for 60 *min* at a temperature $T = 380$ ℃
- *water-vapor oxidation*: the metallic films are placed in a water vapor atmosphere for 60 *min* with no intentional heating; the water vapor is obtained by evaporation of De-Ionized water at $T = 90$ ℃

The water vapor oxidation has been developed as a low-temperature alternative to the thermal oxidation method: in principle, it opens the possibility of obtaining a porous ZnO film on flexible substrates, which in general could melt at the typical temperature ($T = 380$ ℃) of the thermal oxidation method. The analysis

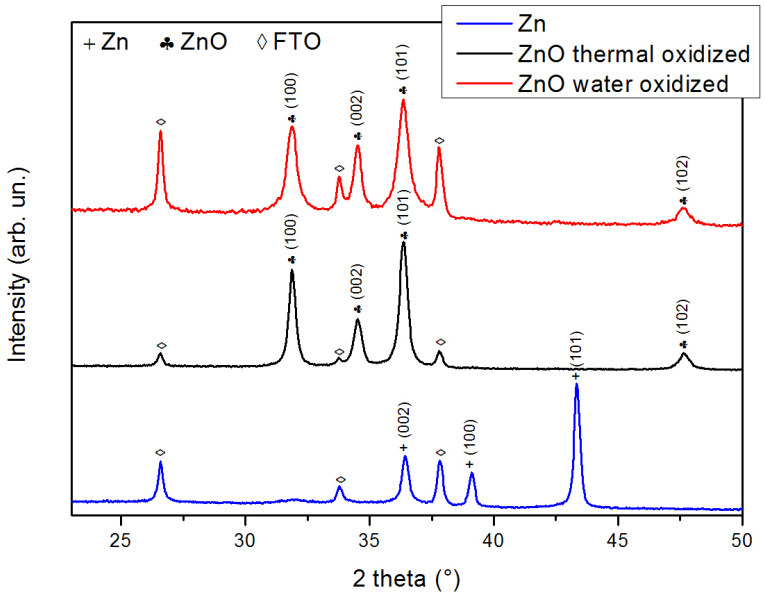

Figure 3.8: XRD spectra of porous Zn film, thermally oxidized and water-vapor oxidized ZnO films on FTO substrates

of crystalline structure of the ZnO films was conducted by XRD for both oxidation methods (figure 3.8). They are randomly oriented polycrystalline films; they exhibit the typical ZnO hexagonal wurtzite crystalline structure. The absence of the characteristic peaks of the Zn crystalline structure in the oxidized samples confirms the complete conversion of the original Zn metallic films into ZnO. Both oxidation methods lead to highly porous ZnO films, with slightly

different morphologies. The thermal oxidation method perfectly preserves the sponge-like morphology of the original Zn film, as it is clear by comparing figure 3.7b and figure 3.9a. On the other hand, the water vapor oxidized samples exhibit slightly larger branches near the top of the film, with further nanostructuration of the branch surface; however, the overall sponge-like structure is preserved through the oxidation treatment (figure 3.9b). The further nanostructuration could lead to higher surface-area, which in principle could be an improvement for applications.

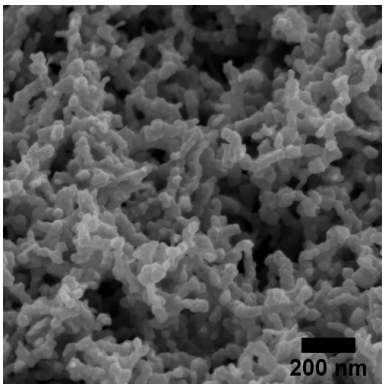

(a) High-magnification image ZnO film obtained by thermal oxidation

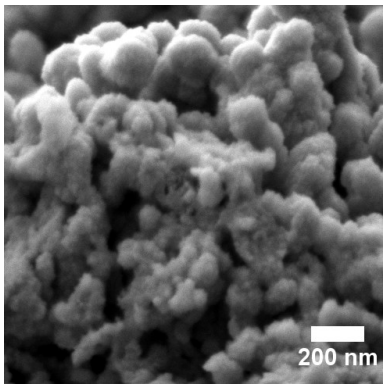

(b) High-magnification image of the ZnO film obtained by water-vapor oxidation

Figure 3.9: FESEM images of oxidized samples

Semi-quantitative analysis (figure 3.10) of EDX spectra acquired both in top-view and cross-section confirms the complete oxidation of the films: in fact, the Zn/O atomic concentration ratio is even lower than 1. However, from the EDX data, we cannot tell whether the excess of O is due to chemical bonding to carbonaceous contamination or it is symptomatic of a deviation from the ideal stoichiometry ($(Zn\ at\%)/(O\ at\%) = 1$) of the films. Considering EDX analysis, there are no major differences in chemical composition between samples obtained with either of the two oxidation methods.

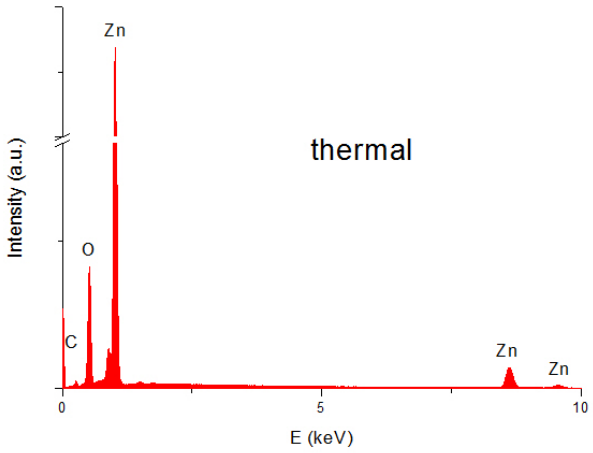

(a) EDX spectrum of a thermal oxidized sample

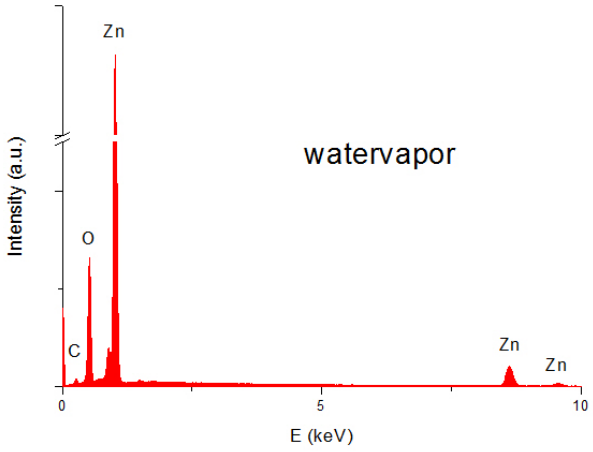

(b) EDX spectrum of a water-vapor oxidized sample

sample	$Zn\ at\%$	$O\ at\%$	$C\ at\%$
Thermal	38	51	11
Watervapor	37	52	11

(c) Semi-quantitative analysis

Figure 3.10: EDX analysis

3.3 Sol-gel Microwires

For the preparation of the ZnO microwires (MWs), zinc nitrate hexahydrate ($Zn(NO_3)_2 \cdot 6H_2O$) and potassium hydroxide KOH are dissolved separately in deionized water. The zinc nitrate solution is then merged with the KOH solution and, after stirring, a gel is obtained. The gel is subsequently placed in a Teflon vessel and kept at a temperature of 70 ℃ for a period of 5 h. The microwires are then separated from the solution by filtration, washed repetitively with deionized water and dried in air at a temperature of 60 ℃. It is worth mentioning that microwires can only be obtained when the concentration ratio $((KOH)/Zn(NO_3)_2) = 12$; otherwise, by tuning this ratio, different morphologies can be obtained such as flower-like microparticles and multipods [57]. After filtration and drying the microwires are agglomerated in the form of a white powder. The microwires have wurtzite crystalline structure, as high-

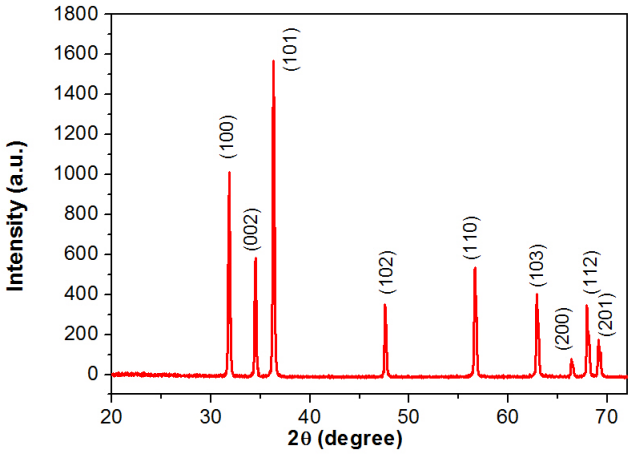

Figure 3.11: XRD spectrum of ZnO microwires; all the reflections belong to the ZnO wurtzite crystalline structure

lighted by the XRD analysis shown in figure 3.11. However, it is not possible to tell whether they are single crystals or not; moreover, we have no information about the growth direction. The typical morphology of the sol-gel microwires is shown in figure 3.12; SEM samples were prepared by simply placing a small quantity of MWs directly on a conductive tape, attached to a stub. The MWs all exhibit hexagonal cross-section, as a consequence of the wurtzite crystalline structure. The average diameter of the wires, measured as the distance between two opposite vertices of the hexagon, is $2.0 \pm 0.7\ \mu m$. We must stress that since the diameter of the wires is not constant along the length of the wire, the above-mentioned average value is purely qualitative. Accurate determination of the average length of the wires after the synthesis is difficult since most of them look

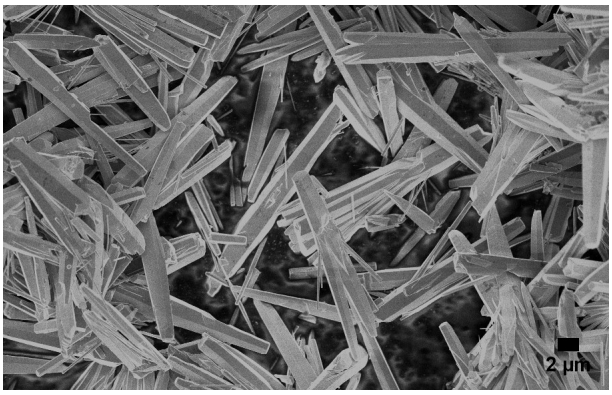

Figure 3.12: FESEM image of ZnO microwires

like they are broken; however, as a rough estimation, we can say that the length lies in the range $8-30\ \mu m$. For high-resolution FESEM imaging, a different approach to the sample preparation was adopted, in order to obtain isolated single microwires. A small amount of agglomerated wires was dispersed in ethanol; after sonication, small drops of the dispersion were deposited on Si substrates. After evaporation of the solvent, the samples were ready for the SEM analysis. Figure 3.13b shows a high resolution image of a single ZnO microwire. It can

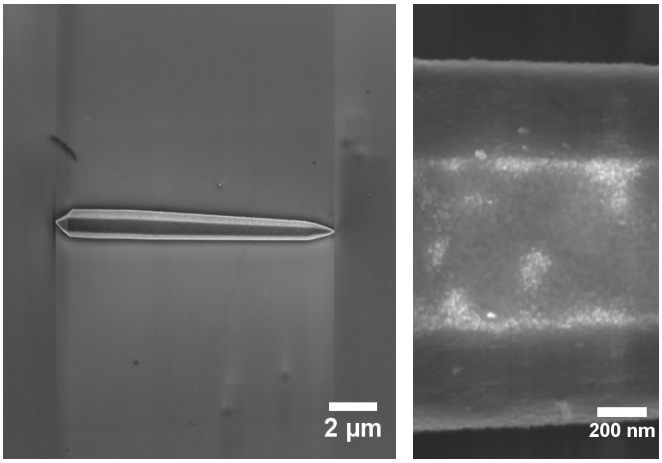

(a) Isolated microwire

(b) High-resolution image of the isolated MW

Figure 3.13: Surface morphology analysis

be seen in figure 3.12 that there exist a minority of the wires which have rather different diameter and length with respect to the others. Figure 3.14 presents a typical example of these anomalous wires, which will be referred to from now on

as *thin* microwires. It must be stressed that since XRD analysis provides infor-

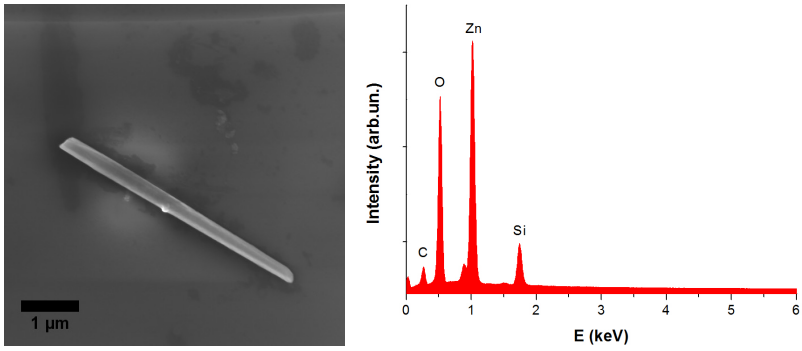

(a) Isolated thin microwire (b) EDX spectrum of the isolated thin MW

Figure 3.14: Surface morphology analysis

mation *on average*, it cannot in principle be asserted that these microwires have wurtzite crystalline structure. Moreover, due to their relatively large diameter ($> 200nm$), TEM analysis of their crystalline structure cannot be performed. However, due to their well-defined geometry with hexagonal cross-section, it can be safely asserted that they have wurtzite crystalline structure.

3.4 Hydrothermal Nanowires

Arrays of vertically-oriented ZnO nanowires can be employed for numerous applications, such as:

- nanostructured photoanode in DSSC or water-splitting cells, due to the high surface-to-volume ratio of the wires
- piezoelectric nanogenerators due to the their well-defined geometry coupled with piezoelectricity

The arrays are synthesized in a two-step procedure:

1. synthesis of the seed-layer
2. hydrothermal synthesis of the nanowire arrays

The main advantage of chemical growth on seed layers is that in principle NW arrays can be grown on any substrate. The seed layers are prepared in either of two ways:

- sputtering from a bulk ZnO target

- spin-coating or dip-coating by using a 10 mM solution of zinc acetate dihydrate ($Zn(CH_3COO)_2 \cdot 2H_2O$) in ethanol, followed by thermal treatments that promote the formation of a polycrystalline ZnO film. The ZnO nanocrystals act as seeds for the subsequent ZnO NWs growth

Once the substrates are uniformly coated by the seed layer, they are immersed in the aqueous growth solution, containing:

- zinc nitrate hexahydrate $Zn(NO_3)_2 \cdot 6H_2O$
- hexamethylenetetramine (HMT)
- polyethylenimine (PEI)
- ammonium hydroxide $NH_4(OH)$

The growth solution is kept at 88 ℃, which is a very low temperature when compared with other synthesis techniques such as CVD or MBE [5]. The growth time determines to a certain extent the final length of the wires; in the first 4 hours of reaction time, the growth rate of the wires is $\approx 1\mu m h^{-1}$ [58]. The reaction responsible for the formation of the wires is:

$$Zn^{2+} + 2OH^- \longrightarrow ZnO + H_2O \tag{3.1}$$

where HMT acts as the source of hydroxide. The addition of PEI and ammonium hydroxide to the solution is extremely helpful for the growth on seeded substrates: in fact, the presence of $NH_4(OH)$ and PEI prevents the formation of ZnO in the solution while keeping the growth rate of the wires on the seeded substrates reasonably high [59].

As it was previously stated, the hydrothermal (HT) synthesis allows for growth of vertically aligned arrays of nanowires on any substrate which is compatible with the deposition or the synthesis of the seed-layer. In fact, HT nanowires have been successfully synthesized at the CSHR on different substrates:

- Si, SOI or Si/Ti/Au: Si substrates coated with metals can be used for any application requiring an electrode
- FTO: transparent conductive substrates are used for optoelectronic applications where scattering of visible light must be minimized
- Kapton: in principle, nanowire arrays on flexible substrates (such as Kapton), could be employed for sensing applications as artificial skin

In general, synthesis of NWs on large areas is possible, as long as the seed layer homogeneously coats the substrate. The preparation of the seed layer plays a key-role in the whole synthesis process, since the properties of the seed layer directly influence the morphology and the density of the NW array. Seed layers obtained by both techniques are textured polycrystalline ZnO films with the [002] crystalline direction perpendicular to the substrate. In fact, the small

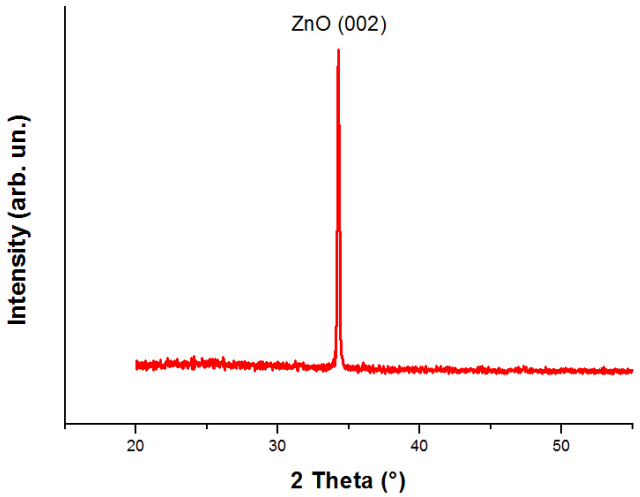

Figure 3.15: XRD of HT NWs on Si substrate

crystals of the seed layer act as nuclei for the nanowire growth and the crystalline orientation of the seeds directly translates to the orientation of the wire. Figure 3.15 presents a typical XRD spectrum; only the (002) wurtzite peak is present, confirming oriented growth of the wires along the [002] crystalline direction. The typical morphology of the wires is shown in figure 3.16. In general, the wires have hexagonal cross-section, although deviations from the ideal morphology are present in every sample. The average diameter is dependent on the seed layer solution concentration, the temperature of the thermal treatment of the seed layer and on the total reaction time. Optimized parameters are:

- $10mM$ zinc acetate solution for the synthesis of the seed layer
- 350° as seed layer calcination temperature
- total reaction time $< \ 4h$ for the synthesis of the wires

Cross-section FESEM studies of the samples confirm the good vertical alignment of the NWs, as it is shown in figure 3.17. It is clear from cross-section images that the diameter decreases along the length of the wires and some of them terminate with a tip shape at the top. Usually, the diameter of the wires lies in the range $(80 - 300 \ nm)$. Concerning the length of the wires, this is in general a monotonically increasing function of the reaction time and nanowires up to 4 μm long can be obtained. In order to obtain deeper insight on the NWs crystalline structures, TEM analysis was performed. The TEM sample preparation consisted of three steps:

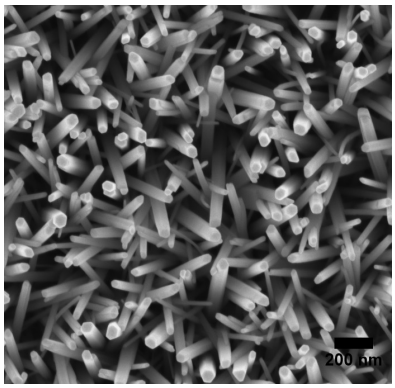

(a) Si substrate

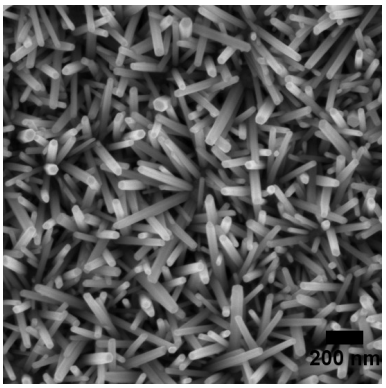

(b) FTO substrate

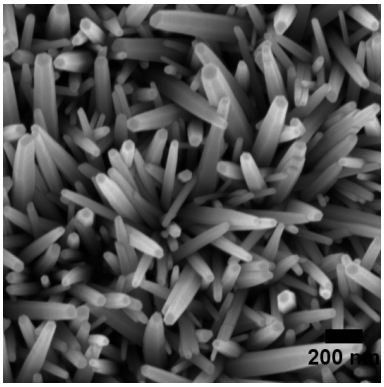

(c) Kapton substrate

Figure 3.16: Top-view FESEM images of HT NWs on different substrates

1. the nanowires are detached from the substrate by mechanical action with a razor blade
2. the detached nanowires are dispersed in ethanol (purity $>$ 99.8%) and placed in a ultrasonic bath for $5min$, in order ot reach a homogenoeous dispersion
3. a small drop of dispersion is placed on a conventional TEM holey carbon grid and after evaporation of the solvent the sample can be used for the analysis

High resolution images and related FFTs of several nanowires prove that the NWs are single crystals and that they grow along the [002] crystalline direction (figure 3.18b). Since some nanowires have large diameters ($> 150nm$) the single crystal nature of the nanowires cannot be confirmed by HRTEM. Selected area

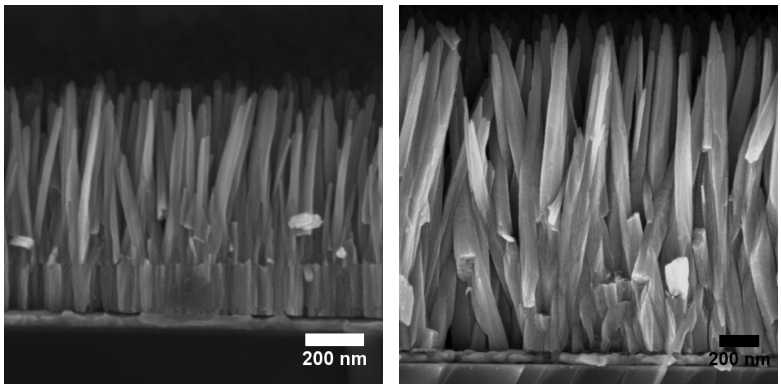

(a) Sputtered seed layer (b) Sol-gel seed layer

Figure 3.17: Cross-section FESEM images of HT NWs

electron diffraction patterns were acquired, confirming the single crystal nature of all the examined nanowires (an example is shown in figure 3.18c).

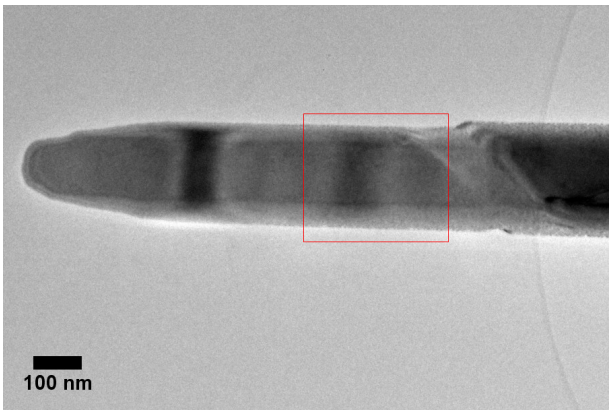

(a) Low-magnification image of a single NW

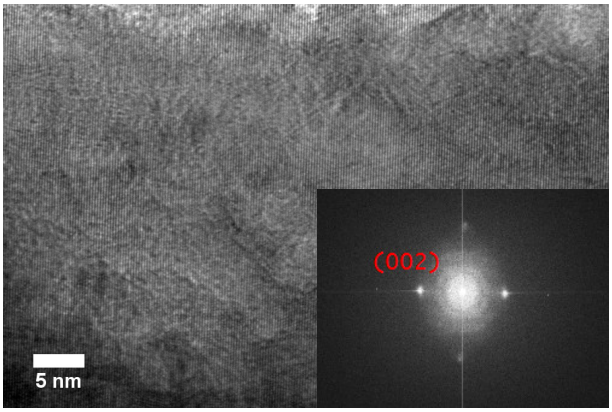

(b) HRTEM image showing lattice fringes; inset: FFT of the image

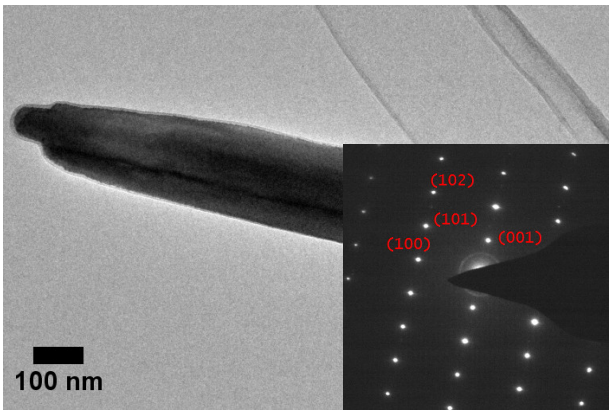

(c) TEM image showing HT nanowire; inset: SA electron diffraction pattern of the nanowire. The diffraction pattern is rotated 90° with respect to the image

Figure 3.18: TEM analysis of HT NWs

3.5 LPCVD Nanowires

In addition to the hydrothermal method, ZnO nanowires arrays have been prepared at the CSHR by Low-Pressure Chemical Vapor Deposition (LPCVD). Usually, less defective ZnO NWs can be obtained in the case of a chemical vapor deposition approach [60]; moreover, the high growth rate and the possibility of growing on large area substrates make this technique very interesting for the synthesis of ZnO NWs. In the CVD process vapor species from the source material are transported by a carrier gas inside the reaction chamber while a chemical reaction (in this case oxidation) takes place. As was the case with the hydrothermal synthesis, the presence of a seed layer is necessary for the growth of the nanowires. Seed layers for CVD growth are prepared with the same methods as the ones for the hydrothermal synthesis: by sputtering deposition or by spinning a solution of zinc acetate dihydrate ($Zn(CH_3COO)_2 \cdot 2H_2O$) in ethanol, followed by a thermal treatment. Silicon or metallized silicon are chosen as substrates, depending on the application. ZnO nanowires are grown in a tubular furnace working at low pressures ($\approx 1.3\ Torr$): sub-atmospheric pressures usually improve the uniformity of the structures across the substrate. An alumina tube placed horizontally is used for the growth of the nanostructures, at temperatures in the range $(650 - 700)$ ℃. The substrates are arranged on a flat alumina holder and placed in the central zone of the tube. A pure metallic Zn foil (99.95 % purity) is used as source of Zn. Ar is used as carrier gas, while O_2 is responsible for the oxidation of Zn during the growth on the substrate. Typical growth processes are carried out with $300 sccm\ Ar$ and $50 sccm\ O_2$ flow rates for 20 min.

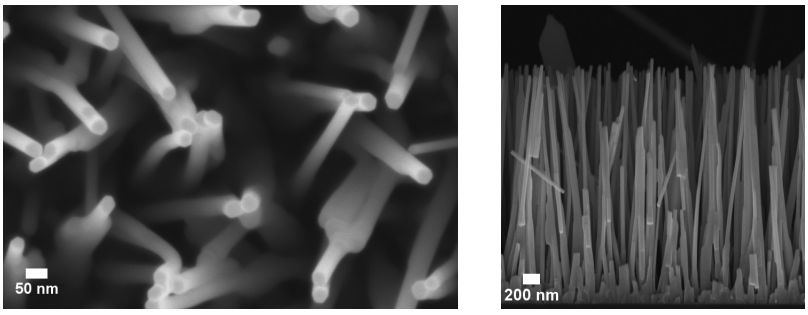

(a) Top-view image (b) Cross-section image

Figure 3.19: FESEM images of LPCVD NWs

Concerning the morphology of the wires, it is clear from FESEM images (figure 3.19) that the shape is much more well-defined with respect to the hydrothermally synthesized NWs. The wires have crystal facets typical of hexagonal crystals as a consequence of the wurtzite crystalline structure (see XRD spectrum in figure 3.20): they have hexagonal cross-section with approximately constant diameter. As for the hydrothermal NWs, the presence of (002) as the only peak in the XRD spectrum indicates a preferential orientation of the wires

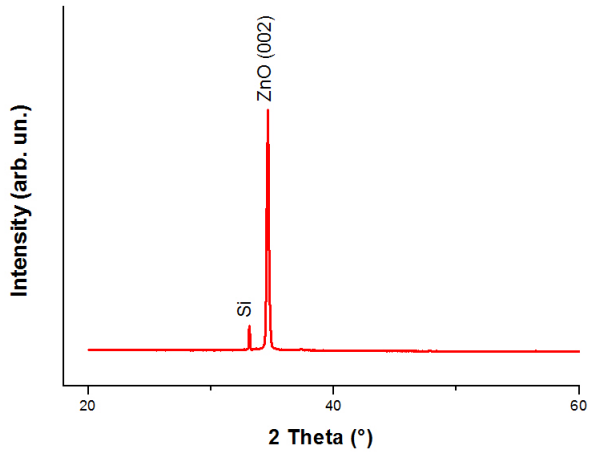

Figure 3.20: XRD spectrum of ZnO nanowires grown on Si substrate

along the [002] crystalline direction. This is confirmed by high-resolution TEM images and related FFTs, as shown in figure 3.21. The TEM sample preparation was carried out following the same procedure that was implemented for the hydrothermal nanowires.

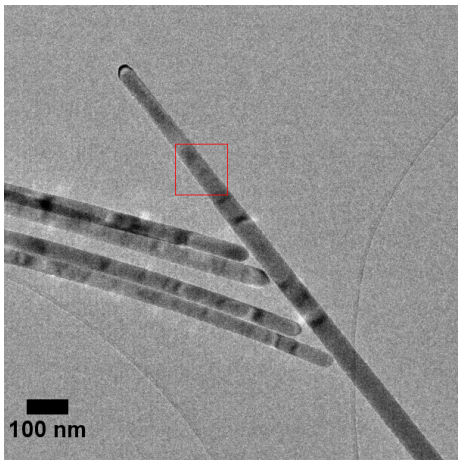

(a) Low-magnification image of single NW

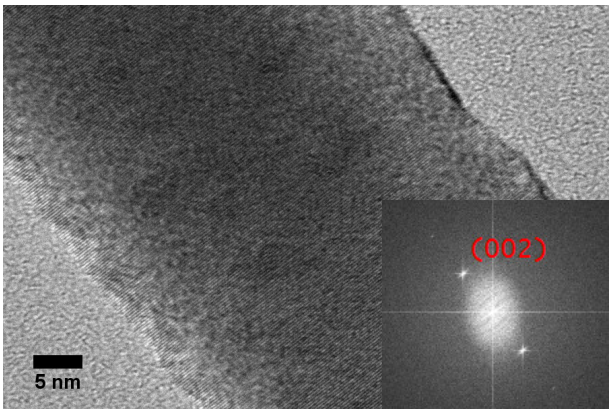

(b) HRTEM image; inset: FFT of the image

Figure 3.21: TEM analysis of LPCVD NWs

Chapter 4

In-situ electrical characterization

Among the different ZnO nanostructures, nanowires (NWs) are of particular interest for applications: they are envisioned as possible future building blocks for nanoelectronics [1] due to their well-defined geometry and possibly enhanced electronic transport properties, coupled with size-dependent piezoelectric response [61]. The electrical characterization of single nanostructures has recently attracted great interest for many reasons:

- nanostructures are the ideal experimental platform for the analysis of quantum-dictated effects on the electric transport properties of materials
- the higher surface-to-volume ratio with respect to bulk counterparts could lead to interesting physical and chemical phenomena due to the different interaction with the environment
- rapid scaling of device technology demands understanding of functional properties of materials at the nanoscale in view of their exploitation for applications

It is of great importance to understand how the electronic transport behavior of the NWs is influenced by morphology and crystalline structure on one side, and by the particular approach adopted for the implementation of electrical contacts at the micro/nano scale on the other side. To date, electrical measurements on single ZnO NWs have been reported in literature, with resistivity values ranging over many orders of magnitude ([62],[63]), depending on the synthesis techniques, morphology, crystalline structure and defects, type of electrical micro/nanocontacts, ambient conditions and experimental set-up. Despite this great effort, work still needs to be done in order to gain fundamental understanding of the electrical properties of single ZnO NWs and their

relationship with synthesis, crystalline structure and the technique adopted for the implementation of the contacts and the for the electrical characterization.

Different approaches have been adopted in literature for the preparation and characterization of the testing devices:

- *deposition on pre-patterned substrates*: electrodes are patterned on suitable insulating substrates (usually SiO_2) by conventional lithography. Nanowires are transferred onto the substrates by mechanical action or by dropping dispersions in suitable solvents, such as ethanol or isopropyl alcohol. The position of the wires on the patterned substrate can be controlled by micromanipulators or by dielectrophoresis ([64], [57]). Perfect control on the position of the wires is not possible and this is the major drawback of this preparation technique.

- *direct contact with micromanipulators*: the nanowires are transferred onto a non-conductive substrate and very sharp conductive tips are put in direct contact with the nanostructure inside the SEM chamber ([65], [66]). Voltage biasing is directly exerted on the nanostrcuture through the tips. The main disadvantage of this technique is that it is really hard to obtain good reliable electrical contacts with the nanowires. Moreover, another drawback is related to the size of tips, which makes direct contact with the smallest nanostructures impossible.

- *Electron-Beam Lithography*: EBL is the most common approach for the construction of devices in view of the electrical characterization of single nanostructures. The wires are transferred on a suitable substrate and the electrodes are patterned by EBL ([67], [68], [69]). The advantage of this technique is that the electrodes are deposited directly on the wires with sub-10 nm resolution [70]. The main drawback is that the preparation consists of many steps which need to be carefully optimized, such as: resist spin-coating, electron dose, deposition of the metal employed for the contacts, lift-off.

- *Atomic Force Microscopy*: AFM microscopes can be equipped with modules for the electrical characterization. The extremely sharp AFM tip can be coated with metals and put into direct contact with single nanostructures [71].

- *in-situ deposition of contacts in the SEM-FIB chamber*: nanowires are placed on a non-conductive substrate and the electrical contacts are directly deposited in the the FIB-SEM chamber by electron-beam induced deposition or ion-beam induced deposition ([72], [41]). Voltage biasing is exerted by putting micromanipulators in direct contact with the deposited conductive pads.

Considering the morphology of the wires synthesized in the Center for Space Human Robotics (CSHR) (presented in chapter 3 and summarized in table 4.1), we have decided to develop procedures for the electrical characterization based

Table 4.1: three different classes of wires are considered; the synthesis temperature, morphology and crystalline structure are reported

sample	T (℃)	Structure	length	diameter
SG MWs	70 ℃	wurtzite	$(8-30)\mu m$	$(0.9-2.7)\mu m$
HT NWs	88 ℃	wurtz., sin. crystal	$(1.3-2.5)\mu m$	$(80-300)nm$
LPCVD NWs	650 ℃	wurtz., sin. crystal	$(1.6-2.2)\mu m$	$(50-80)nm$

on the in-situ deposition of contacts. In fact, this technique is versatile and it can be applied to both micro and nanostructures; moreover, unlike EBL, it does not require the optimization of multiple steps. The dual-beam workstation AURIGA installed at the CSHR is equipped with a 5-channel Gas-Injector-System; currently, two different materials can be deposited:

- nominal platinum as conductive material
- nominal silicon dioxide as insulating material

Platinum was used as the material to be deposited for electrical contacts to nanowires. This choice is actually consistent with the literature: there are some reports ([73], [74]) of the in-situ deposition of Pt-contacts to ZnO nanowires which lead to linear I-V behavior with low contact resistances. Two micro-manipolators (Kleindiek Nanotechnik, equipped with tungsten tips) can be mounted in our Auriga dual-beam configuration; therefore, two-probe measurements are presented in this thesis work. The manipulators can be connected to any source measure unit (SMU) by BNC connectors. Figure 4.1 schematically represents the characterization system. Silicon wafers covered with SiO_2 obtained by thermal oxidation are chosen as insulating substrates. The wires are

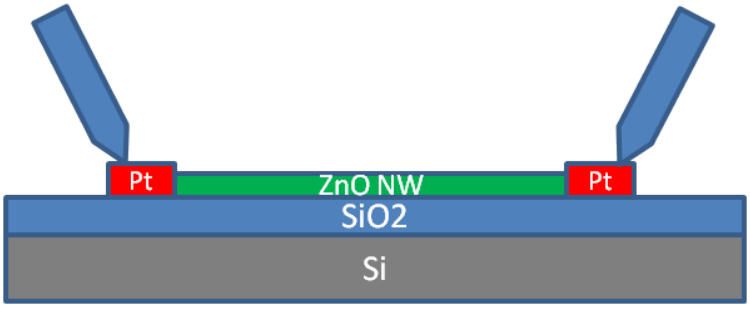

Figure 4.1: Two tungsten tips connected to a source measure unit are put in direct contact with the Pt nanopads

transferred to the substrates with the following procedure:

1. the nanowires (HT, LPCVD) are mechanically detached from the substrate with a razor blade. This step is not applied to the SG microwires since they are not synthesized on substrates

2. an extremely small quantity of microwires/detached nanowires is dispersed in ethanol (purity $>$ 99.8%) and placed in a ultrasonic bath for $5min$, in order to reach a homogenoeous dispersion

3. a small drop of dispersion, caught with a micropipette, is placed on the insulating substrates; after evaporation of the solvent, the samples can be put in the SEM chamber

Since the diameter and length of the wires synthesized with the three different methods span two orders of magnitude, specific procedures for the deposition of contacts must be developed for each kind of structure. Detailed description of the in-situ deposition process and of the necessary preliminary studies will be given in the following section. In the second part of this chapter, results on the electrical characterization of the ZnO micro and nanowires will be presented.

4.1 Preliminary studies on in-situ deposition

The electron (or ion) beam induced deposition consists of two simultaneous processes:

- a suitable gas precursor, injected in the FIB-SEM chamber by a Gas-Injection-System (GIS), is adsorbed on the surface of the sample

- the electron (ion) beam is scanned over the region of interest. The gas molecules are decomposed by the interaction with the beam; the volatile part is taken away by the pumping system while Pt is deposited on the surface of the sample, with the same shape and size of the scanned area

Many factors influence the deposition process: gas flux, energy of the beam, interaction volume of the beam with the substrate, scanning parameters [75]. The gas precursor for platinum deposition is methylcyclopentadienyl-trimethyl platinum $(CH_3)_3Pt(CpCH_3)$; the deposited material (shown in figure 4.2) is actually composed of an amorphous carbon matrix with crystalline Pt inclusions with average size $<$ 10 nm [76]. From now on we will refer to e-beam deposited and i-beam deposited platinum as E-Pt-C and I-Pt-C, respectively. The Pt concentration in I-Pt-C is usually $30 - 40$ $\%at$, while it is lower in E-Pt-C ; as a consequence, ion-beam deposited Pt shows better conductive behavior with respect to the electron beam deposited equivalent [76]. Moreover, during the deposition with ions, Ga ions are implanted in the deposited layer, enhancing conductivity. Since the decomposition of the gas precursors is more effective with the ion beam than the electron beam [77], materials can be deposited with ions at a much higher rate. The main drawback in performing ion-beam deposition is that the interaction of the beam with matter is destructive (see section 2.2). Another key aspect is that the deposition of the material with both beams is not perfectly limited to the scanned area: this *delocalization* of the deposition process is related to the fact that the interaction of electron or ion beams with matter extends over 3D volumes and secondary processes can

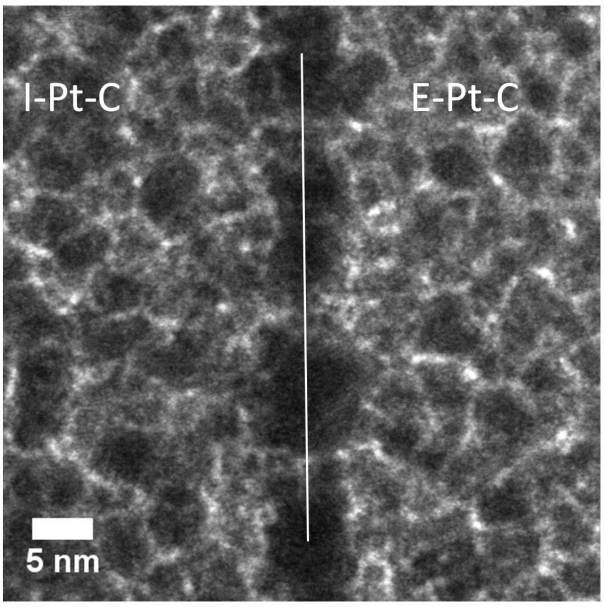

Figure 4.2: BF TEM image of i-beam (on the left) and e-beam (on the right) deposited Pt. The crystalline Pt inclusions (size $< 10nm$) show darker contrast with respect to the carbon matrix

occur micrometers away from the impinging spot of the beam. In fact, a halo of delocalized material is present around the in-situ deposited features (a schematic representation is shown in figure 4.3). The reasons for the halo formation are

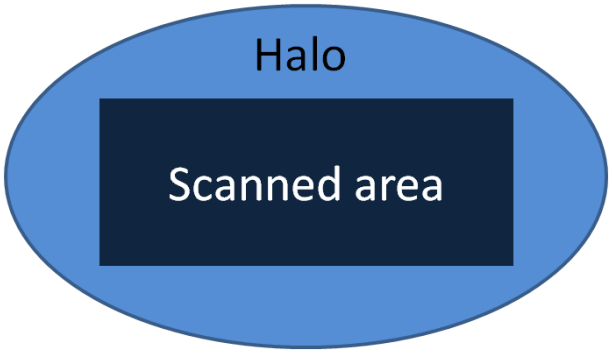

Figure 4.3: Halo effect in the in-situ deposition process

currently not clear; possible hypotheses include:

- **I-beam deposition**: ion beam profile with micrometer-sized extended tails, redeposition, forward scattering of Ga ions by already deposited material, diffusion over the substrate surface [46]

- **E-beam deposition**: secondary electrons produced by backscattered electrons could be responsible for delocalized dissociation of gas molecules

In general, the halo effect is more pronounced in i-beam induced deposition processes [78]. It is extremely important to minimize the delocalization of the deposition when dealing with nanowires with length $< 10\mu m$: in fact, the deposited halo is conductive and it can act as a resistor connected in parallel to the nanowire which is under test, affecting the measurements [79]. Figure 4.4 presents the electrical model of the characterization system, where R_{NW} is the resistance of the wire, R_C is the contact resistance at the $ZnO - Pt$ interfaces, R_{gap} is the resistance of the delocalized halo present in the gap between the contacts, $(R_{Pt} + R_{tip})$ comprises the resistance of the deposited Pt and the contact resistance between the tip and Pt. In order to obtain significant electrical

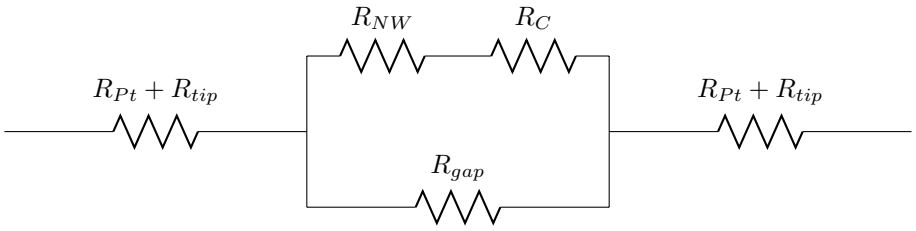

Figure 4.4: Electric model of the characterization system

measurements of the wire, R_{Pt} and R_{gap} must be minimized. Therefore, preliminary studies on I-Pt-C, E-Pt-C and on the delocalization of the deposition have been made in order to develop procedures for the deposition of the nanocontacts specific for the chosen nanostructures.

4.1.1 I-beam deposition

In order to evaluate the resistivity of I-Pt-C and the contact resistance between the tungsten tips and the deposited Pt layer, transmission line method (TLM) measurements were carried out on a Pt strip. The TLM [80] is based on conventional two-probe current-voltage sweeps performed at different channel lengths; the calculated values for the resistance at different channel lengths can be plotted against the length/cross-section ratio. In this case, we expect the system to behave as a series of resistors, where the measured total resistance is described by the equation

$$R = 2R_{tip} + R_{I-Pt-C} \tag{4.1}$$

with $2R_{tip}$ the total contact resistance and R_{I-Pt-C} the resistance of the strip at a given channel length. Since the resistance and the resistivity are related by

$$R_{I-Pt-C} = \rho_{I-Pt-C}\frac{l}{A} \tag{4.2}$$

the contact resistance and the resistivity can be extracted as the intercept and the slope of the linear fit of R vs l/A, respectively. The Pt strip ($20\mu m \times 2.2\mu m$,

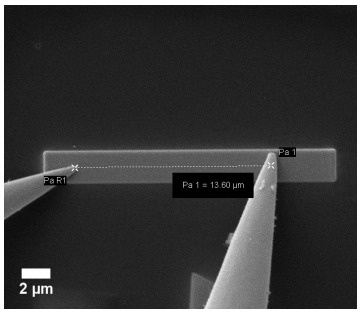

(a) Measure acquired with 13.6μm channel length

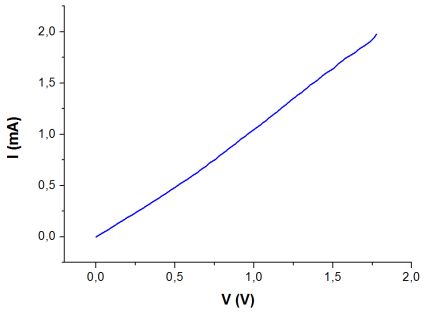

(b) I-V sweep acquired with 13.6μm channel length

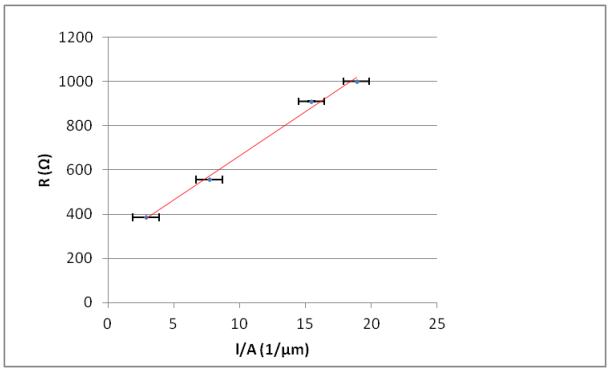

(c) Resistance vs l/A plot

Figure 4.5: Transmission Line Measurement of i-beam deposited Pt strip

thickness $\approx 400nm$) was deposited in this conditions: 30 kV acceleration voltage, 240 pA ion current, 2 min time, sample perpendicular to the ion beam optic axis (54° tilt). The ion current was chosen in order to reach the optimized deposition conditions of $5pA$ per μm^2. After deposition, the strip was characterized with I-V sweeps at different channel lengths; since the behavior was linear (see for example figure 4.5b), it was possible to calculate the resistance as the inverse of the slope of the I-V plot for any channel length. By plotting the as-calculated resistances as a function of the l/A ratio, it was possible to calculate the resistivity and the contact resistance: $\rho_{I-Pt-C} = 4200 \pm 300\ \mu\Omega cm$ and $2R_{tip} = 250 \pm 30\ \Omega$. The value for the resistivity of I-Pt-C is comparable with values reported in [76] for other strips deposited with the same gas precursor.

4.1.2 E-beam deposition

Studies on E-Pt-C strips have been made, following the same approach that was employed for I-Pt-C strip. However, there are some differences between the two deposition processes. One parameter that influences the deposition rate and the structure of the Pt layers is the electron or ion beam current. The ion current can be controlled over several orders of magnitude ($20pA\ -\ 16nA$) by selecting the appropriate aperture. The electron current can be controlled by apertures, too; however, the significant range of available currents is narrower than in FIBs ($600pA - 3nA$). As a consequence, one cannot perform deposition on large areas while keeping the current per unit area constant. Moreover, the electron beam energy is a critical factor in e-beam deposition: the deposition rate is maximized when the beam energy is 1.5 keV and it lowers by a factor of 2 when the energy is over 3 keV. Unfortunately, at low beam energies the electron beam is deflected by charging effects caused by the insulating substrate. We have experimentally found out that with our substrates ($\approx 1\mu m$ thick SiO_2) the threshold value of energy for the electron beam to be stable is 4 keV. The best condition for stationary conditions of the electron beam near the surface of the sample is 5 keV beam energy. Therefore, a E-Pt-C strip was deposited at 5 keV beam energy with the highest beam current possible ($\approx 7nA$), which on the Auriga dual-beam microscope is obtained by selecting the $120\mu m$ aperture in the *high current* mode. A E-Pt-C strip (shown in figure 4.6a) was deposited with longitudinal dimensions $14\mu m \times 1.5\mu m$; the thickness of the strip was $\approx 380nm$. After the deposition, the strip was characterized with I-V sweeps at different channel lengths, in accordance with the TLM. As was previously done with I-Pt-C strip, it was possible to calculate the resistivity $\rho_{E-Pt-C} = (4.2 \pm 0.4) \cdot 10^5\ \mu\Omega cm$, which is significantly higher than ρ_{I-Pt-C}. The obtained result is comparable with the ones found in literature [81] and it can be explained by the difference in chemical composition between ion-deposited and electron-deposited Pt: the Pt content is reduced in E-Pt-C layers and therefore conductivity is lower, too. The obtained value for $2R_{tip} = 4000\Omega$ (tip-contact resistance) is not statistically significant since the uncertainty evaluated from the linear fit was larger than $2R_{tip}$. Further insight into the contact resistance between tips and E-Pt-C will be given in chapter 5.

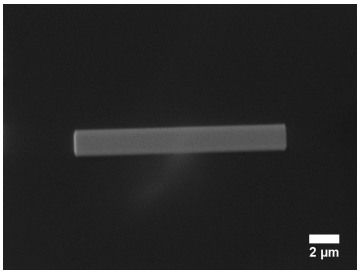

(a) E-beam deposited Pt strip

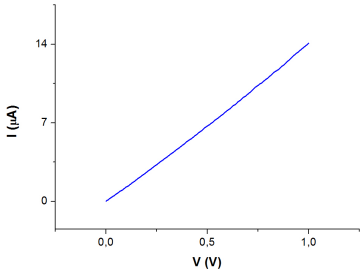

(b) I-V sweep acquired with $9.7\mu m$ channel length

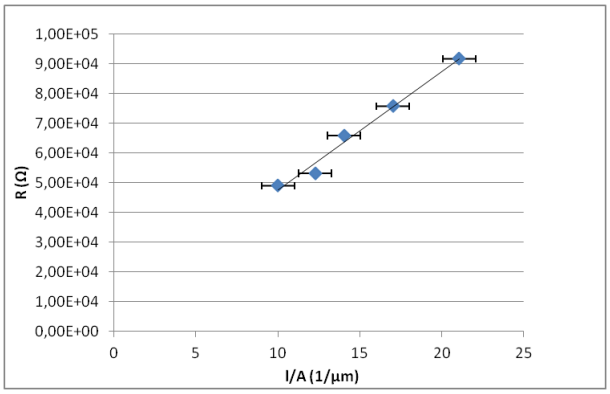

(c) Resistance vs l/A plot

Figure 4.6: Transmission Line Measurement of e-beam deposited Pt strip

4.1.3 Halo study

In order to estimate the gap resistance between pads in different conditions, experiments were conducted on both I-Pt-C and E-Pt-C. The gap length must of course be comparable with the average length of the wires under testing. As can be seen in table 4.1, there are basically two different lengths of interest:

- Sol-Gel microwires: length $> 9\ \mu m$
- Hydrothermal and LPCVD nanowires: length $\approx 2\mu m$

Deposition with the electron beam (e-beam) would be the ideal choice since the interaction of the electrons with matter is not destructive. However, the growth rate with electrons is much lower than with the ions; this could be a problem with the sol-gel microwires, having diameters $> 1\ \mu m$. Moreover, I-Pt-C shows better conductive behavior, as underlined by the previous TLM studies on Pt strips. Therefore, two different approaches were chosen for the study on the delocalization problem, as a consequence of the existence of two different classes of sample:

- deposition of I-Pt-C contacts with a $13\mu m$ gap
- deposition of E-Pt-C contacts with a $2\mu m$ gap

I-Pt-C gap

Two conductive pads of longitudinal dimensions $4\mu m \times 3\mu m$ were deposited at a $13\mu m$ gap length. The area of the pads ($\approx 12\mu m^2$) is optimized for their use as contacts for the SG MWs, as it will be clear in section 4.2.2. The micro pads were grown for $120s$ using $30keV\ Ga$ ions at a $50pA$ ion current ($\approx 5\ pA/\mu m^2$). The current between the gaps was characterized by I-V sweeps, such as the one

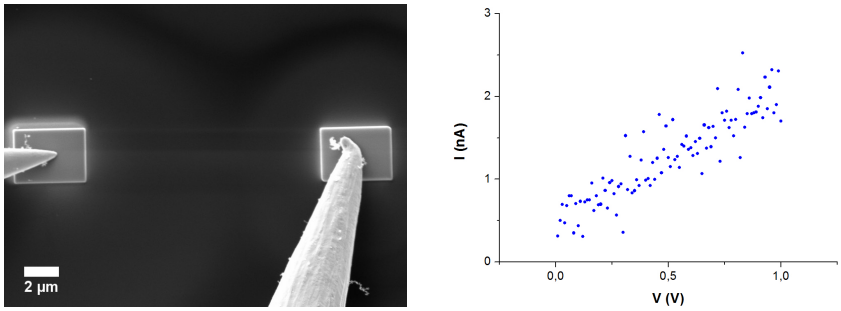

(a) (b)

Figure 4.7: Evaluation of leakage current for I-Pt-C

shown in figure 4.7b. It is possible to calculate the gap resistance by linear fitting of the I-V curves. In this way, the resistance of the gap R_{gap} is estimated to be $6 \cdot 10^8\ \Omega$. Therefore, by recalling the electrical model in figure 4.4, the

leakage current due to the deposition halo should not affect the measurements as long as $R_{NW} + R_C$ is at least one order of magnitude lower than R_{gap}, since:

$$R_{total} = \frac{(R_{NW} + R_C) \cdot R_{gap}}{(R_{NW} + R_C) + R_{gap}} \approx \frac{(R_{NW} + R_C) \cdot R_{gap}}{R_{gap}} = R_{NW} + R_C \quad (4.3)$$

It will be shown in section 4.2.2 that this is the case when characterizing the SG microwires.

E-Pt-C gap

As previously discussed, E-beam induced deposition is the only choice when dealing with the nanowires with sub-100 nm diameter: in fact, even mild exposure to the ion beam could lead to amorphization or Ga implantation in the wires, possibly affecting their electrical behavior. Moreover, it is known from the literature that e-beam deposition is usually less delocalized [78]: minimization of delocalization is extremely important with nanowires with length $\approx 2\mu m$. Many deposition parameters were varied during the analysis:

- electron current: the electron current was varied by changing the aperture and the mode (normal mode or high-current mode)
- deposition time: deposition time is related to final thickness of the pads
- sample tilt: the gas flux is confined in a smaller region when the GIS approaches a position normal to the surface of the sample (see figure 4.8). In the Auriga dual-beam microscope, the position of the GIS is optimized for FIB deposition, therefore it is placed at 54° of tilt with respect of the surface of the sample
- beam energy: lower beam energies could lower the probability of having delocalized scattering events, since the interaction volume is smaller. However, the energy cannot be lowered below $4keV$ if one wants to retain stationary conditions of the beam near the surface of the insulating SiO_2 substrate.

Two typical experimental set-ups for the characterization of the leakage current are shown in figures 4.9a and4.9c. Table 4.2 reports the deposition conditions and the estimated gap resistance for seven samples. The first four samples consist of a pair of $3\mu m \times 2\mu m$ pads deposited $1.5\mu m$ far from each other. Samples from 5 to 7 have a different design (figure 4.9c); the pads are composed of two parts with different functions:

- $1\mu m \times 500\ nm$ contact area to the nanowire
- $2\mu m \times 1\mu m$ landing area for the micromanipulators

Furthermore, sample 6 was deposited on a different substrate with lower SiO_2 thickness, in order to investigate the halo effect at lower beam energies; in

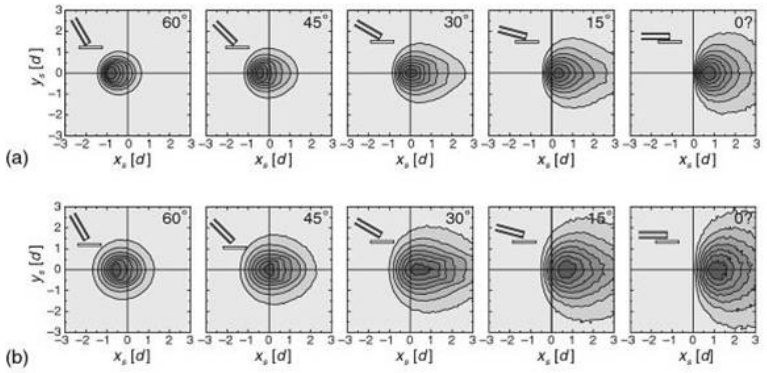

Figure 4.8: Gas flux lines obtained with the GIS simulator at two different distances of the GIS from the surface of the sample [46]

Table 4.2: Leakage current estimation

sample	EHT	aperture	tilt	time	R (Ω)
1	4 kV	120 HC	0°	1 min	$(1.028 \pm 0.002) \cdot 10^5$
2	5 kV	60 HC	0°	1 min	$(1.98 \pm 0.05) \cdot 10^6$
3	4 kV	60 HC	0°	1 min	$(2.70 \pm 0.04) \cdot 10^6$
4	5 kV	60	0°	1 min	$(6.550 \pm 0.004) \cdot 10^5$
5	5 kV	60	54°	20 s	$(2.327 \pm 0.007) \cdot 10^6$
6	2 kV	60	30°	20 s	$(1.332 \pm 0.003) \cdot 10^6$
7	5 kV	60	30°	20 s	$(2.35 \pm 0.02) \cdot 10^6$

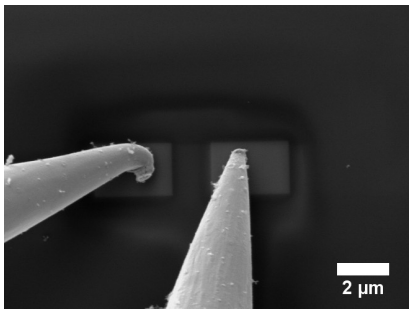

(a) Sample 4

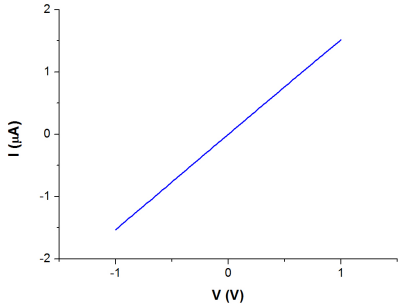

(b) I-V sweep of sample 4

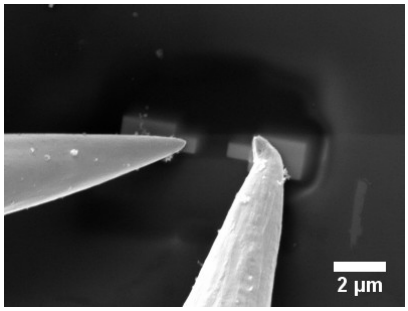

(c) Sample 5

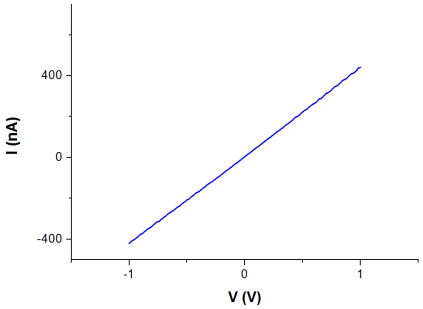

(d) I-V sweep of sample 5

Figure 4.9: Evaluation of leakage current for E-Pt-C

Table 4.3: Summary of results on preliminary studies

I-strip	E-strip	I-gap	E-gap
$\rho \approx 4 \cdot 10^3 \mu\Omega cm$	$\rho \approx 4 \cdot 10^5 \mu\Omega cm$	$R \approx 6 \cdot 10^8 \Omega$	$R \approx 2 \cdot 10^6 \Omega$

fact, by lowering the thickness of the oxide, it was possible to have stationary conditions of the $2keV$ beam near the surface. Based on the results shown in table 4.2, there is an indication that by lowering the electron current (smaller aperture), the gap resistance is higher. Concerning the other parameters, there is no clear indication of their effect on the gap resistance. The outcome of the deposition process is highly influenced by the gas flux, which is in part determined by the pressure gradient between the gas reservoir and the SEM chamber. The pressure in the gas reservoir in equilibrium is a function of the temperature through Clausius-Clapeyron equation; however, when the gas valve is open there are not equilibrium conditions and the gas flux is not completely under control. Moreover, the position of the sample relative to the GIS is not perfectly controlled or repeatable. Therefore, it can be assumed that the most important limiting factor is the lack of perfect control on the GIS flux. As a consequence, for the characterization of nanowires the experimental conditions which lead to more reproducible results (sample $5, 6, 7$) are chosen, namely: 5 keV electron beam, $60\mu m$ aperture, 30° tilt of the sample with respect to the optical axis.

4.2 I-V electrical characterization

The results from the preliminary studies, are summarized in table 4.3. These preliminary studies are the basis for the specific approach to the deposition of contacts for the different micro and nanowires. In this section, we will present the results on the electrical characterization of single ZnO microwires and nanowires, based on the acquisition of two-probe I-V curves.

4.2.1 Introduction on contacts

In figure 4.4 the equivalent electrical model for the in-situ two-probe characterization system was presented. In this model, the total contribution from the interface between the ZnO wire and the deposited Pt contacts is modeled as series resistance R_C. However, this assertion is strictly true only in case the conductive behavior of the contact regions is linear. On a more general basis, the interface between ZnO (a semiconductor) and the Pt contact regions (which behave like a low-conductance metal) should be treated as a metal-semiconductor interface. Usually, a potential barrier arises when a semiconductor and a metal are brought into physical contact; as a consequence, this kind of contacts typically show a rectifying behavior, as it is shown in figure 4.10. In fact, metal-semiconductor systems can be used as rectifying devices, called Schottky diodes, since Schottky firstly developed the theory of metal-semiconductor contacts [82]. The I-V

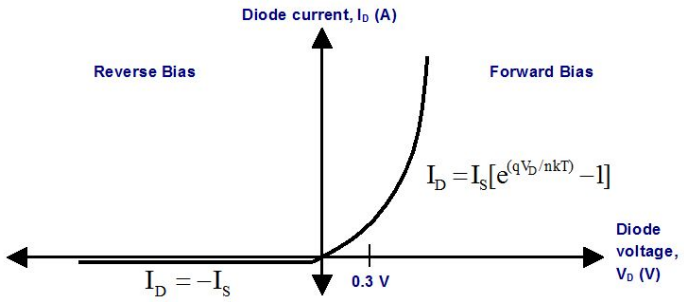

Figure 4.10: I-V characteristic of a Schottky diode

characteristic of the metal-semiconductor interface can be described by:

$$\text{reverse bias} \quad I \approx I_s$$

$$\text{forward bias} \quad I = I_s \left[e^{qV_{MS}/\eta k_B T} - 1 \right]$$

with η ideality factor, q electron charge, k_B Boltzmann constant, T absolute temperature, I_s saturation current, V_{MS} the voltage drop at the interface. Within the frame of thermionic emission theory, the saturation current is [83]:

$$I_s = A^* A T^2 e^{-q\Phi_b/k_B T}$$

with Φ_b the barrier height, A^* Richardson constant and A the contact effective area. In the case of n-ype semiconductor, the barrier height can be expressed in the Schottky-Mott approximation as:

$$\Phi_b = \phi_M - \chi_S$$

with ϕ_M the metal workfunction and χ_S the electron affinity of the semiconductor. However, this expression does not take into account surface states: in fact, real contacts are not in complete accordance with the Schottky expression for the barrier. Moreover, the barrier Φ_b usually depends on the applied bias as a consequence of the presence of unavoidable interfacial layers or the effect of the image force [83]. In this case, the reverse bias characteristic of the Schottky interface does not show saturation.

The system composed by the ZnO nanowire and the e-beam deposited contacts can be represented with the equivalent circuit shown in figure 4.11, with $C1$ and $C2$ back-to-back Schottky diodes associated to the interfaces between ZnO and e-beam deposited Pt. The applied bias V (neglecting contribution from the tips and the Pt contacts), is distributed as

$$V = V_{C1} + V_{NW} + V_{C2}$$

During DC measurements, one Schottky diode is in the forward bias condition, while the other is in the reverse bias condition. Zhang et al. [84] have proposed

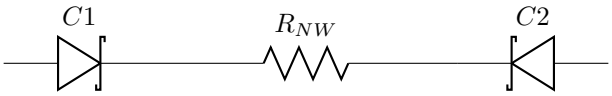

Figure 4.11: Equivalent circuit

a model for the I-V characteristic of back-to-back with Schottky diodes in series with a semiconducting nanowire: in this model, different types of I-V curves can be obtained, by varying the Schottky barrier heights and the ideality factors associated to each metal-semiconductor interface. In general, the obtained I-V curves show two linear regimes: one at low bias, the other at large bias (the concepts of low and large bias are dependent on the particular device under test). In the linear regime, the contribution to the voltage drop of the back-to-back Schottky diodes in the electrical circuit presented in figure 4.11 can be effectively reduced to purely resistive; in this, way the electrical model shown in figure 4.4 is retrieved. According to the model presented in [84], the large bias linear regime should in principle allow for the calculation of the resistance of the nanowire, since at large bias the resistance of the Schottky contacts should be negligible when compared to the resistance of the nanowire. However, this approach was not possible in the measurements presented in this thesis work due to failure of the devices at large bias, probably due to Joule heating. Therefore, the values for the resistance reported in this work are calculated from the low-bias linear regime and contact resistances are not in principle considered negligible, as it will be shown in the following sections.

4.2.2 Sol-Gel Microwires

The preparation of the micro pads consists of two steps:

1. **deposition of a protective E-Pt-C layer**: the aim of this preliminary step is to provide deposition of conductive material without the interference of possible destructive interaction of Ga ions with the microwire under test; however, since the growth rate is low and the microwires are thick (diameter $>$ $1\mu m$), a second step with the ion-beam is necessary. The E-Pt-C layers are deposited with 5 keV electrons with the $60\mu m$ aperture in the high-current mode for 2 minutes

2. **deposition of I-Pt-C contacts**: the deposition of the actual micro pads is performed with the ion beam with 30 keV ions and $50pA$ current for 2 minutes

After the deposition of the micropads, tungsten tips are put into direct contact with them and voltage bias is applied on the nanostructure. The two-probe I-V characteristic of sample SG1 is shown in figure 4.13b. It can be seen from I-V curve that the electric behavior of the wire is linear in the range $(0 \div 1)$ V; the resistance of the system can be calculated as the inverse of the slope of the I-V curve. The curve is noisy probably due to imperfect deposition of contacts

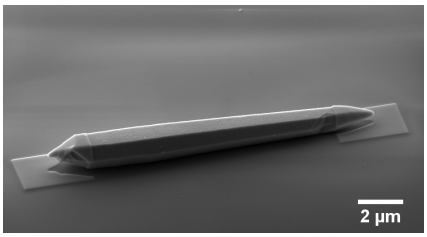

(a) First step: deposition of protective layer with the e-beam

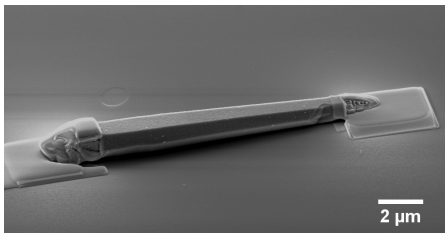

(b) Second step: deposition of the micro pads with the i-beam

Figure 4.12: Two-step preparation of the conductive micro pads for the SG MWs

at the nanowire-contact interface. The imperfect deposition of contacts can be attributed to shadow effects caused by the relatively large size of the considered microwires. Moreover, the position of the tips on the pads could play a role: in fact we have noticed that good contacts are not immediately established when the tips touch the sample. The position of the tips is optimized by imposing constant DC voltage bias and maximizing the intensity of the current. Once the best tip-pad contact is obtained, I-V curves are acquired. The electrical behavior of sample SG2 in the $(-2 \div 2)$ V voltage range and for SG3 in the range $(-3 \div 3)$V is shown in figures 4.13d and 4.13f. Sample SG2 and SG3 show slightly non-linear behavior: according to the model presented in section 4.2.1, the deviation from the linear regime is caused by the Schottky barriers at the ZnO-Pt interface. In this case, according to the model by Zhang [84] the value for the resistance is calculated in the large-bias linear regime. Globally, four microwire samples were analyzed. The results for all the samples are reported in table 4.4. The presented values for resistance are calculated as the average of

Table 4.4: I-V characterization of Sol-Gel microwires

sample	l (μm)	d (μm)	R (Ω)	ρ ($\mu \Omega cm$)
SG1	9.0 ± 0.2	1.8 ± 0.2	$(1.5 \pm 0.1) \cdot 10^4$	$(3.5 \pm 0.8) \cdot 10^5$
SG2	14.0 ± 0.2	2.0 ± 0.2	$(3.1 \pm 0.1) \cdot 10^4$	$(5.8 \pm 1.2) \cdot 10^5$
SG3	19.5 ± 0.2	2.1 ± 0.2	$(2.0 \pm 0.2) \cdot 10^4$	$(3.0 \pm 1.0) \cdot 10^5$
SG4	11.5 ± 0.2	1.6 ± 0.2	$(2.1 \pm 0.1) \cdot 10^4$	$(3.0 \pm 0.7) \cdot 10^5$

several repeated measurements for each sample. The uncertainty of resistance was calculated as $(max\ value - min\ value)/2$. Since the diameter of the wires is not homogeneous along the length of the wires, it is difficult to accurately calculate the resistivity; as an estimation, values for the resistivity are reported in table 4.4, where the uncertainty is obtained by standard propagation of error. The measured values for resistance can be interpreted by looking at the electrical model in figure 4.4. It is clear from the experiments presented in section 4.1.1 that the contribution $R_{Pt} + R_{tip}$ is negligible, since it is $< 10^3 \Omega$. Therefore, the electrical model reduces to:

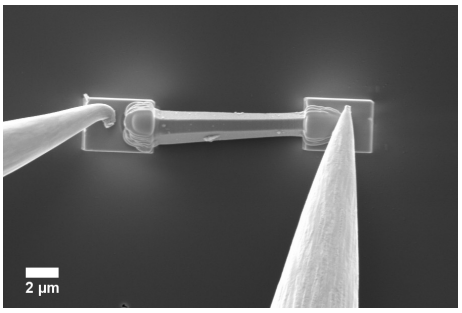

(a) FESEM image of sample SG1 during measurements

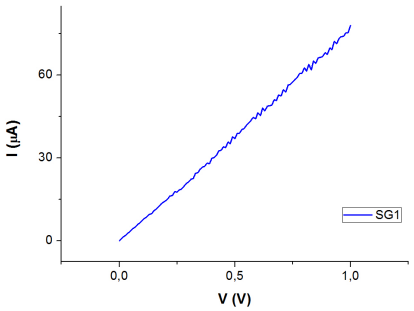

(b) I-V sweep of sample SG1 in the $(0 \div 1)$ V range

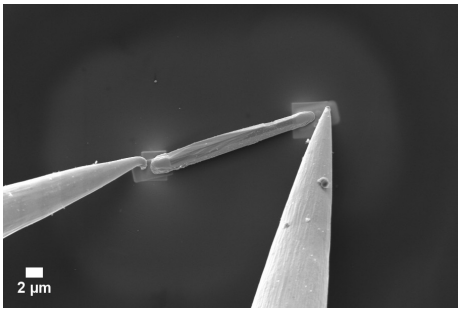

(c) FESEM image of sample SG2 during measurements

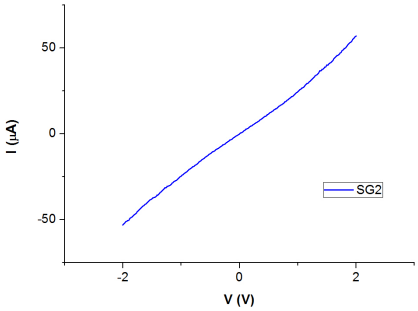

(d) I-V sweep of sample SG2 in the $(-2 \div 2)$ V range

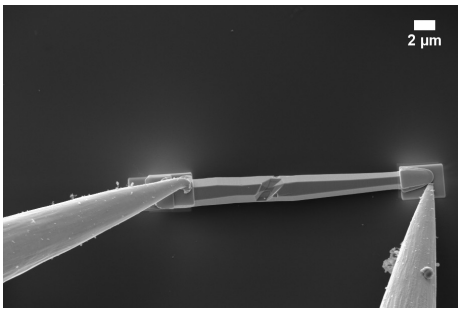

(e) FESEM image of sample SG3 during measurements

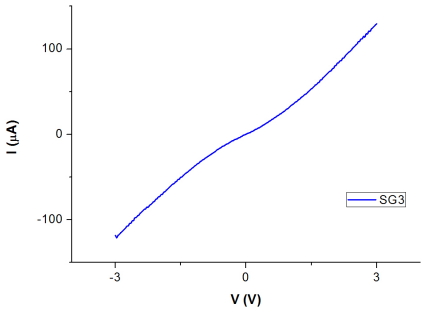

(f) I-V sweep of sample SG3 in the $(-3 \div 3)$ V range

Figure 4.13: Electrical characterization of SG MWs

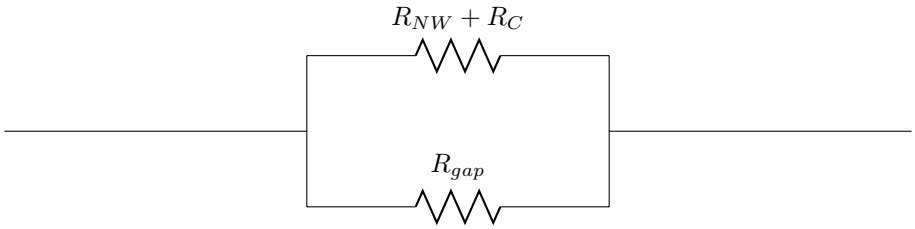

Moreover, we have demonstrated in section 4.1.3 that the contribution of the halo is negligible, since $R_{gap} \approx 10^8\Omega$, which is two orders of magnitude greater than the measured resistance. Therefore, we can conclude that

$$R_{meas} \approx R_{NW} + R_C \tag{4.4}$$

where R_C is the contact resistance between the deposited Pt and the ZnO microwire. Unfortunately, two-probe DC measurements cannot supply information about the contact resistance; therefore, the presented resistivity values are representative of the microwires only in case $R_C << R_{NW}$, so that $R_{meas} \approx R_{NW}$. One way to obtain information on the contact resistance could be the application of the TLM on this kind of structures; this is, however, not possible, since the deposition of more than two I-Pt-C contacts on structures this thick would inevitably lead to lower gap resistances. We will show in chapter 5 a possible way to overcome the problem of the determination of contact resistances in a two-probe setup without applying the TLM.

4.2.3 Hydrothermal Nanowires

Eight hydrothermally synthesized samples were characterized from the electrical point of view. Two different approaches were used for the preparation of the contacts:

- **approach 1**: the contacts to the nanowires are deposited with the e-beam and the landing area for the tips is deposited with the i-beam (figure 4.14a). The main reason for the deposition by i-beam of the landing area is that the contact resistance between the tips and the pad was well characterized ($R_C \approx 300\Omega$, see section 4.1.1) and I-Pt-C shows better conductive behavior with respect to E-Pt-C

- **approach 2**: the contacts and the landing area are deposited with the e-beam (figure 4.14b). The idea behind this approach is that, since the deposition is not completely under control, it is better to reduce the number of deposition processes. The main drawback in this approach is that the contact resistance between the tips and the e-beam deposited pads is not well characterized (see section 4.1.2)

In both approaches, the deposition of the e-beam pads is performed with the optimized parameters presented in section 4.1.3, namely: 5 keV beam energy, $60\mu m$ aperture, 30° tilt. Samples $\{HT1, \dots HT4\}$ were prepared with the first

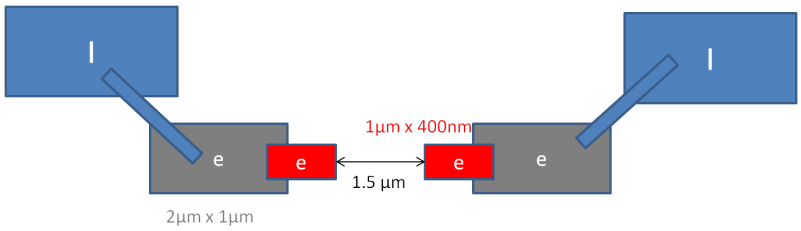

(a) Approach 1

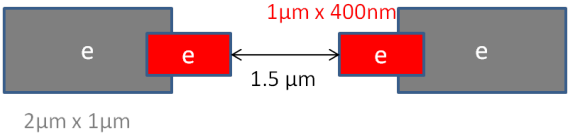

(b) Approach 2

Figure 4.14: Two different approaches to the preparation of contacts

approach, while the other samples were prepared with the second approach. All the samples were characterized with I-V sweeps, as shown in figure 4.15; the results are presented in table 4.5.

Table 4.5: I-V characterization of HT nanowires

sample	l (nm)	d (nm)	R (Ω)	ρ ($\mu\Omega cm$)
HT1	2200 ± 10	190 ± 5	$(2.62 \pm 0.07) \cdot 10^5$	$(2.8 \pm 0.2) \cdot 10^5$
HT2	2500 ± 10	300 ± 5	$(2.4 \pm 0.3) \cdot 10^5$	$(5.4 \pm 0.9) \cdot 10^5$
HT3	2200 ± 10	220 ± 5	$(1.47 \pm 0.03) \cdot 10^5$	$(2.1 \pm 0.2) \cdot 10^5$
HT4	2400 ± 10	210 ± 5	$(3.90 \pm 0.07) \cdot 10^5$	$(4.5 \pm 0.3) \cdot 10^5$
HT5	1450 ± 10	140 ± 5	$(3.161 \pm 0.003) \cdot 10^5$	$(2.7 \pm 0.2) \cdot 10^5$
HT6	1350 ± 10	110 ± 5	$(5.032 \pm 0.005) \cdot 10^5$	$(2.9 \pm 0.3) \cdot 10^5$
HT7	1620 ± 10	180 ± 5	$(1.833 \pm 0.005) \cdot 10^5$	$(2.4 \pm 0.2) \cdot 10^5$
HT8	1580 ± 10	130 ± 5	$(5.57 \pm 0.01) \cdot 10^5$	$(3.9 \pm 0.3) \cdot 10^5$

All the nanowires have linear I-V behavior in the $(-2 \div 2)$ V range; resistance was calculated as the inverse of the slope of the curves, calculated from the linear fit curve. Uncertainties in table 4.5 for samples prepared with the first approach were calculated as follows: it was possible to calculate the average value of the resistance based on repeated measurements, and the uncertainties were evaluated as $(max\ value - min\ value)/2$. The same statistical treatment was not possible for samples $HT5, HT6, HT7, HT8$: in this case, the nanowires show decreasing resistivity after repeated measurements. Therefore, only the lowest measured value is reported in the table and the uncertainty calculated from the linear fit is presented. Concerning the interpretation of the measured resistance values, it is not straight-forward as it was for the Sol-Gel microwires. In the following paragraphs, interpretation of the measurements for each deposition

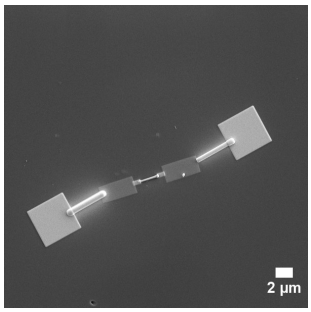

(a) FESEM image of sample HT4, prepared with approach 1

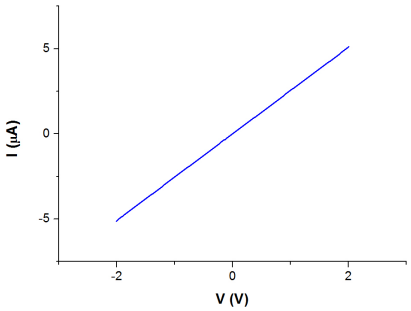

(b) I-V sweep of sample HT4 in the $(-2 \div 2)$ V range

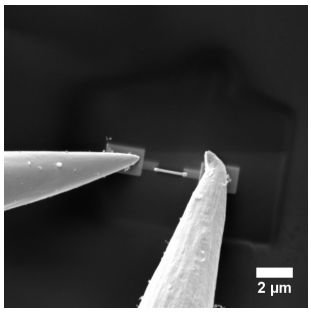

(c) FESEM image of sample HT5, prepared with approach 2

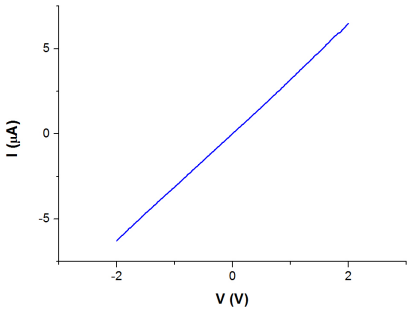

(d) I-V sweep of sample HT5 in the $(-2 \div 2)$ V range

Figure 4.15: Electrical characterization of HT NWs

approach will be given.

First approach

The electrical model presented in figure 4.4, can be simplified to

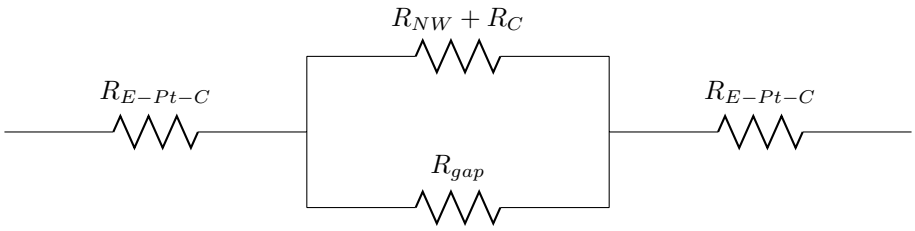

since the resistance of the i-beam deposited Pt pads and the resistance between tips and pads is negligible (section 4.1.1). The resistance of the e-beam deposited pads can be evaluated by using $\rho_{E-Pt} \approx 4 \cdot 10^5 \mu\Omega cm$ (see section 4.1.2) and taking into account the thickness of the layer ($\approx 100nm$). The estimated resistance for the E-Pt pads is therefore $\leq 10^4\Omega$. The electrical model can be simplified to

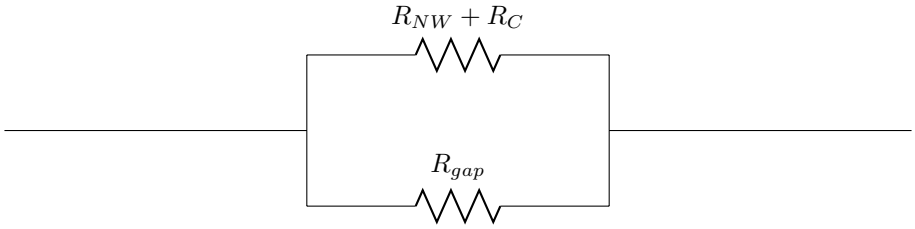

since $R_{meas} \geq 10^5\Omega$ for all the samples. The reference value for R_{gap} is $2.3 \cdot 10^6\Omega$ (see section 4.1.3), which is not negligible in this case. However, $(R_{NW} + R_C)$ can be calculated by:

$$(R_{NW} + R_C) = \frac{R_{gap} R_{meas}}{R_{gap} - R_{meas}} \tag{4.5}$$

Table 4.6 shows a comparison between the measured values for the resistance and the calculated values for $(R_{NW} + R_C)$; for simplicity, uncertainties are not reported. In order to evaluate the discrepancy between the measured values and the corrected values $R_{NW} + R_C$, their ratio is presented in table 4.6. The values $R_{NW} + R_C$, calculated from equation 4.5 are correct only if R_{gap} is accurately known. Unfortunately, since GIS conditions are not perfectly controlled and repeatable (section 4.1.3), this is not the case; therefore, when performing electrical measurements on HT NWs, the following inequality holds true:

$$R_{NW} + R_C \geq R_{meas} \tag{4.6}$$

Table 4.6: Correction to the resistance and resistivity

sample	R_{meas} (Ω)	R_{NW+C} (Ω)	R_{NW+C}/R_{meas}	ρ_{corr} ($\mu\Omega cm$)
HT1	$2.62 \cdot 10^5$	$2.93 \cdot 10^5$	1.13	$3.1 \cdot 10^5$
HT2	$2.4 \cdot 10^5$	$2.5 \cdot 10^5$	1.11	$6.0 \cdot 10^5$
HT3	$1.47 \cdot 10^5$	$1.60 \cdot 10^5$	1.07	$2.3 \cdot 10^5$
HT4	$3.90 \cdot 10^5$	$4.55 \cdot 10^5$	1.20	$5.4 \cdot 10^5$
HT5	$3.161 \cdot 10^5$	$3.583 \cdot 10^5$	1.16	$3.1 \cdot 10^5$
HT6	$5.032 \cdot 10^5$	$6.389 \cdot 10^5$	1.28	$3.7 \cdot 10^5$
HT7	$1.833 \cdot 10^5$	$1.992 \cdot 10^5$	1.06	$2.6 \cdot 10^5$
HT8	$5.57 \cdot 10^5$	$7.35 \cdot 10^5$	1.32	$5.1 \cdot 10^5$

Second approach

The electrical model for samples prepared with the second approach is

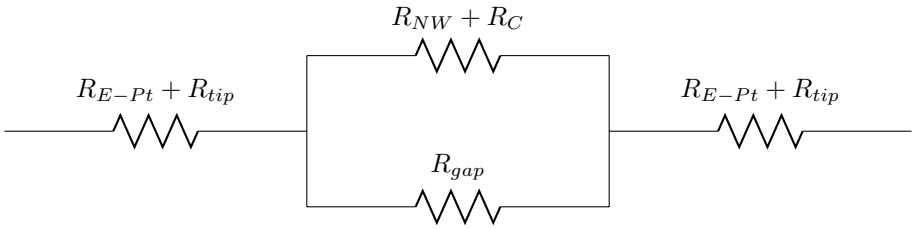

Although it was not possible to evaluate the resistance between the tip and the e-beam deposited pads with statistical significance in section 4.1.2, it is clear by looking at the TLM plot in figure 4.6c that R_{tip} cannot be higher than $10^4\Omega$. A support for this assumption will be given in chapter 5. Therefore, by using the same argumentation as in the previous paragraph, we can conclude that $R_{NW} + R_C \geq R_{meas}$.

4.2.4 LPCVD Nanowires

Nine LPCVD nanowires were characterized by using the second approach (explained in section 4.2.3) for the deposition of the conductive pads. This approach was chosen as it yields results comparable to the first approach, but it reduces the number of deposition processes, which in principle are not perfectly under control. Moreover, since LPCVD nanowires have smaller diameters with respect to the hydrothermal nanowires, it is more advisable to completely avoid interaction with the ion-beam. Typical I-V curves are shown in figure 4.16 for samples LPCVD6 and LPCVD7. The results for all measurements are shown in table 4.7. As was the case for the hydrothermal nanowires, the reported uncertainties for the resistance were calculated from the linear fit. Concerning the interpretation of the data, the same electrical model adopted for the HT NWs prepared with the second approach can be used here. Again, the contribution from the deposition halo is not negligible; calculated values for the $(R_{NW} + R_C)$ resistance are reported in table 4.8 for each nanowire.

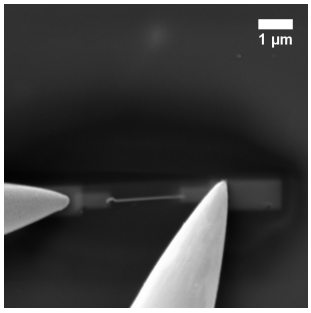

(a) FESEM image of sample LPCVD6, prepared with approach 1

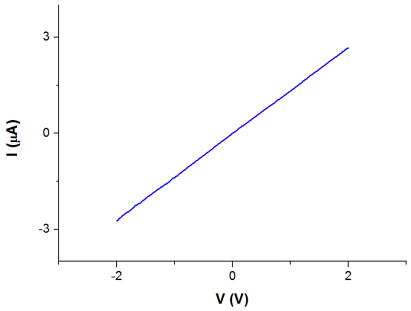

(b) I-V sweep of sample LPCVD6 in the $(-2 \div 2)$ V range

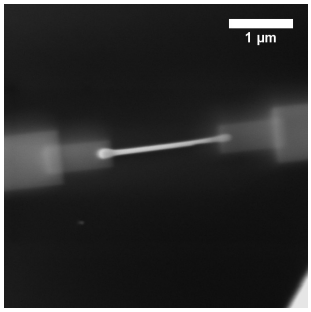

(c) FESEM image of sample LPCVD7, prepared with approach 2

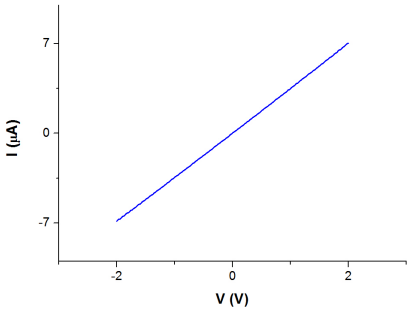

(d) I-V sweep of sample LPCVD7 in the $(-2 \div 2)$ V range

Figure 4.16: Electrical characterization of LPCVD NWs

Table 4.7: I-V characterization of LPCVD nanowires

sample	l (nm)	d (nm)	R (Ω)	ρ ($\mu\Omega cm$)
LPCVD1	2010 ± 10	80 ± 5	$(2.528 \pm 0.006) \cdot 10^5$	$(5.2 \pm 0.7) \cdot 10^4$
LPCVD2	1750 ± 10	70 ± 5	$(1.382 \pm 0.002) \cdot 10^5$	$(2.5 \pm 0.4) \cdot 10^4$
LPCVD3	2040 ± 10	50 ± 5	$(8.06 \pm 0.01) \cdot 10^5$	$(6.4 \pm 0.1) \cdot 10^4$
LPCVD4	2080 ± 10	60 ± 5	$(3.180 \pm 0.002) \cdot 10^5$	$(3.6 \pm 0.6) \cdot 10^4$
LPCVD5	1670 ± 10	60 ± 5	$(8.65 \pm 0.01) \cdot 10^5$	$(1.2 \pm 0.2) \cdot 10^5$
LPCVD6	2050 ± 10	70 ± 5	$(6.486 \pm 0.009) \cdot 10^5$	$(1.0 \pm 0.2) \cdot 10^5$
LPCVD7	1700 ± 10	80 ± 5	$(2.852 \pm 0.002) \cdot 10^5$	$(7.0 \pm 0.9) \cdot 10^4$
LPCVD8	2000 ± 10	60 ± 5	$(3.159 \pm 0.001) \cdot 10^5$	$(3.7 \pm 0.6) \cdot 10^4$
LPCVD9	1820 ± 10	50 ± 5	$(2.057 \pm 0.008) \cdot 10^5$	$(1.8 \pm 0.4) \cdot 10^4$

Table 4.8: Correction to the resistance and resistivity

sample	R_{meas} (Ω)	R_{NW+C} (Ω)	R_{NW+C}/R_{meas}	ρ_{corr} ($\mu\Omega cm$)
LPCVD1	$2.528 \cdot 10^5$	$2.840 \cdot 10^5$	1.12	$5.9 \cdot 10^4$
LPCVD2	$1.382 \cdot 10^5$	$1.470 \cdot 10^5$	1.06	$2.7 \cdot 10^4$
LPCVD3	$8.06 \cdot 10^5$	$1.241 \cdot 10^6$	1.53	$9.9 \cdot 10^4$
LPCVD4	$3.180 \cdot 10^5$	$3.690 \cdot 10^5$	1.16	$4.2 \cdot 10^4$
LPCVD5	$8.65 \cdot 10^5$	$1.385 \cdot 10^6$	1.61	$1.9 \cdot 10^5$
LPCVD6	$6.486 \cdot 10^5$	$9.033 \cdot 10^5$	1.47	$1.4 \cdot 10^5$
LPCVD7	$2.852 \cdot 10^5$	$3.256 \cdot 10^5$	1.14	$8.0 \cdot 10^4$
LPCVD8	$3.159 \cdot 10^5$	$3.662 \cdot 10^5$	1.16	$4.3 \cdot 10^4$
LPCVD9	$2.057 \cdot 10^5$	$2.259 \cdot 10^5$	1.10	$2.0 \cdot 10^4$

4.3 Large bias behavior and Joule heating

Although approximately linear at relatively low bias, the I-V characteristics of all the analysed micro/nanowires show non-linear behavior at larger bias. The deviation from the linear behavior is expected as a consequence of the back-to-back Schottky interfaces between the ZnO wires and the deposited Pt contacts. Examples of large bias I-V characteristics are shown in figure 4.17 for a sol-gel microwire and a LPCVD nanowire. It is worth noticing that such I-V curves are

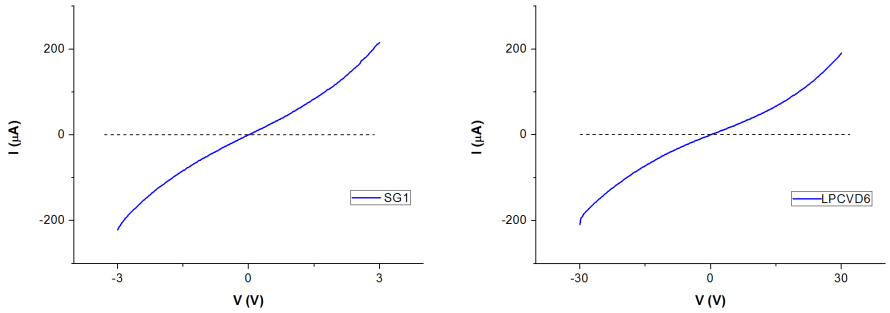

(a) I-V curve of sample SG1 in the $(-3 \div 3)$ V range

(b) I-V curve of sample LPCVD6 in the $(-30 \div 30)$ V range

Figure 4.17: Large bias I-V measurements

symmetric; therefore, differences between the two contact interfaces are negligible and the two Schottky barriers can be reasonably considered equal. Based on the calculations published by Zhang et al. [84], a second linear regime is expected at large bias, since in this conditions the dominant contribution to the total voltage drop arises from the nanowire. However, it was not possible to apply a sufficiently high bias to reach the second linear regime for the micro/nanowires studied in this thesis, due to failure of the devices under test. FESEM images of a microwire after failure and a table reporting failure conditions are shown in figure 4.18. In this table, voltage and current ranges where

(a) FESEM image of a SG microwire after failure

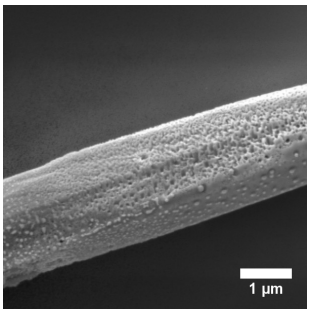

(b) High-magnification image of the microwire

sample	$V(V)$	$I(\mu A)$	$V \cdot I$ (W)
SG microwires	$(3 \div 4)$	$(200 \div 300)$	$(6 \div 8) \cdot 10^{-4}$
HT nanowires	> 10	–	–
LPCVD nanowires	$(15 \div 35)$	$(50 \div 300)$	$(10^{-3} \div 10^{-2})$

(c) Failure conditions for the studied micro/nanowires

Figure 4.18: Failure due to Joule heating

failure occurred are reported; data for the hydrothermal nanowires are missing since no failure occurred during experiments. According to the data shown in the table, nanowires can sustain much higher voltages with respect to the microwires. A major cause of failure in such devices is Joule heating, directly caused by current flow. The energy per unit time dissipated by Joule heating in a Ohmic electrical component can be expressed as:

$$P = VI \tag{4.7}$$

with V the voltage drop and I the current. Therefore, assuming that a significant part of the applied external voltage drops in the micro/nanowires, it is expected that microwires generate more Joule heat at a given voltage than nanowires as a direct consequence of equation 4.7. However, it is also clear from the data that nanowires can tolerate more thermal power than microwires before suffering failure. The capability of the device under test to dissipate Joule heat has to be taken into account. In general, heat can be transferred by three different mechanisms:

1. *conduction*: the wire is in direct contact with the insulating substrate and with the conductive pads. Since the thermal conductivity of SiO_2 is $1.4W/mK$ [85], it is expected that the majority of heat loss by conduction occurs at the contact interfaces. This contribution is directly proportional to the contact area.

2. *convection*: since the electrical characterization is performed in the SEM chamber (pressure $< 10^5$ Torr), this heat dissipation mechanism can be neglected.

3. *radiation*: radiated power is directly proportional to exposed surface of the wire.

In the literature, two different approaches have been used for the estimation of heat dissipation in this experimental condition:

- Li et al. [65] consider thermal radiation as the main source of heat loss
- Strelcov et al. [86] consider both conduction and thermal radiation as heat transfer mechanisms

For both approaches, the capability of transferring heat should be proportional to the surface area of the structure under investigation. As a consequence, microwires are expected to transfer heat more efficiently. However, as evidenced by the experiments, the microwires are able to sustain lower Joule power before failing with respect to the nanowire. This cannot be explained by the general arguments previously mentioned and further studies have to be undertaken in order to investigate Joule heating in the micro/nanowires.

4.4 Conclusions

On the basis of the acquired knowledge on the morphology of the structures under study (presented in chapter 3), preliminary studies on the in-situ deposition processes were conducted. These preliminary studies involve both I-beam and E-beam induced deposition:

- **I-beam**: the resistivity of the i-beam deposited Pt was evaluated by the Transmission Line Method as $\rho_{I-Pt-C} = 4200 \pm 300\ \mu\Omega cm$. The contact resistance between the tungsten tips and the i-beam deposited Pt was calculated as $2R_{tip} = 250 \pm 30\ \Omega$. Micropads were deposited at a distance comparable with the Sol-Gel microwires length and the gap resistance was estimated as $R_{gap} \approx 10^8 \Omega$.
- **E-beam**: the Transmission Line Method was applied for the electrical characterization of e-beam deposited Pt. The calculated resistivity is $\rho_{E-Pt-C} = (4.2 \pm 0.4) \cdot 10^5\ \mu\Omega cm$. It was not possible to estimate the resistance between the tips and the e-beam deposited Pt since the uncertainty was larger than the measured value. Nanopads were deposited with a $\approx 2\mu m$ gap, which is comparable with the average length of the hydrothermal and LPCVD nanowires. The R_{gap} resistance in this case is not completely under control: the causes were identified in the lack of perfect control and repeatability of the GIS flux and position. Deposition conditions which lead to more reproducible results were chosen.

Specific procedures for the deposition of contacts were selected, based on information gained by the morphological analysis of the wires and by the preliminary studies on the deposition processes. Two-probe I-V curves were acquired for microwires and nanowires in voltage ranges where the electrical behavior is linear, with subsequent evaluation of resistance and interpretation of the data:

- **Sol-Gel Microwires**: the measured values for the resistance lie in the range $(1.5 - 3.1) \cdot 10^4 \Omega$. Since the contribution to the total resistance by the tips, the pads and the deposition halo are all negligible, the measured resistance corresponds to $R_{MW} + R_C$, where R_C is the contact resistance between the microwire and the deposited Pt. The calculated values for the resistivity are actually related to the wires only in case $R_C << R_{MW}$ so that $R_{meas} \approx R_{MW}$.

- **Hydrothermal Nanowires**: the measured values for the resistance lie in the range $(1.5 - 5.6) \cdot 10^5 \Omega$. The contribution of the gap resistance is not negligible and the measured values must be corrected. The accuracy of this correction is dependent on the knowledge of R_{gap}, which is not completely under control.

- **LPCVD Nanowires**: the values for resistance lie in the range $(1.4 - 8.7) \cdot 10^5 \Omega$. As was the case for the HT NWs, the measured values must be corrected, taking into account the contribution from the gap resistance.

The *measured* values of the resistance for all three classes of wires are plotted in figure 4.19 as a function of the aspect-ratio l/A. For any of the wire classes

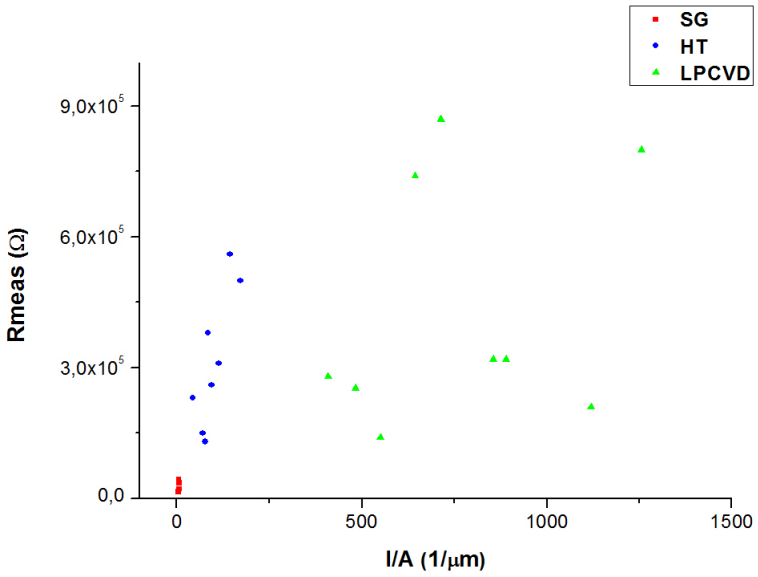

Figure 4.19: Measured values for resistance as a function of the aspect-ratio

considered in this work (MWs, NWs), information on the resistance of the wire R_{NW} is hindered by the presence of the unknown contact resistance between the wire and the in-situ deposited Pt. By performing two-probe DC measurements, this obstacle can be overcome only by the TLM method. Unfortunately, the TLM cannot be applied to any of the considered structures:

- **Sol-Gel**: since the wires have diameters in the micrometer range, micrometer-thick pads must be deposited. Therefore, deposition with the e-beam (which has limited halo effect) is not possible. In order to perform TLM, several micrometer-thick pads must be deposited with the i-beam and this would lead to uncontrollable influence of the halo on measurements.
- **Hydrothermal, LPCVD**: the halo effect absolutely hinders the possibility of depositing more than two independent contacts

Therefore, DC measurements cannot supply in this case information about the contact resistance. However, in some cases, AC two-probe measurements allow for the estimation of contact resistances. In the next chapter, the possibility of performing impedance spectroscopy measurements on single wires will be introduced.

Chapter 5

Impedance Spectroscopy

Impedance spectroscopy (IS) [87] is an important electrical characterization technique which consists in the perturbation of a material with a sinusoidal potential of low magnitude (usually $<< 1V$ but the choice depends on the particular system which needs to be characterized). Although currently impedance spectroscopy measurements are usually performed on electrochemical systems [88], this technique can be employed for the characterization of virtually any material. By the analysis of the response of the material to AC polarization, information can be gained about the contact resistance, too. This could be extremely helpful when dealing with systems where four-probe measurements are not possible, such as the case of the nanowires presented in chapter 4. To the best of our knowledge, there are only two reports that discuss the impedance spectroscopy characterization of a single nanowire ([89], [90]). There is no difference in the preparation of the samples for impedance spectroscopy with respect to the DC electrical characterization. Once contact of the tips with the deposited pads is established, IS measurements can be performed by connecting a potentiostat and a frequency-response analyzer to the micromanipulators. Concerning the measurements, an AC voltage of variable frequency is applied to the wire and the impedance of the system is measured as a function of the frequency of the voltage. Usually, the alternating voltage is superimposed to a constant DC bias voltage.

As was previously stated in chapter 4, it was not possible to measure the resistance between the tungsten tips and the e-beam deposited Pt-contacts by the transmission-line method. Since contact resistances can be measured by impedance spectroscopy, this method was applied for the estimation of the afore-mentioned tip-Pt resistance, as it will be shown in the following section. In the second part of the chapter, impedance spectroscopy measurements on hydrothermal and LPCVD nanowires will be reported.

5.1 Estimation of tip-Pt contact resistance

In chapter 3, it was shown that there exist a minority of sol-gel prepared nanowires that have different morphology with respect to the others: namely, they have intermediate dimensions between the regular sol-gel microwires and the hydrothermal nanowires. This *thin* microwires were not considered for the electrical measurements reported in chapter 4, since in principle information on the crystalline structure gained by XRD cannot be applied to them. However, *thin* microwires constitute the ideal system for the characterization of the e-beam deposited Pt contacts, mainly for two reasons:

- the length $> 5\mu m$ makes the contribution of the deposition halo negligible
- they have sufficiently small diameter to allow for electron-beam induced deposition of contacts

Since impedance spectroscopy enables in principle for the calculation of contact resistances, this method can be applied to a e-beam contacted microwire, in order to gain information about the resistance between the tungsten tips and the Pt pads. It was possible to locate a particular thin microwire which is (6.5 ± 0.1) μm long and it has (180 ± 5) nm diameter. Although the crystalline structure of the wire cannot be studied, the chemical composition of the wire is confirmed by EDX analysis. Figure 5.1 presents a FESEM image of the wire and the corresponding EDX spectrum. The contacts were deposited with the electron beam following the same procedure adopted for the LPCVD nanowires: 5 keV beam energy, 60 μm aperture, 20° tilt. The longitudinal dimensions of the contacts are kept the same as for the LPCVD NWs; the only difference was the deposition time, which was doubled in order to obtain thicker contacts. Conventional I-V curves (figure 5.2) were acquired before the impedance spectroscopy characterization. Since the I-V behavior is not perfectly linear, the resistance was evaluated by linear fitting in the $(-0.5 \div 0.5)$ V voltage range. The calculated value for resistance is $R_{I-V} = (5.234 \pm 0.008) \cdot 10^5 \Omega$. Since the gap between the contacts is > 6 μm and the deposition was performed by the e-beam, the contribution from the halo to the total resistance is negligible and the DC electrical model can be approximated with the one shown in figure 5.3. As a first step, the contribution from the pads and the tips is not considered negligible. Impedance spectroscopy measurements were performed on the same microwire by connecting a potentiostat and a frequency-response analyzer (FRA) to the micromanipulators. Five measurements were acquired, differing in the applied AC voltage and in the constant DC bias. In all measurements, the DC constant bias is $< 0.5\ V$, in order to perform the analysis in a regime where the DC electrical behavior of the microwire is approximately linear. The AC bias was optimized in order to reduce noise at lower frequencies. The frequency range in all measurements is $(1MHz \div 100Hz)$. The experimental parameters and the results are reported in table 5.1. During a typical IS measurement, the impedance of the system is measured by the frequency-response analyzer as a function of the frequency of the AC bias. IS data are usually displayed in the

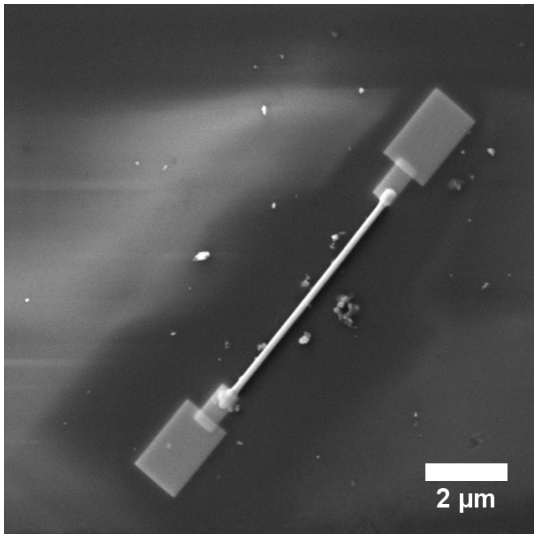

(a) FESEM image of the microwire after deposition of the contacts

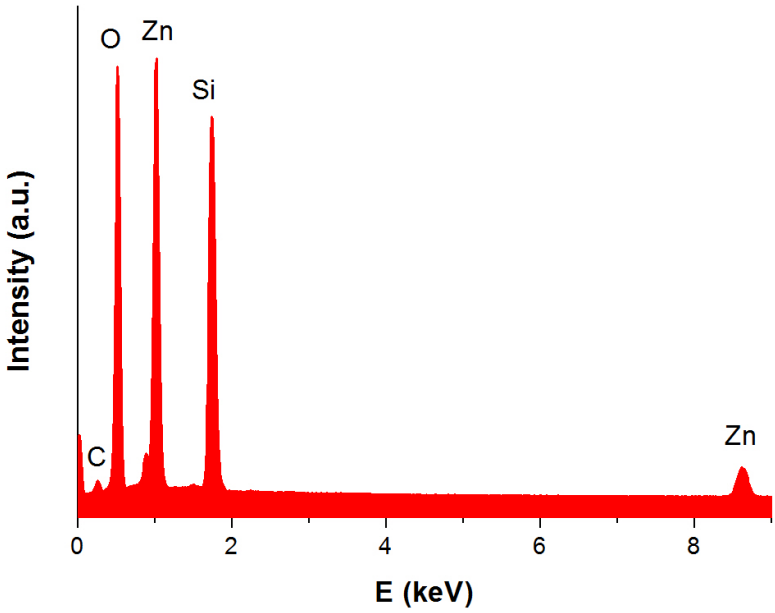

(b) EDX spectrum of the microwire

Figure 5.1: Morphology and chemical composition of the microwire

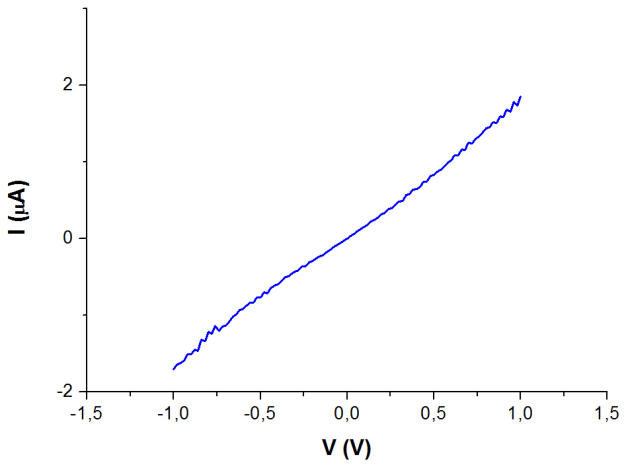

Figure 5.2: I-V curve in the range $(-1 \div 1)$ V

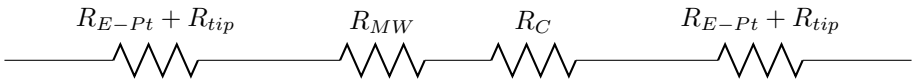

Figure 5.3: Electrical model for the DC characterization

Table 5.1: IS measurements

meas	AC (mV)	DC (V)	$2(R_{E-Pt} + R_{tip})$	$R_{MW} + R_C$	C (pF)
1	25	0.3	$7.6 \cdot 10^2\Omega$	$4.9 \cdot 10^5\Omega$	32
2	50	0.3	$7.7 \cdot 10^2\Omega$	$4.8 \cdot 10^5\Omega$	32
3	100	0.3	$6.8 \cdot 10^2\Omega$	$3.9 \cdot 10^5\Omega$	33
4	150	0.3	$7.0 \cdot 10^2\Omega$	$3.6 \cdot 10^5\Omega$	33
5	100	0.4	$7.0 \cdot 10^2\Omega$	$3.2 \cdot 10^5\Omega$	33

so-called Nyquist graphs: the values of the impedance at different frequencies are plotted in the complex plane. The Nyquist plot and the phase vs frequency plot of the fifth measurement are presented in figure 5.4 as an example. Usually,

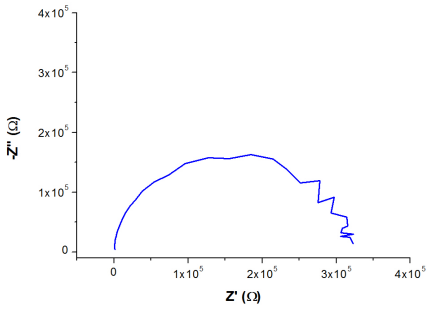

(a) Nyquist plot: the signal at low-frequencies (right-hand side of the plot) is noisy

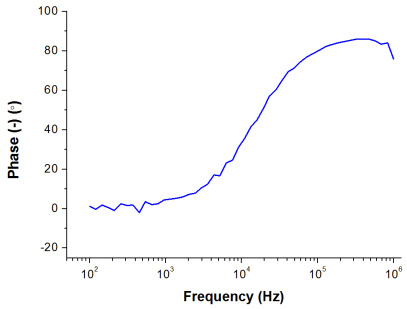

(b) Phase vs frequency plot: at higher frequencies the capacitive behavior prevails

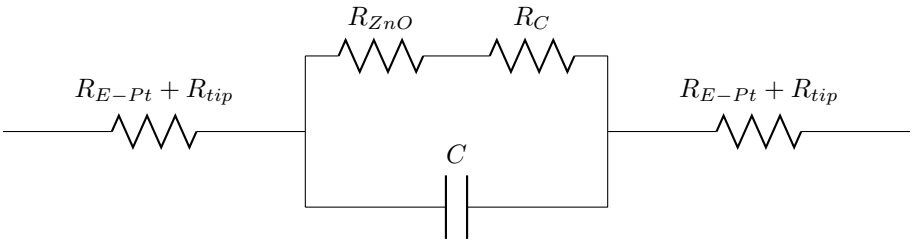

(c) Electric model

Figure 5.4

semicircle Nyquist plots shifted from the origin are obtained by systems composed of a resistor in series with the parallel combination of a capacitor and a resistor [91]. Therefore, the electrical model shown in figure 5.4c is proposed for the interpretation of the data. The total impedance of the system is described by the equation:

$$Z_{tot} = 2(R_{E-Pt} + R_{tip}) + \left(\frac{1}{(R_{MW} + R_C)} + j\omega C \right)^{-1} \tag{5.1}$$

with ω related to the frequency by $\omega = 2\pi\nu$ and j the imaginary unit. The electrical model was used to fit the acquired data with the IS analysis software *ZSimpWin*; the results shown in table 5.1 can be visualized in the Nyquist plot as follows:

- $2(R_{E-Pt} + R_{tip})$: it is equal to the shift of the semicircle from the origin along the real axis
- $R_{MW} + R_C$: it is equal the diameter of the semicircle

It is now clear from the IS data that the assumption (made in chapter 4) that the contribution to the total resistance of the system by the e-deposited pads and by the interface between tips and pads is negligible holds true. In this case, the $R_{E-Pt} + R_{tip}$ resistance is three orders of magnitude lower than the $R_{MW} + R_C$ resistance. Concerning the capacitance, the electrical model presented in figure 5.4c assumes that the contribution to the capacitance of the system arises from both the wire and the contact regions between ZnO an Pt. This assumption is justified by the fact that the contacts are not perfect Ohmic contacts (the response of the system to DC biasing is not perfectly linear). It is important to notice that if the two metal/semiconductor interfaces were modeled as pure resistors, their contribution to the total resistance would be completely translated in a shift from the origin in the Nyquist plot; therefore, the resistance calculated as the diameter of the semicircle would be the *actual* microwire resistance. Further insight on the interpretation of impedance spectroscopy measurements will be given in section 5.3.

Table 5.2: IS measurements for HT and LPCVD nanowires

sample	AC (mV)	DC (V)	$2(R_{E-Pt} + R_{tip})$	$R_{NW} + R_C$	C (pF)
HT8	100	0.4	$(3.2 \pm 2.8) \cdot 10^2\Omega$	$(4.3 \pm 0.1) \cdot 10^5\Omega$	31 ± 3
LPCVD8	100	0.4	$(5.9 \pm 1.2) \cdot 10^2\Omega$	$3.6 \pm 0.1) \cdot 10^5\Omega$	34 ± 2
LPCVD9	100	0.4	$(5.7 \pm 1.1) \cdot 10^2\Omega$	$(2.1 \pm 0.1) \cdot 10^5\Omega$	34 ± 2

5.2 IS measurements on single nanowires

In this section, the impedance spectroscopy characterization of three different nanowires is presented, specifically:

- sample HT8: hydrothermal nanowires
- samples LPCVD8, LPCVD9: low-pressure chemical vapor deposition nanowires

whose I-V behavior was already presented in chapter 4. All the samples were prepared in the same way, by e-beam deposition of contacts in the same conditions: 5 keV beam energy, 60 μm aperture, 20° tilt. The Nyquist graphs obtained from impedance spectroscopy measurements are presented in figure 5.5. All the measurements were acquired with $0.4V$ DC bias and $100mV$ AC polarization: the DC bias lies in the linear region of the I-V behavior of the considered nanowires and the choice for the AC amplitude was dictated by minimization of noise during the measurements. As was the case for the *thin* microwire analysed in the previous section, the impedance response of all the nanowires can be obtained by fitting with the equivalent model shown in figure 5.4. As a consequence, the total impedance of the system is described by the equation:

$$Z_{tot} = 2(R_{E-Pt} + R_{tip}) + \left(\frac{1}{(R_{NW} + R_C)} + j\omega C \right)^{-1} \tag{5.2}$$

The values calculated by fitting with the equivalent electrical model are reported in table 5.2. It is interesting to notice that the contact resistances, which receive contribution form both the tip-Pt interface and the e-beam deposited pads, are completely negligible with respect to the total measured resistance. Moreover, the calculated values for samples LPCVD8 and LPCVD9 are comparable with the corresponding value of $2(R_{E-Pt} + R_{tip})$ that was measured in the case of the thin microwire. The measured value for $2(R_{E-Pt} + R_{tip})$ is even lower (approximately a half); however, it could be a consequence of noisy measurements (figure 5.5b) which in turn could lead to high uncertainties for the fit parameters. In any case, these measurements prove that the assumption made in chapter 4 that $2(R_{E-Pt} + R_{tip})$ is negligible with respect to the total measured resistance holds true.

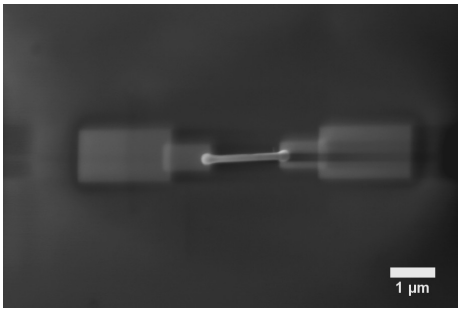

(a) FESEM image of sample HT8

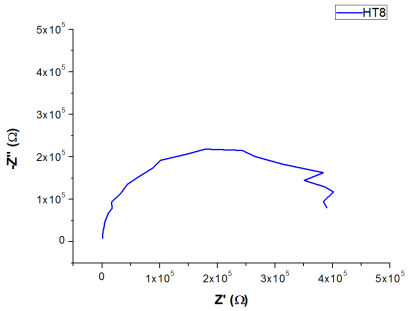

(b) Nyquist graph for sample HT8

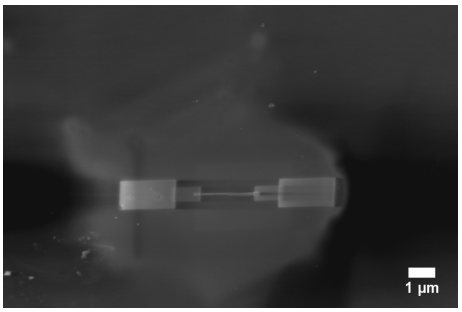

(c) FESEM image of sample LPCVD8

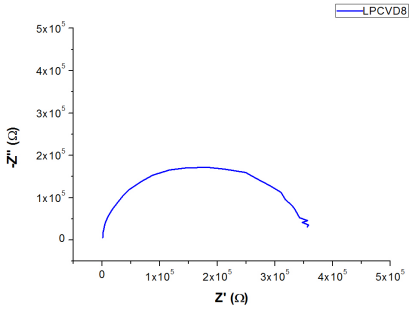

(d) Nyquist graph for sample LPCVD8

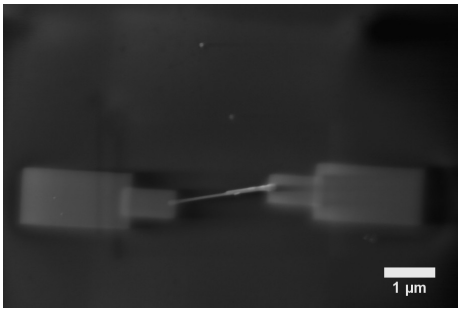

(e) FESEM image of sample LPCVD9

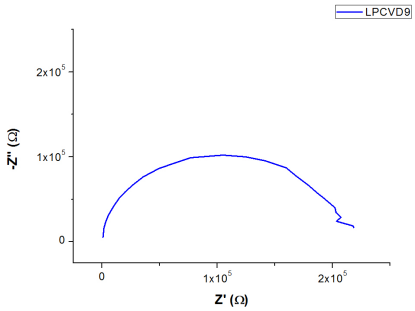

(f) Nyquist graph for sample LPCVD9

Figure 5.5: IS characterization of nanowires

5.3 Insight into the interpretation of IS data

According to the experimental results presented in the previous sections, the AC response of each of the analysed micro/nanowires can modeled as:

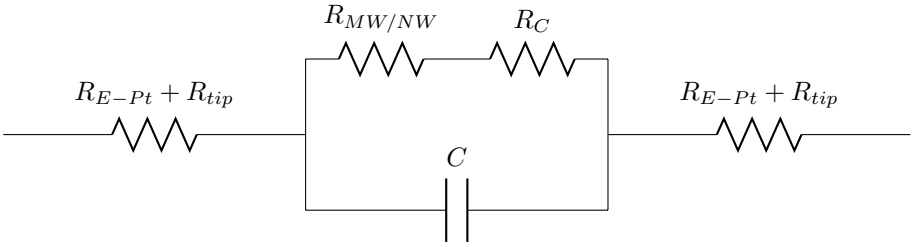

As was previously stated in section 4.2.1, the interfaces between the ZnO nanowire and the Pt contacts can be electrically modeled as back-to-back Schottky diodes. Therefore, although each impedance measurement was performed in the linear regime (low DC bias), the AC behavior of the contacts cannot in principle be modeled as purely resistive under AC polarization. In general, a Schottky diode can be modeled as a resistance in parallel with a capacitance [83]. According to this assumption, the AC response of the system can modeled as in figure 5.6.

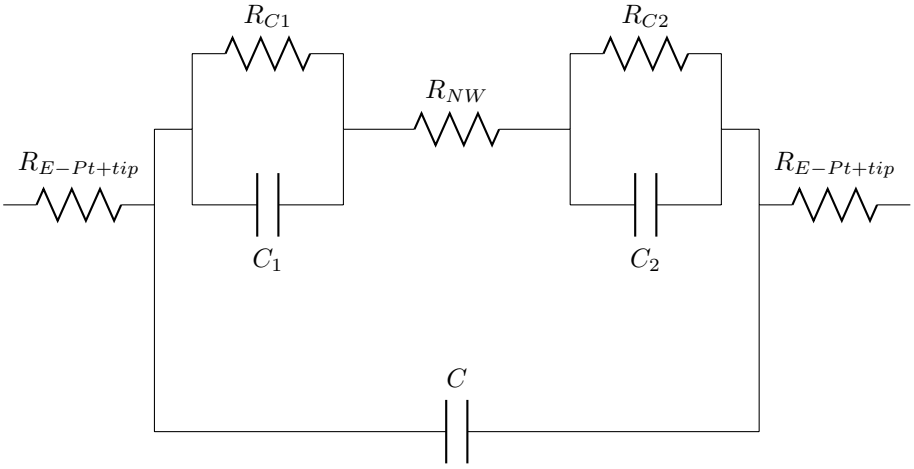

Figure 5.6: AC electrical model

However, the model in figure 5.6 does not in principle lead to semicircle Nyquist graphs such as the ones that were acquired for each nanowire. As a possible explanation, one has to consider the time constant RC associated with each Schottky contact. The time constant associated to the Schottky interface (for example interface 1) can be calculated by $R_{C1}C_1$; since the frequency range in the experiments was $(1MHz \div 100Hz)$, electrical responses characterized

by time constants $< 10^{-6}$ s cannot be measured. The depletion capacitance associated with a metal-semiconductor junction is expected to assume very small values ($C \approx 10^{-15}$ F [90]); therefore, unless R_C takes values $> 10^8\Omega$, the effect of the ZnO/Pt contacts is not measured. For frequencies much lower than $(R_{C1}C_1)^{-1}$, the contact behaves as a resistance with value R_C. In this case, the equivalent circuit turns into the one shown in figure 5.7, which reproduces the measured AC response for each nanowire.

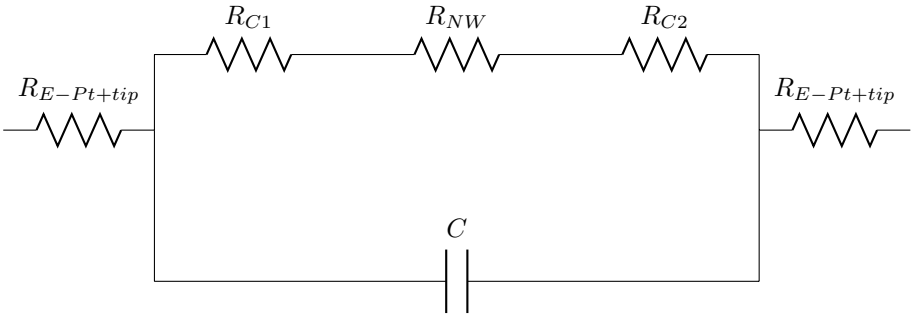

Figure 5.7: Equivalent IS model

Concerning the capacitance C, it is interpreted in the literature as a parasitic capacitance arising from the interaction between the nanowire, the contacts and the dielectric substrate ([90], [92]). However, it was evidenced by test measurements (not shown here) on Pt-strips deposited on the same substrates that the capacitance C emerges only in the presence of micro/nanowires. Therefore, in the model presented in figure 5.7 the capacitance C is associated only to the micro/nanowire and contact region. Further studies are needed in order to gain understanding on the nature of this capacitance.

Chapter 6

Conclusions and Further Developments

In conclusion, this thesis work consisted of two parts:

- **morphological and structural investigation of ZnO nanostructured thin films and micro/nanowires**
- **in-situ electrical characterization of ZnO micro/nanowires**

Morphological and structural characterization

Concerning the first point, two classes of ZnO thin films were studied: columnar compact films and sponge-like films. Their different morphologies, which were characterized by FESEM, make them suitable for different target applications. Polycrystalline columnar films are deposited by sputtering mainly in view of piezoelectric applications; piezoelectric response is critically influenced by crystalline orientation of the grains and therefore the crystalline structure of the films was characterized by XRD and TEM (high-resolution imaging and selected-area electron diffraction). Sponge-like films have radically different morphology, characterized by a high specific surface area, which makes them suitable for their employment as photoanodes in DSSCs or water-splitting cells. They are obtained by oxidation of porous Zn films deposited by sputtering; the preservation of the high specific surface area of the original metallic film was assessed by FESEM characterization and the complete oxidation was confirmed by EDX analysis.

Wire-like ZnO structures synthesized with three different methods were studied:

- microwires obtained by a sol-gel process
- nanowires synthesized by the hydrothermal method:
- nanowires grown by low-pressure chemical vapor deposition

Table 6.1: Micro/nanowire morphology and crystalline structure

sample	Structure	length	diameter
SG MWs	wurtzite	$(8-30)\mu m$	$(0.9-2.7)\mu m$
HT NWs	wurtz., sin. crystal	$(1.3-2.5)\mu m$	$(80-300)nm$
LPCVD NWs	wurtz., sin. crystal	$(1.6-2.2)\mu m$	$(50-80)nm$

The morphology of all the samples was characterized by FESEM, while the analysis of the crystalline structure was conducted by XRD and high-resolution TEM. The results are briefly summarized in table 6.1. It turns out that the sol-gel method leads to the growth of microwires, while the hydrothermal method and the low-pressure chemical vapor deposition yield single crystal nanowires.

In-situ electrical characterization

The second part of this thesis work presents an investigation on the experimental set-up for the electrical characterization of nanostructures, focusing on the in-situ deposition of contacts on the ZnO wires for two-probe electrical characterization. This activity has two main goals:

- determination of contact deposition procedures based on the morphology of the nanostructures under study
- application of these techniques to ZnO wires with tree different morphologies

In order to correctly interpret the measured data, preliminary studies on the deposited materials were conducted:

- **I-beam deposited Pt**: the resistivity of the i-beam deposited Pt was evaluated by the Transmission Line Method as $\rho_{I-Pt-C} = 4200 \pm 300\ \mu\Omega cm$. The contact resistance between the tungsten tips and the i-beam deposited Pt was measured as $2R_{tip} = 250 \pm 30\ \Omega$. A study on the deposited halo (a consequence of delocalized deposition) shows that the resistance between pads separated by a gap $> 10\mu m$ is $\geq 10^8\Omega$.
- **E-beam deposited Pt**: the Transmission Line Method was applied for the electrical characterization of e-beam deposited Pt. The calculated resistivity is $\rho_{E-Pt-C} = (4.2 \pm 0.4) \cdot 10^5\ \mu\Omega cm$. By impedance spectroscopy, it was found that the resistance between the tungsten tips and e-beam deposited Pt must satisfy the condition $2R_{tip} < 10^3\Omega$. Nanopads were deposited with a $\approx 2\mu m$ gap. The lack of perfect control and repeatability of the GIS flux and position were identified as causes for the fluctuation of the measured R_{gap} values in the range $(1 \cdot 10^5 \div 3 \cdot 10^6\Omega)$. Deposition conditions which lead to more reproducible results were identified; R_{gap} was estimated to be $\approx 10^6\Omega$ in these conditions.

Preliminary information on the morphology of the nanostructures determines the specific procedure for the deposition of the contacts; in the case of wire-like structures:

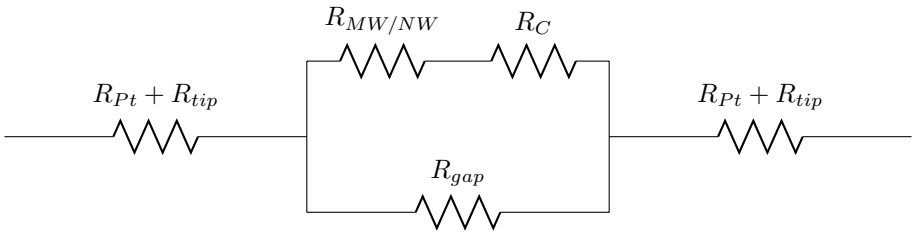

Figure 6.1: DC electrical model

- the diameter plays a role in the choice between e-beam or i-beam deposition: thicker structures require thicker contacts. Since ion deposition has a higher growth-rate, it can be considered as an option for thicker structures
- the length of the wires determines the gap length. Ion beam induced deposition must be avoided when dealing with nanostructures whose length is just few micrometers

After deposition of the contacts, the DC response of the system can be investigated by the acquisition of I-V curves. The measured resistance is interpreted by means of the electrical model shown in figure 6.1, with R_{Pt} the resistance of the pads, R_{tip} the resistance between tips and pads, $R_{MW/NW}$ the resistance of the micro/nanowire, R_C the contact resistance at the interface between the wire and the Pt contacts. Interpretation of the data was made for all the wire morphologies under study:

- **Sol-gel microwires**:

  $$R_{meas} \approx R_{MW} + R_C$$

  The measured values for the resistance lie in the range $(1.5{\cdot}10^4 \div 4.0{\cdot}10^4)\Omega$. Since R_C is unknown, these values have to be considered as upper limits for the resistance of the wire

  $$R_{MW} \leq R_{meas}$$

- **Hydrothermal nanowires**:

  $$R_{meas} \approx (R_{NW} + R_C) \cdot R_{gap}/(R_{NW} + R_C + R_{gap})$$

  In this case, the contribution from the delocalized halo is not negligible; by assuming $R_{gap} \approx 2 \cdot 10^6\Omega$ as a reference value for the gap resistance, calculation of $R_{NW} + R_C$ is possible. The calculated values lie in the range $(1.6 \cdot 10^5 \div 7.4 \cdot 10^5)\Omega$. Again, these values are upper limits for the resistance of the wires.

Table 6.2: Evaluation of resistivity

sample	resistivity
Sol-Gel	$\rho = (3.0 \div 5.8) \cdot 10^5 \mu\Omega cm$
Hydrothermal	$\rho = (2.3 \div 6.0) \cdot 10^5 \mu\Omega cm$
LPCVD	$\rho = (0.2 \div 1.9) \cdot 10^5 \mu\Omega cm$

- **LPCVD nanowires**:

$$R_{meas} \approx (R_{NW} + R_C) \cdot R_{gap}/(R_{NW} + R_C + R_{gap})$$

  Concerning the interpretation of LPCVD data, the same argumentation used for the hydrothermal nanowires holds true in this case. The calculated values for $R_{NW} + R_C$ lie in the range $(1.4 \cdot 10^5 \div 1.4 \cdot 10^6)\Omega$.

Since the R_C value is unknown, calculation of the resistivity of the wires is not expected to be accurate. However, by assuming that the majority of the contribution to the $R_{MW/NW} + R_C$ resistance comes from $R_{MW/NW}$, a qualitative calculation of the resistivity can be performed for all the wires. The results are presented in table 6.2. In fact, these results are comparable with most of the studies on the electrical characterization of single ZnO nanowires [62]. In particular, they are in agreement with most recent studies , such as those reported by Lord et al. [66] and by Geng et al. [68]. In these studies, made on both hydrothermal and CVD nanowires, the reported resistivity values are in the range $10^5 \div 10^6 \mu\Omega cm$. It must be stressed that both works adopted different techniques for the characterization of the wires: in [66], measurements were acquired by direct contact to the wires by four tungsten tips, while in [68], the EBL approach is reported. The main drawback of the two-probe approach adopted in this thesis work is that the resistance between the wire and the Pt contacts is unknown; however, it is worth noticing that, to the best of our knowledge, four-probe measurements on nanowires with length $\approx 2\mu m$ are yet to be reported. This is probably due to technological issues in the deposition of four contacts at this scale without leakage current on selectable nanowires. However, impedance spectroscopy (IS) measurements allow in some cases the determination of contact resistances in a two-probe configuration. IS analysis on a single microwire and single nanowires is presented in the final part of this work. It is shown that the electrical response of the system to a AC voltage in the absence of contribution from the delocalized halo can be modeled as the one presented in figure 6.2: The total impedance of the system is described by the equation:

$$Z_{tot} = 2(R_{Pt} + R_{tip}) + \left(\frac{1}{(R_{MW/NW} + R_C)} + j\omega C \right)^{-1} \tag{6.1}$$

with ω related to the frequency by $\omega = 2\pi\nu$ and j the imaginary unit. By fitting the data, $(R_{Pt} + R_{tip})$, $(R_{MW} + R_C)$ and the capacitance C can be calculated. It is worth noticing that if one was able to prove that the contribution from

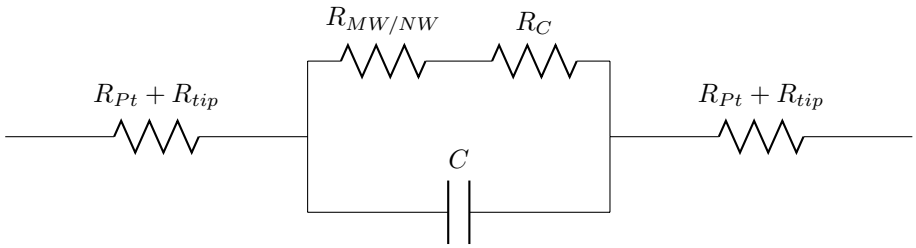

Figure 6.2: IS electrical model

the ZnO/Pt is purely resistive and that the capacitance does not involve the ZnO/Pt contacts, R_C would be incorporated in the total contact resistance, enabling direct calculation of the $R_{MW/NW}$ resistance. This could be really useful for systems where four-probe measurements are difficult or not possible, such as the hydrothermal and the LPCVD nanowires presented in this work. Therefore, two aspects of the in-situ electrical characterization technique must be improved in order to fully exploit impedance spectroscopy measurements:

1. minimization of the halo effect when working with low-length nanowires
2. thorough study of the ZnO/Pt interface electrical behavior

References

[1] Zhong Lin Wang. ZnO nanowire and nanobelt platform for nanotechnology. *Materials Science and Engineering: R: Reports*, 64:33 – 71, 2009.

[2] Z.C. Feng. *Handbook of Zinc Oxide and Related Materials: Volume One, Materials*. Electronic materials and devices series. Taylor & Francis, 2012.

[3] New Jersey Zinc Company and H.E. Brown. *Zinc Oxide Rediscovered*. New Jersey Zinc Company, 1957.

[4] O. Dulub, L.A. Boatner, and U. Diebold. Stm study of the geometric and electronic structure of ZnO(0 0 0 1)-Zn, (0 0 0 1)-O, (1 0 1 0), and (1 1 2 0) surfaces. *Surface Science*, 519(3):201–217, 2002.

[5] Umit Ozgur and Hadis Morkoc. *Zinc Oxide: Fundamentals, Materials and Device Technology*. Wiley, 2007.

[6] Dragan Damjanovic. Ferroelectric, dielectric and piezoelectric properties of ferroelectric thin films and ceramics. *Reports on Progress in Physics*, 61(9):1267, 1998.

[7] I.B. Kobiakov. Elastic, piezoelectric and dielectric properties of zno and cds single crystals in a wide range of temperatures. *Solid State Communications*, 35(3):305 – 310, 1980.

[8] Andrea Dal Corso, Michel Posternak, Raffaele Resta, and Alfonso Baldereschi. Ab initio. *Phys. Rev. B*, 50:10715–10721, Oct 1994.

[9] Gene H. Haertling. Ferroelectric ceramics: History and technology. *Journal of the American Ceramic Society*, 82(4):797–818, 1999.

[10] S. O. Kucheyev, J. E. Bradby, J. S. Williams, C. Jagadish, and M. V. Swain. Mechanical deformation of single-crystal ZnO. *Applied Physics Letters*, 80(6):956–958, 2002.

[11] S. O. Kucheyev, J. E. Bradby, J. S. Williams, C. Jagadish, M. Toth, M. R. Phillips, and M. V. Swain. Nanoindentation of epitaxial GaN films. *Applied Physics Letters*, 77(21):3373–3375, 2000.

[12] Robert E. Newnham. *Properties of materials anisotropy, symmetry, structure*. Oxford University Press, 2005.

[13] H. Iwanaga, A. Kunishige, and S. Takeuchi. Anisotropic thermal expansion in wurtzite-type crystals. *Journal of Materials Science*, 35(10):2451–2454, 2000.

[14] A. Mang, K. Reimann, and St. R.benacke. Band gaps, crystal-field splitting, spin-orbit coupling, and exciton binding energies in ZnO under hydrostatic pressure. *Solid State Communications*, 94(4):251 – 254, 1995.

[15] Y.P. Varshni. Temperature dependence of the energy gap in semiconductors. *Physica*, 34(1):149 – 154, 1967.

[16] M.D. McCluskey and S.J. Jokela. Defects in ZnO. *Journal of Applied Physics*, 106(7), 2009.

[17] D.C. Look, D.C. Reynolds, J.R. Sizelove, R.L. Jones, C.W. Litton, G. Cantwell, and W.C. Harsch. Electrical properties of bulk ZnO. *Solid State Communications*, 105(6):399 – 401, 1998.

[18] F.K. Shan, G.X. Liu, W.J. Lee, G.H. Lee, I.S. Kim, B.C. Shin, and Y.C. Kim. Transparent conductive ZnO thin films on glass substrates deposited by pulsed laser deposition. *Journal of Crystal Growth*, 277:284 – 292, 2005.

[19] F.K. Shan, B.C. Shin, S.W. Jang, and Y.S. Yu. Substrate effects of ZnO thin films prepared by {PLD} technique. *Journal of the European Ceramic Society*, 24(6):1015 – 1018, 2004.

[20] Z.Q. Chen, S. Yamamoto, A. Kawasuso, Y. Xu, and T. Sekiguchi. Characterization of homoepitaxial and heteroepitaxial ZnO films grown by pulsed laser deposition. *Applied Surface Science*, 244:377 – 380, 2005.

[21] Y. Kashiwaba, K. Haga, H. Watanabe, B.P. Zhang, Y. Segawa, and K. Wakatsuki. Structures and photoluminescence properties of ZnO films epitaxially grown by atmospheric pressure mocvd. *physica status solidi (b)*, 229(2):921–924, 2002.

[22] Yefan Chen, D.M. Bagnall, Ziqiang Zhu, Takashi Sekiuchi, Ki tae Park, Kenji Hiraga, Takafumi Yao, S. Koyama, M.Y. Shen, and T. Goto. Growth of ZnO single crystal thin films on c-plane (0 0 0 1) sapphire by plasma enhanced molecular beam epitaxy. *Journal of Crystal Growth*, 181:165 – 169, 1997.

[23] Keiichiro Sakurai, Masahiko Kanehiro, Ken Nakahara, Tetsuhiro Tanabe, Shizuo Fujita, and Shigeo Fujita. Effects of substrate offset angles on {MBE} growth of ZnO. *Journal of Crystal Growth*, 214-215(0):92 – 94, 2000.

[24] Wei Gao and Zhengwei Li. Zno thin films produced by magnetron sputtering. *Ceramics International*, 30(7):1155 – 1159, 2004. 3rd Asian Meeting on Electroceramics.

[25] Chennupati Jagadish and Stephen J. Pearton. *Zinc Oxide Bulk, Thin Films and Nanostructures*. Elsevier, 2006.

[26] Xiang Yang Kong, Yong Ding, Rusen Yang, and Zhong Lin Wang. Single-crystal nanorings formed by epitaxial self-coiling of polar nanobelts. *Science*, 303(5662):1348–1351, 2004.

[27] Xiang Yang Kong and Zhong Lin Wang. Polar-surface dominated ZnO nanobelts and the electrostatic energy induced nanohelixes, nanosprings, and nanospirals. *Applied Physics Letters*, 84(6):975–977, 2004.

[28] Ado Jorio, Gene Dresselhaus, and Mildred S Dresselhaus. *Carbon nanotubes: advanced topics in the synthesis, structure, properties and applications*, volume 111. Springer, 2007.

[29] Volker Schmidt, Joerg V. Wittemann, Stephan Senz, and Ulrich G?ele. Silicon nanowires: A review on aspects of their growth and their electrical properties. *Advanced Materials*, 21(25-26):2681–2702, 2009.

[30] Huijuan Zhou, Johannes Fallert, Janos Sartor, Roman JB Dietz, Claus Klingshirn, Heinz Kalt, Daniel Weissenberger, Dagmar Gerthsen, Haibo Zeng, and Weiping Cai. Ordered n-type ZnO nanorod arrays. *Applied Physics Letters*, 92(13):132112–132112, 2008.

[31] Sheng Xu and ZhongLin Wang. One-dimensional ZnO nanostructures: Solution growth and functional properties. *Nano Research*, 4(11):1013–1098, 2011.

[32] Yen-Hsing Chen, Yu-Min Shen, Sheng-Chang Wang, and Jow-Lay Huang. Fabrication of one-dimensional ZnO nanotube and nanowire arrays with an anodic alumina oxide template via electrochemical deposition. *Thin Solid Films*, 2014.

[33] William L. Hughes and Zhong L. Wang. Controlled synthesis and manipulation of ZnO nanorings and nanobows. *Applied Physics Letters*, 86, 2005.

[34] B. P. Zhang, N. T. Binh, K. Wakatsuki, Y. Segawa, Y. Yamada, N. Usami, M. Kawasaki, and H. Koinuma. Formation of highly aligned ZnO tubes on sapphire (0001) substrates. *Applied Physics Letters*, 84:4098–4100, 2004.

[35] Y. Xi, W.Z. Wu, H. Fang, and C.G. Hu. Integrated ZnO nanotube arrays as efficient dye-sensitized solar cells. *Journal of Alloys and Compounds*, 529:163 – 168, 2012.

[36] Lijuan Luo, Gang Lv, Bihui Li, Xiaoyan Hu, Lei Jin, Jianbo Wang, and Yiwen Tang. Formation of aligned ZnO nanotube arrays by chemical etching and coupling with CdSe for photovoltaic application. *Thin Solid Films*, 518(18):5146 – 5152, 2010.

[37] Y. W. Heo, L. C. Tien, Y. Kwon, D. P. Norton, S. J. Pearton, B. S. Kang, and F. Ren. Depletion-mode ZnO nanowire field-effect transistor. *Applied Physics Letters*, 85(12):2274–2276, 2004.

[38] M.S. Arnold, P. Avouris, Z.W. Pan, and Z.L. Wang. Field-effect transistors based on single semiconducting oxide nanobelts. *Journal of Physical Chemistry B*, 107(3):659–663, 2003.

[39] Z.L. Wang and J. Song. Piezoelectric nanogenerators based on zinc oxide nanowire arrays. *Science*, 312(5771):243–246, 2006.

[40] Q. Zhang, C.S. Dandeneau, X. Zhou, and C. Cao. Zno nanostructures for dye-sensitized solar cells. *Advanced Materials*, 21(41):4087–4108, 2009.

[41] O. Lupan, G.A. Emelchenko, V.V. Ursaki, G. Chai, A.N. Redkin, A.N. Gruzintsev, I.M. Tiginyanu, L. Chow, L.K. Ono, B. Roldan Cuenya, H. Heinrich, and E.E. Yakimov. Synthesis and characterization of ZnO nanowires for nanosensor applications. *Materials Research Bulletin*, 45(8):1026 – 1032, 2010.

[42] Vinay Gupta. Zno based third generation biosensor. *Thin Solid Films*, 519(3):1141 – 1144, 2010. Biomolecular Electronics and Organic Nanotechnology for Environmental Preservation.

[43] D.B. Williams and C. Barry Carter. *Transmission Electron Microscopy*. Springer, 2009.

[44] Pierre Hovington, Dominique Drouin, and Raynald Gauvin. Casino: A new monte carlo code in c language for electron beam interaction ?part i: Description of the program. *Scanning*, 19(1):1–14, 1997.

[45] J. Goldstein. *Scanning Electron Microscopy and X-Ray Microanalysis*. Springer, 2007.

[46] I. Utke, S. Moshkalev, and P. Russell. *Nanofabrication Using Focused Ion and Electron Beams: Principles and Applications*. Nanomanufacturing series. Oxford University Press, USA, 2012.

[47] S J Pennycook. Z-contrast transmission electron microscopy: Direct atomic imaging of materials. *Annual Review of Materials Science*, 22(1):171–195, 1992.

[48] M.T. Postek and A.E. Vladr. Helium ion microscopy and its application to nanotechnology and nanometrology. *Scanning*, 30(6):457–462, 2008.

[49] R. Hill and F.H.M. Faridur Rahman. Advances in helium ion microscopy. *Nuclear Instruments and Methods in Physics Research, Section A: Accelerators, Spectrometers, Detectors and Associated Equipment*, 645(1):96–101, 2011.

[50] Lucille A. Giannuzzi and Fred A. Stevie. *Introduction to Focused Ion Beams*. Springer, 2005.

[51] Jon Orloff, Mark Utlaut, and Lynwood Swanson. *High Resolution Focused Ion Beams*. Kluwer Academic, 2003.

[52] Chiara Lucarotti, Calogero Maria Oddo, Nicola Vitiello, and Maria Chiara Carrozza. Synthetic and bio-artificial tactile sensing: A review. *Sensors*, 13(2):1435–1466, 2013.

[53] B. O'Regan and M. Gratzel. A low-cost, high-efficiency solar cell based on dye-sensitized colloidal TiO2 films. *Nature*, 353(6346):737–740, 1991.

[54] Kwang-Soon Ahn, Sudhakar Shet, Todd Deutsch, Chun-Sheng Jiang, Yanfa Yan, Mowafak Al-Jassim, and John Turner. Enhancement of photoelectrochemical response by aligned nanorods in ZnO thin films. *Journal of Power Sources*, 176(1):387 – 392, 2008.

[55] A Van der Drift. Evolutionary selection, a principle governing growth orientation in vapour-deposited layers. *Philips Res. Rep*, 22(3):267–88, 1967.

[56] A. Lamberti, R. Gazia, A. Sacco, S. Bianco, M. Quaglio, A. Chiodoni, E. Tresso, and C.F. Pirri. Coral-shaped ZnO nanostructures for dye-sensitized solar cell photoanodes. *Progress in Photovoltaics: Research and Applications*, 22(2):189–197, 2014.

[57] V. Cauda, D. Pugliese, N. Garino, A. Sacco, S. Bianco, F. Bella, A. Lamberti, and C. Gerbaldi. Multi-functional energy conversion and storage electrodes using flower-like zinc oxide nanostructures. *Energy*, 65:639–646, 2014.

[58] V.F. Rivera, F. Auras, P. Motto, S. Stassi, G. Canavese, E. Celasco, T. Bein, B. Onida, and V. Cauda. Length-dependent charge generation from vertical arrays of high-aspect-ratio ZnO nanowires. *Chemistry - A European Journal*, 19(43):14665–14674, 2013. cited By (since 1996)6.

[59] Chengkun Xu, Paul Shin, Liangliang Cao, and Di Gao. Preferential growth of long ZnO nanowire array and its application in dye-sensitized solar cells. *The Journal of Physical Chemistry C*, 114(1):125–129, 2010.

[60] Hyun Wook Kang, Junyeob Yeo, Jin Ok Hwang, Sukjoon Hong, Phillip Lee, Seung Yong Han, Jin Hwan Lee, Yoon Soo Rho, Sang Ouk Kim, Seung Hwan Ko, et al. Simple ZnO nanowires patterned growth by microcontact printing for high performance field emission device. *The Journal of Physical Chemistry C*, 115(23):11435–11441, 2011.

[61] H.D. Espinosa, R.A. Bernal, and M. Minary-Jolandan. A review of mechanical and electromechanical properties of piezoelectric nanowires. *Advanced Materials*, 24(34):4656–4675, 2012.

[62] E Schlenker, A Bakin, T Weimann, P Hinze, D H Weber, A Golzhuser, H-H Wehmann, and A Waag. On the difficulties in characterizing ZnO nanowires. *Nanotechnology*, 19(36):365707, 2008.

[63] Jr-Hau He, Jr-Jian Ke, Pei-Hsin Chang, Kun-Tong Tsai, P. C. Yang, and I-Min Chan. Development of ohmic nanocontacts via surface modification for nanowire-based electronic and optoelectronic devices: Zno nanowires as an example. *Nanoscale*, 4:3399–3404, 2012.

[64] C.S. Lao, J. Liu, P. Gao, L. Zhang, D. Davidovic, R. Tummala, and Z.L. Wang. Zno nanobelt/nanowire schottky diodes formed by dielectrophoresis alignment across au electrodes. *Nano Letters*, 6(2):263–266, 2006.

[65] P. Li, Q. Liao, Z. Zhang, Z. Wang, P. Lin, X. Zhang, Z. Kang, Y. Huang, Y. Gu, X. Yan, and Y. Zhang. Investigation on the mechanism of nanodamage and nanofailure for single ZnO nanowires under an electric field. *ACS Applied Materials and Interfaces*, 6(4):2344–2349, 2014.

[66] Alex M Lord, Thierry G Maffeis, Alex S Walton, Despoina M Kepaptsoglou, Quentin M Ramasse, Michael B Ward, Ju-Jin KimrgenJuole, and Steve P Wilks. Factors that determine and limit the resistivity of high-quality individual ZnO nanowires. *Nanotechnology*, 24(43):435706, 2013.

[67] Bogdan Bercu, Wei Geng, Olivier Simonetti, Sergei Kostcheev, Corinne Sartel, Vincent Sallet, Gilles Lrondel, Micha?l Molinari, Louis Giraudet, and Christophe Couteau. Characterizations of ohmic and schottky-behaving contacts of a single zno nanowire. *Nanotechnology*, 24(41):415202, 2013.

[68] Wei Geng, Sergei Kostcheev, Corinne Sartel, Vincent Sallet, Michael Molinari, Olivier Simonetti, Gilles Lrondel, Louis Giraudet, and Christophe Couteau. Ohmic contact on single ZnO nanowires grown by mocvd. *physica status solidi (c)*, 10(10):1292–1296, 2013.

[69] Shao-Pin Chiu, Yong-Han Lin, and Juhn-Jong Lin. Electrical conduction mechanisms in natively doped ZnO nanowires. *Nanotechnology*, 20(1):015203, 2009.

[70] C. Vieu, F. Carcenac, A. Ppin, Y. Chen, M. Mejias, A. Lebib, L. Manin-Ferlazzo, L. Couraud, and H. Launois. Electron beam lithography: resolution limits and applications. *Applied Surface Science*, 164(1?4):111 – 117, 2000. Surface Science in Micro & Nanotechnology.

[71] D.A. Scrymgeour and J.W.P. Hsu. Correlated piezoelectric and electrical properties in individual ZnO nanorods. *Nano Letters*, 8(8):2204–2209, 2008.

[72] Yong-Jun Ma, Ze Zhang, Feng Zhou, Li Lu, Aizi Jin, and Changzhi Gu. Hopping conduction in single ZnO nanowires. *Nanotechnology*, 16(6):746, 2005.

[73] J H He, P H Chang, C Y Chen, and K T Tsai. Electrical and optoelectronic characterization of a ZnO nanowire contacted by focused-ion-beam-deposited pt. *Nanotechnology*, 20(13):135701, 2009.

[74] Oleg Lupan, Lee Chow, Guangyu Chai, Leonid Chernyak, Olena Lopatiuk-Tirpak, and Helge Heinrich. Focused-ion-beam fabrication of ZnO nanorod-based uv photodetector using the in-situ lift-out technique. *physica status solidi (a)*, 205(11):2673–2678, 2008.

[75] Ivo Utke, Patrik Hoffmann, and John Melngailis. Gas-assisted focused electron beam and ion beam processing and fabrication. *Journal of Vacuum Science & Technology B*, 26(4):1197–1276, 2008.

[76] A. Fernandez-Pacheco, J.M.b c De Teresa, R Cocoletzi, G.rdoba, and M. Ibarra. Metal-insulator transition in Pt-C nanowires grown by focused-ion-beam- induced deposition. *Physical Review B - Condensed Matter and Materials Physics*, 79(17), 2009.

[77] W. F. van Dorp and C. W. Hagen. A critical literature review of focused electron beam induced deposition. *Journal of Applied Physics*, 104(8):–, 2008.

[78] D. Brunel, D. Troadec, D. Hourlier, D. Deresmes, M. Zdrojek, and T. Mlin. Characterization of ion/electron beam induced deposition of electrical contacts at the sub-μm scale. *Microelectronic Engineering*, 88(7):1569 – 1572, 2011.

[79] S.K. Tripathi, N. Shukla, N.S. Rajput, and V.N. Kulkarni. The out of beam sight effects in focused ion beam processing. *Nanotechnology*, 20(27), 2009.

[80] Dieter K Schroder. *Semiconductor material and device characterization*. John Wiley & Sons, 2006.

[81] R.M. Langford, T.-X. Wang, and D. Ozkaya. Reducing the resistivity of electron and ion beam assisted deposited Pt. *Microelectronic Engineering*, 84(5-8):784–788, 2007.

[82] SM Sze and K Ng Kwok. *Physics of semiconductor devices 3rd Edition*. Wiley Online Library, 2007.

[83] E.H. Rhoderick. Metal-semiconductor contacts. *IEE Proceedings I (Solid-State and Electron Devices)*, 129:1–14(13), February 1982.

[84] Z. Zhang, K. Yao, Y. Liu, C. Jin, X. Liang, Q. Chen, and L.-M. Peng. Quantitative analysis of current-voltage characteristics of semiconducting nanowires: Decoupling of contact effects. *Advanced Functional Materials*, 17(14):2478–2489, 2007.

[85] A Delan, M Rennau, S.E Schulz, and T Gessner. Thermal conductivity of ultra low-k dielectrics. *Microelectronic Engineering*, 70:280 – 284, 2003.

[86] Evgheni Strelcov, Serghei Dmitriev, Bradley Button, Joshua Cothren, Victor Sysoev, and Andrei Kolmakov. Evidence of the self-heating effect on surface reactivity and gas sensing of metal?oxide nanowire chemiresistors. *Nanotechnology*, 19(35):355502, 2008.

[87] J.Ross Macdonald. Impedance spectroscopy. *Annals of Biomedical Engineering*, 20(3):289–305, 1992.

[88] B.-Y. Chang and S.-M. Park. Electrochemical impedance spectroscopy. *Annual Review of Analytical Chemistry*, 3(1):207–229, 2010.

[89] S. Samanta, K. Das, and A.K. Raychaudhuri. Junction effect on transport properties of a single si nanowire metal-semiconductor-metal device. *IEEE Transactions on Nanotechnology*, 12(6):1089–1093, 2013.

[90] Francisco Hernandez-Ramirez, Albert Tarancon, Olga Casals, Jordi Rodriguez, Albert Romano-Rodriguez, Joan R Morante, Sven Barth, Sanjay Mathur, Tae Y Choi, Dimos Poulikakos, Victor Callegari, and Philipp M Nellen. Fabrication and electrical characterization of circuits based on individual tin oxide nanowires. *Nanotechnology*, 17(22):5577, 2006.

[91] Mark E Orazem. The impedance response of semiconductors: An electrochemical engineering perspective. *Chemical Engineering Education*, 24(1):48–55, 1990.

[92] Y.-P. Zhao, B. Wei, P. Ajayan, G. Ramanath, T.-M. Lu, G.-C. Wang, A. Rubio, and S. Roche. Frequency-dependent electrical transport in carbon nanotubes. *Phys. Rev. B*, 64:201402, Oct 2001.